UNIVERSIDADE D
COIMBRA

Rute Rodrigues dos Santos

Development of instrumentation for measuring Geomagnetically Induced Currents (GICs) and effect of shield wires on GIC simulations

Dissertation to obtain a Master's Degree in Physics Engineering, specialization in Instrumentation, supervised by Professor Maria Alexandra Albuquerque Faria Pais and by Professor João Manuel Rendeiro Cardoso and presented to the Physics Department of the Faculty of Sciences and Technology of the University of Coimbra.

October 2021

FACULDADE DE CIÊNCIAS E TECNOLOGIA
UNIVERSIDADE D COIMBRA

University of Coimbra
Faculty of Sciences and Technology

Master of Science in Physics Engineering

Development of instrumentation for measuring Geomagnetically Induced Currents (GICs) and effect of shield wires on GIC simulations

Rute Rodrigues dos Santos

Supervisor:
Professor Doctor M. Alexandra Pais
CITEUC

Supervisor:
Professor Doctor João Cardoso
LIBPhys-UC

Coimbra, October 2021

Abstract

Geomagnetically Induced Currents (GICs) are the result of rapid variations in the Earth's geomagnetic field and of the finite Earth's conductivity. Along grounded conducting structures such as transmission power networks, GICs can flow and, for extreme events, can be a threat to the power system normal operation. For this reason, interest in modeling GICs has been growing. This thesis work consists both in simulating the shield wire effects on GICs models and in assembling and installing a GIC measuring instrument at a power grid substation.

Shield wires can carry GICs similarly to power transmission lines. A simple equivalent circuit model that considered the effect of resistances and induced electromotive forces (emf) along the shield wires was derived. This model is an extension of an already studied model that consider only shield wire resistances. Tests were done using synthetic parameters and also realistic parameters from two Portuguese transmission lines. Results show that for some cases, it is important to consider shield wires and if the equivalent circuit is used, the induced emf must be taken into consideration. In addition, when increasing the complexity of the circuit model by connecting more power transmission lines to a substation, the equivalent circuit presented in this thesis has a higher accuracy than the equivalent circuit that neglects the induced emf.

GIC measurements should be taken in order to validate predicted values from GIC models. This thesis also encompasses the task of assembling and installing a measuring system to monitor GICs in the neutral of a given transformer. The system relies on a Hall effect current sensor and it was built over a Raspberry Pi 4 with a high resolution digitizer (24-bits). Preliminary tests in laboratory show a measurement precision of 0.056A. The system was installed at Paraimo Substation from REN and it is operational to collect data having already registered some candidate events for GICs in addition to the expected diurnal modulation due to temperature variations.

Keywords: Space Weather; Geomagnetically Induced Currents; Power Transmission Grid; Shield Wires; DC monitoring system;

Resumo

As Correntes Geomagneticamente Induzidas (GICs) são o resultado de variações rápidas no campo geomagnético terrestre e da condutividade finita da Terra. Ao longo de estruturas condutoras aterradas, como as redes de transporte de energia elétrica, as GICs podem fluir e, para tempestades geomagnéticas intensas, podem ser uma ameaça ao regular fornecimento de energia. Por esta razão, o interesse na modelação das GICs tem vindo a crescer. O trabalho desta dissertação consiste em simular o efeito dos cabos de guarda em modelos de GICs e na montagem e instalação de um instrumento de medição de GICs numa subestação da rede elétrica.

Os cabos de guarda podem transportar GICs tal como as linhas de transmissão de energia. Um circuito equivalente simples que considera o efeito das resistências e das forças eletromotrizes induzidas (fem) ao longo dos cabos de guarda foi concebido. Este modelo é uma extensão de um modelo já estudado que considerava apenas as resistências dos cabos de guarda. Foram realizados testes usando parâmetros teóricos e também parâmetros reais de duas linhas de transmissão da rede elétrica nacional. Os resultados mostram que, para alguns casos, é importante considerar os cabos de guarda e, se for utilizado o circuito equivalente, a fem induzida deve ser considerada. Além disso, ao aumentar a complexidade do modelo de circuito adicionando mais linhas de transmissão de energia a uma subestação, o circuito equivalente apresentado nesta dissertação tem uma precisão maior do que o circuito equivalente que despreza a fem induzida.

Para validar os valores previstos nos modelos, é importante fazer medições de GICs. Esta dissertação também abrange a tarefa de construir e instalar um sistema de medição para monitorização de GICs no neutro de um determinado transformador. O sistema consiste num sensor de corrente de efeito Hall e foi construído sobre uma Raspberry Pi 4 com um conversor analógico-digital de alta resolução (24 bits). Os testes preliminares em laboratório mostram uma precisão de medição de 0.056A. O sistema foi instalado na Subestação de Paraimo da REN e está operacional a recolher dados já tendo registado alguns eventos candidatos a GICs para além da expectável modulação diurna devida às variações de temperatura.

Palavras-Chave: Meteorologia Espacial; Correntes Geomagneticamente Induzidas; Rede de transmissão de energia; Cabos de guarda; Sistema de monitorização DC

Dedicated to my family

Acknowledgements

Esta dissertação representa o fim de uma etapa importante. Foram muitas as pessoas que, direta ou indiretamente, contribuíram para a sua concretização. Assim, deixo de seguida notas de agradecimento.

Aos meus orientadores, Professora Doutora Alexandra Pais e Professor Doutor João Cardoso, um muito obrigado pela partilha de conhecimento e pela imensa disponibilidade. Agradeço todo o apoio, paciência e sugestões de melhoria. Não consigo expressar o quão importante foram durante esta jornada ... obrigada por ambos contribuírem para o meu crescimento académico e pessoal.

Aos meus colegas do LIBPhys-UC, Pedro Vaz, pelos conselhos e sugestões no decorrer da montagem do sistema de medição de GICs, Andreia Gaudêncio, pelas conversas matinais e pela compreensão das minhas frustações :), por todos os conselhos e dicas e Miguel Silva, um obrigado especial por toda a paciência e disponibilidade em ajudar-me na parte da eletrónica e programação!

Aos membros do Projeto MAG-GIC pelo apoio e sugestões de melhorias. Em especial à Joana e ao Fernando por me incluirem tão bem no grupo e por toda a partilha de conhecimento.

À equipa da REN, nomeadamente Engenheiro Luís Perro e Engenheiro André Santos, pela disponibilidade, pelo apoio e pela colaboração em fornecer as informações necessárias da rede elétrica nacional. Agradecer também à equipa que nos recebeu em Paraimo, Engenheiro António Amaral, Engenheiro Adriano Carreira, Engenheiro Marco Figueiredo e Engenheiro Tiago Oliveira, pela disponibilidade e pela ajuda na instalação do sistema de medição de GICs.

Às minhas amigas de longa data, Diana Farinha, pelo ombro amigo sempre presente e Mariana Lopes, por todas as palavras encorajadoras e por toda a compreensão. Ao Pedro Nunes, pelo apoio e pelas conversas sobre o decurso desta dissertação. E aos mais recentes, Catarina Carvalho, Diana Mimoso e Fábio Morgado, por partilharem comigo os últimos anos de muitos desafios e algumas frustações.

Por fim, termino com as pessoas mais importantes e especiais da minha vida.

Aos meus pais, Maria e Joaquim, que sempre trabalharam e lutaram para poderem dar oportunidade às suas filhas de frequentar a Universidade. Obrigada por nos mostrarem que as conquistas e os sucessos são frutos do trabalho e dedicação! Obrigada por nos ensinarem que valores como honestidade, solidariedade, gratidão, respeito e responsabilidade devem ser seguidos. Obrigada por sempre nos acompanharem e aceitarem as nossas decisões! Mãe, Pai, estão de parabéns! Tendo apenas a

escolaridade mínima, conseguiram educar as vossas filhas (a um passo de poder dizer duas Engenheiras!) incentivando-as sempre a fazer mais e melhor.

À minha irmã, Cátia, por apoiar indubitavelmente as minhas escolhas, das mais acertadas às mais loucas, e por acreditar sempre em mim. Agradeço todos os conselhos, compreesão e sinceridade. Obrigada por seres o meu porto seguro.

O trabalho desenvolvido durante esta dissertação foi realizado com a atribuição de uma Bolsa de Investigação de Licenciatura (referência BIL 623468) durante 18 meses, associada ao projeto MAG-GIC (Correntes induzidas pelo campo geomagnético no território português, PTDC / CTA-GEO / 31744/2017), financiado pela FCT (Fundação para a Ciência e Tecnologia, I.P.). O projeto MAG-GIC é um projeto de investigação do CITEUC (Centro de Investigação da Terra e do Espaço da Universidade de Coimbra), o qual é financiado por Fundos Nacionais através da FCT (Projetos UID / 00611/2020 e UIDP / 00611/2020) e FEDER (Fundo Europeu de Desenvolvimento Regional através do Programa Operacional Competitividade e Internacionalização COMPETE 2020, projeto POCI-01- 0145-FEDER-006922).

Acronyms

!

1D	one-dimensional
2D	two-dimensional
3D	three-dimensional
AC	Alternate Current
ADC	Analog-to-Digital Converter
CIGRE	International Council on Large Electric Systems
CITEUC	Centro de Investigação da Terra e do Espaço da Universidade de Coimbra
CLA	IAGA code for Colaba Magnetic Station (India)
CME	Coronal Mass Ejections
COI	IAGA code for Coimbra Magnetic Station (Portugal)
CUA	IAGA code for Cuajimalpa Magnetic Station (Mexico)
DC	Direct Current
emf	Electromotive Force
EURISGIC	European Risk from Geomagnetically Induced Currents
GIC	Geomagnetically Induced Current
GMD	Geomagnetic Disturbance
GPIO	General-Purpose Input/Output from Raspberry Pi
IAGA	International Association of Geomagnetism and Aeronomy
IEEE	Institute of Electrical and Electronics Engineers
LFA.SN	Line between Ferreira do Alentejo e Sines
LIBPhys	Laboratory for Instrumentation, Biomedical Engineering and Radiation Physics
LPM.SB1	Line between Palmela and Setúbal
LSB	Least Significant Bit
NERC	North American Electric Reliability Corporation
OGAUC	Observatório Geofísico e Astronómico da Universidade de Coimbra
PGA	Programmable Gain

PLA	Polylactic acid polymer
REN	Redes Energéticas Nacionais, SGPS, S.A.
RNT	National Transmission Grid
SB	Setúbal Substation from REN
SFA	Ferreira do Alentejo Substation from REN
SFS	IAGA code for San Fernando Magnetic Station (Spain)
SNN	Sines Substation from REN
SPI	Paraimo Substation from REN
SPM	Palmela Substation from REN
SPT	IAGA code for San Pablo-Toledo Magnetic Station (Spain)
TSDB	Time Series Database
USD	United States Dollar
UT	Universal Time
ZKW	IAGA code for Zi-ka-wei Magnetic Station (China)

List of Figures

List of Tables

Contents

Chapter 1

Introduction

Contents

1.1 Motivation

Nowadays, society is strongly dependent on the supply of electricity. Even short interruptions may cause substantial losses for both supplier and customer, hence the operator of the transmission system has the responsibility to ensure security and reliability of the power transmission grid. There are some factors that may compromise the proper operation of the electrical transmission network, such as human activity and natural phenomena, in particular space weather events.

Space weather describes the variations in the space environment between the Sun and the Earth, which can have impact in systems and technologies in orbit and on Earth. During extreme space weather, the Earth's geomagnetic field varies rapidly and these episodes of perturbation are called Geomagnetic Storms or Geomagnetic Disturbances (GMD). As a result, there are induced electric fields in the Earth, which can drive currents in man-made grounded infrastructures such as transmission power systems. These currents are called Geomagnetically Induced Currents (GICs).

In transmission power systems, GICs can be measured when flowing through the transformer neutral which is connected to the ground. GICs have a very low frequency ($\sim$1mHz-1Hz) compared to power lines frequency currents (50Hz). The presence of these quasi-DC currents causes additional stress to the transformers, in the form of half-cycle saturation, which may lead to transformer heating, generation of harmonics and increased reactive power consumption. These effects tend to shorten the operational lifetime of transformers and in some cases to provoke their failure leading to power blackouts.

Due to this hazard to power systems, it is important to predict and prevent the flow of high GICs in the transmission network by creating good models. In order to

improve models, the most relevant parameters need to be identified and precise values need to be used. Finally, the models need to be validated against GIC measurements.

1.2 Goals

It is increasingly important to understand the parameters that influence the most the models used to calculate GICs and also to validate the same models with direct measurements of GICs. For this reason, the aim of this study is twofold:

- Study of the effect of the shield wires on the modeling of GICs in Portuguese power network.
- Design of an instrument to monitor GICs in the transformer neutrals in order to be installed in a Portuguese substation.

The two goals are outlined below:

The calculation of GICs in the power network depends on different parameters that must be considered, as the distribution of ground conductivity, laterally and in depth and the characteristics of the different components of the equivalent electric circuit. These include the values of the different resistances, the types of transformers and also the transmission path for the GICs, i.e., the network topology. Shield wires, which are protective cables of power transmission lines from atmospheric storms as lightning, represent possible paths for GIC currents. In the first part of this study the influence of shield wires on GICs in power systems is modeled. Then, tests are done using realistic values for the circuit parameters provided by the Portuguese high voltage power network company (REN - *Redes Energéticas Nacionais, SGPS, S.A.*).

There has been a recently published study that produced GIC simulations for the South of Portugal (Alves Ribeiro et al., 2021). Until the summer of 2021 there were no direct records of GICs in the electrical transmission network to validate this model. The present thesis work also encompasses the task of producing a measuring instrument to monitor GICs in the neutral of a given transformer. This instrument measures quasi-DC currents using a Hall current sensor, with high resolution. It is targeted to operate remotely over a time interval of several months while being minimally invasive to the power transformer. Laboratory testes are carried out before installing the instrument in a Portuguese substation.

1.3 The MAG-GIC Project

This thesis work has been done in the framework of the MAG-GIC project. The MAG-GIC Project (Geomagnetically induced currents in Portugal mainland, PTDC/CTAGEO/31744/2017) is the first initiative to evaluate the geomagnetic hazard to power systems in Portugal mainland. This proposal covers the whole chain of physical processes and related observational and analytical methods linking the geomagnetic field variability to final effects at high voltage power grids and modeling of GIC source currents.

The MAG-GIC Project is a very interdisciplinary project requiring a collaborative study of different domains: geophysics (geomagnetic driving fields, magnetotelluric measurements), engineering/physics (instrumentation, telemetry and remote sensing, power grid characteristics, estimation of GICs) and physics/maths (modeling, data analysis). Therefore, different research units are involved (see section 1.4).

A better knowledge of the Portuguese territory underground conductivity and a realistic assessment of the hazard to the power transmission network during geomagnetic storms are expected through this project. In the end, general recommendations for a more robust infrastructure will also be outlined.

1.4 Research Team

The subject of GICs is highly interdisciplinar, since it requires to deal with concepts from Space Physics, Geomagnetism, Applied Physics and Geophysics as well as with Instrumentation. Because of this, the present master thesis work was only possible to carry out in the framework of a collaboration between the two Research Centers introduced below.

CITEUC

The Center for Earth and Space Research of the University of Coimbra (CITEUC[1]) is a research unit dedicated to the study of Earth and Space Sciences. It has two research groups: Earth Dynamics and Solar System Sciences.

- The Earth Dynamics group studies the Earth's structure and the processes that occur inside it, crustal evolution and the History of Geosciences.
- The Solar System Sciences group studies the Sun-Earth interactions, focusing on solar physics, celestial mechanics, minor bodies of the solar system, and planetary geology.

CITEUC is housed at the Geophysical and Astronomical Observatory of University of Coimbra (OGAUC). This Observatory is responsible for the only magnetic observatory of Portugal, with IAGA code COI, using different magnetometers that have been monitoring the time-varying geomagnetic field since 1866.

CITEUC is funded by National Funds through FCT - Foundation for Science and Technology (Projects UID/00611/2020 and UIDP/00611/2020) and FEDER - European Regional Development Fund through COMPETE 2020 Operational Program Competitiveness and Internationalization (project: POCI-01-0145-FEDER-006922).

LIBPhys-UC

LIBPhys-UC is the UC pole of the Laboratory for Instrumentation, Biomedical Engineering and Radiation Physics (LIBPhys) formed by researchers from the Universities of NOVA of Lisbon, Coimbra, and Lisbon. LIBPhys is dedicated to research

[1] http://citeuc.pt/

in the areas of atomic, molecular, nuclear physics, electronic and industrial automation, instrumentation with applications to analytical methods, radiation detection, and biomedical engineering.

LIBPhys-UC [2] is funded by National Funds through FCT (project UID UIDB/ 04559/2021) and several COMPETE 2020 Operational European Regional Development Fund projects. Its activities are centered on the Physics Department of the University of Coimbra.

1.5 Structure of the thesis

The physical processes relating the Sun activity with GICs, as well as the main factors contributing to GICs and the methods to compute and measure them, are explained in Chapter 2.

The study of the effect of the shield wires on the modeling of GICs is presented in Chapter 3. A new equivalent circuit model is proposed and it is validated with real data from the Portuguese power network.

In Chapter 4 is proposed a GIC measuring instrument to measure quasi-DC currents that flow through the transformer neutrals in order to be installed in a Portuguese substation. Description of the process of choosing measuring equipment used in this dissertation will also be discussed. Furthermore, the system integration is described as well as laboratory tests.

The choice of the substation and of the transformer to install the sensor is explained in Chapter 5. Afterwards, the instrument installation procedure is described and first measurements are shown.

Chapter 6 summarizes the findings from Chapters 3, 4 and 5 and identifies interesting related problems to consider in future work.

[2] http://libphys.pt/

Chapter 2

Geomagnetically Induced Currents

Contents

2.1 State of the Art

2.1.1 GICs all over the world

GICs are more intense and can cause more damage on power systems located at high-latitude, in which geomagnetic storms are the largest and the most frequent (Astafyeva et al., 2015). In particular, higher-voltage networks can be seriously damaged due to longer line sections and lower line resistances (Zheng et al., 2013).

The first geomagnetic storm which had a remarkable effect on a modern power system was on March 24^{th}, 1940. There were several consequences reported regarding this storm, for example power system disturbances, numerous voltage dips and tripped transformers in the US and Canada and also telephone and telegraph systems failures in US and Norway (Boteler, 1998).

The iconic example of the overwhelming effect of GICs on electrical transmission networks occurred on March 13^{th}, 1989. It was the largest geomagnetic storm ever

measured. The worst effect of this storm was for Hydro-Québec network where the system collapsed in 92 seconds and around 9 million people were left without electricity. This blackout lasted around 9 hours for most places and the total amount of cost was estimated to have been 13.2 million USD (Mac Manus et al., 2017b; Rodger et al., 2020; Bolduc, 2002).

The Halloween Solar Storm, which happened on October 2003, was also an intense space weather event, largely studied. Satellites were affected by solar activity, flights at higher latitudes were rerouted all over the world, transformers were triggered leading to blackouts in southern Sweden (Pulkkinen et al., 2005) and thermal damage on transformers in Southern Africa (Gaunt and Coetzee, 2007) was documented. The loss of the Japanese ADEOS-2 spacecraft with a value of 640 million USD was assumed to be a consequence of this solar storm (National Weather Service, 2004).

The St. Patrick's Day storm in March 2015 was the strongest for the past 15 years. In New Zealand, magnetometers recorded significant variations on the geomagnetic field and there were measured GIC amplitudes of dozens of Amperes on a transformer (Rodger et al., 2020; Astafyeva et al., 2015). There is also a study of the ionospheric response to this geomagnetic storm in Astafyeva et al. (2015), where a hemispheric asymmetry was observed, phenomenon that normally occurs due to seasonal factors at solstices. Because this geomagnetic storm occurred at equinox, there's a strong conviction this hemispheric asymmetry could be due to geomagnetic storm.

Based on this GIC recorded events in the past and understanding that GIC can lead to network operational problems and blackouts, research on this field has been increasing and involving both geophysics and engineers for the past years. Besides all independent research all over the world, some dedicated research groups can be outlined:

- **NERC:** The *North American Electric Reliability Corporation* is a non-profit international regulatory authority for United States, Canada and a small part of Mexico whose mission is to assure the reduction of risks to the reliability and security of the grid. NERC was one of the first to consider GMD as a serious hazard to power industry.

- **EURISGIC:** In 2011, the *European Risk from Geomagnetically Induced Currents* project was founded by European Union with the main purpose of producing the first European real-time prototype forecast service of GIC in power systems, based on solar wind observations and comprehensive simulations of the Earth's magnetosphere. They provide this information to public through the website `eurisgic.org`.

- **IEEE Guide:** The IEEE created a guide (IEEE C57.163-2015) to specify the capability of power transformer under geomagnetic disturbances.

- **CIGRE Working Group:** The *International Council on Large Electric Systems* is a non-profit association which main goal is to collaborate with experts all over the world to discuss future developments and transfer knowledge on power system industry, recently creating a group to study the effect of geomagnetic storms in power grids.

2.1.2 GIC studies in Portugal

Despite Portugal being a mid-latitude country, the Portuguese power network can suffer from the hazardous effect of GICs. It has been studied and observed effects, more or less severe, of GICs in other mid-latitude countries such as Spain, China, Japan and South Africa (Torta et al., 2014, 2017; Choi et al., 2015; Liu et al., 2009; Bernhardi et al., 2008b; Nakamura et al., 2018).

Regarding the study and measurement of GICs in power systems, Portugal is starting to take its first steps compared to other countries such as New Zealand, China and Canada (Rodger et al., 2020; Mac Manus et al., 2017a; Boteler, 1998). Until the summer of 2021 there were no direct record of GICs in the electrical transmission network. The existing records concern the driving geomagnetic storm signal B(t), at the geomagnetic observatory of Coimbra (COI) using different magnetometers that have been monitoring the time-varying geomagnetic field since 1866. All this data is save in the SPINLab laboratory providing the most recent data that allow interested people to monitor the conditions of Space Weather. Although this observatory is the only one in Portuguese territory, San Pablo-Toledo (SPT) magnetic observatory, in Spain, is relatively close to COI ($\sim$ 400 km) (Alves Ribeiro et al., 2021).

Figures 2.1 and 2.2 represent the geomagnetic field horizontal components B_x and B_y during two storm events: the historical storm on the October 31^{st} - November 2^{nd}, 1903 and the St Patrick storm on the March 17^{th}, 2015. B_x represents the geomagnetic field component with the direction North-South (positive towards North) and B_y represents the geomagnetic field component with the direction East-West (positive towards East). The values are shown for every minute. In the case of the 1903 storm, this sampling was obtained from digitizing the magnetogram registration, on photographic paper.

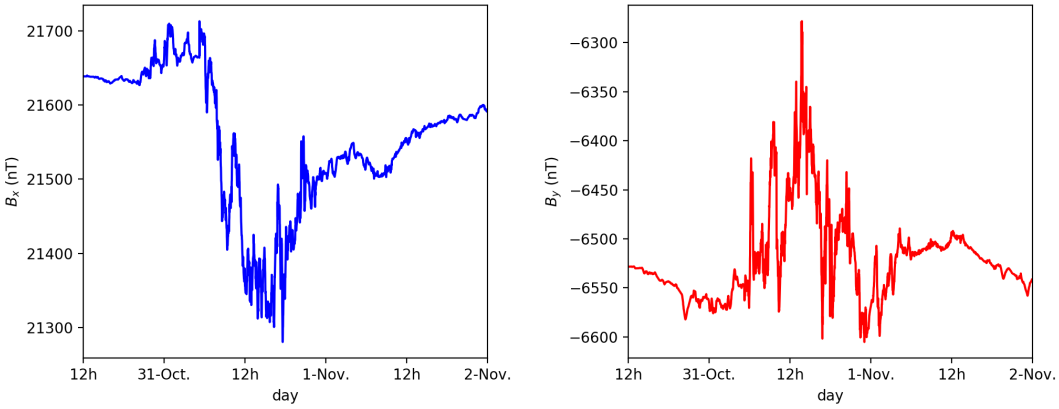

Figure 2.1: Magnetic field components B_x and B_y at COI during geomagnetic storm in October 1903. From the OGAUC server: https://spinlab.ogauc.pt.

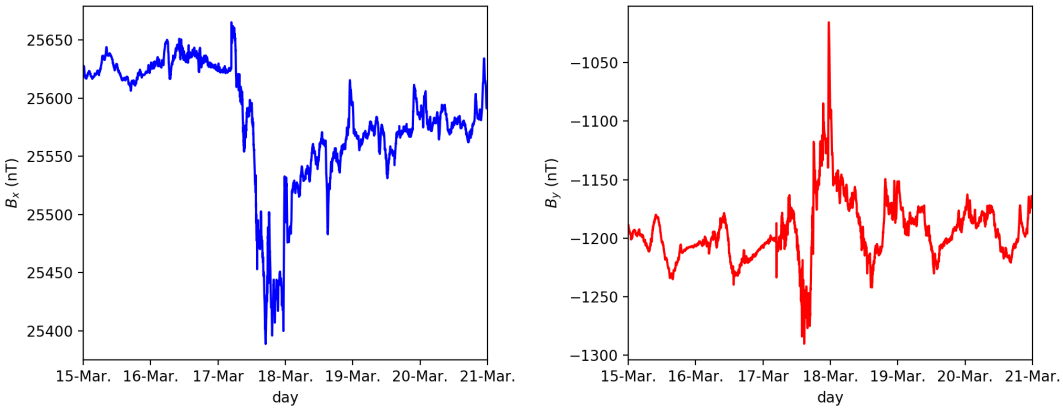

Figure 2.2: Magnetic field components recorded at COI during St. Patrick's Day storm (March 2015). From the OGAUC server: https://spinlab.ogauc.pt.

The first space weather event that was documented in Portuguese newspapers, was from the geomagnetic storm of October 1903. This geomagnetic storm affected significantly a number of communication networks in both mid-latitude Iberian countries. A review of this event is documented in Ribeiro et al. (2016). The telegraph communication network was practically interrupted from 09h30 UT to 21h00 UT and the cause of this failure was the flow of GICs in the telegraphic lines. A point of interest in this study is the possibility of confirming the origin of these communication failures through measurements of the geomagnetic field variations that are available at COI and San Fernando (SFS). Later, measurements of the observatories of Colaba (CLA), Cuajimalpa (CUA) and Zi-ka-wei (ZKW) were also analyzed in order to provide further information on this space weather event (Hayakawa et al., 2020) (Figure 2.3) .

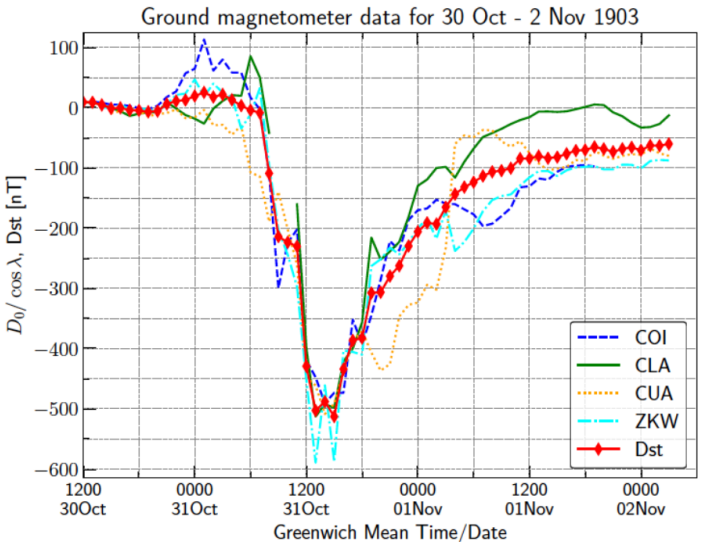

Figure 2.3: The plot shows the magnetic disturbance (curve D_0, very close to the field B_x curve) at stations of COI, CLA, CUA, and ZKW during the 1903 Oct. 30 - Nov. 2 event. From Hayakawa et al. (2020)

Also related to this geomagnetic storm, the newspaper article "Record of the great magnetic storm of October 31^{th}, 1903, at Ponta Delgada, Azores" (Chaves, 1904) was published. The occurrence of Aurorae Borealis at the time of that event was also recorded, at lower latitudes than usual (see Figure 2.4).

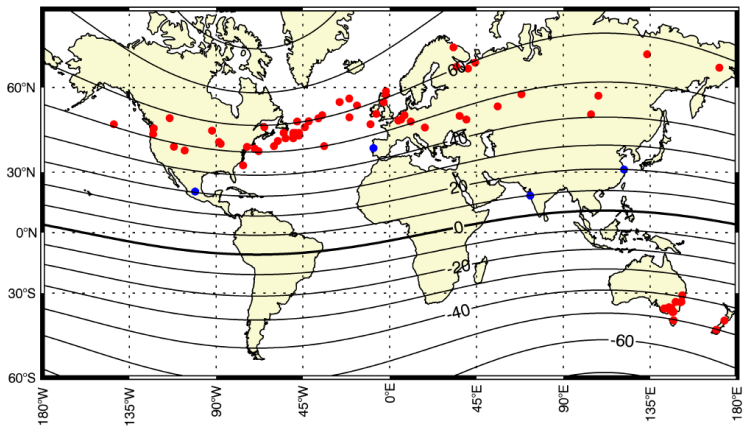

Figure 2.4: Auroral visibility between October 30^{th} and November 1^{st}, 1903. In blue is represented COI, CLA, CUA and ZKW stations. From Hayakawa et al. (2020).

Concerning GIC modeling, the first results for the estimation of GICs over the southern area of the Portuguese power transmission network have been published recently (Alves Ribeiro et al., 2021). This study used a conductivity model for the earth underneath the Portuguese south region, taking into account the proximity to the ocean (higher conductivity values). From there, and using geomagnetic data from the COI observatory, the induced geoelectric field was computed for the most intense storms during the year 2015 of solar cycle 24. The study above mentioned has been done with the collaboration of REN, that provided the grid parameters as transmission lines, transformer winding resistances and grounding resistances, as well as information on the type and number of transformers in each substation. This information is crucial to obtain more accurate GIC estimations.

2.2 Geomagnetic Storms and Induced Electric Field

Certain events of solar activity can represent a significant risk for modern society so heavily dependent on power supply. With the exponential increase in the use of power consuming technologies, it is increasingly important to realize the potential hazard in the impact of solar storms.

2.2.1 Origin of geomagnetic storms

The Sun constantly emits particles and electromagnetic radiation in all directions, in the form of solar flares, coronal mass ejections (CMEs) and solar wind (Pulkkinen et al., 2017; Blake, 2017). Solar flares are sudden and intense explosions on the Sun's surface caused by changes in its magnetic field. These explosions release high levels of energy, in the form of electromagnetic radiation and particles at high speeds. Solar flares are often accompanied by CMEs. A CME is a giant cloud of plasma, many times the size of the Earth, that carries billions of tons of coronal material from the Sun to very large distances. The direction of the CMEs is not uniform. Depending on the blast direction, it can miss the Earth or arrive to Earth in less then 20 hours (Vourlidas et al., 2017). The solar wind is the continuously streaming of plasma ejected by the Sun in all directions. This gas consists of electrons and protons that leave the Sun gravitational attraction thanks to high temperature of the atmosphere of the solar corona base.

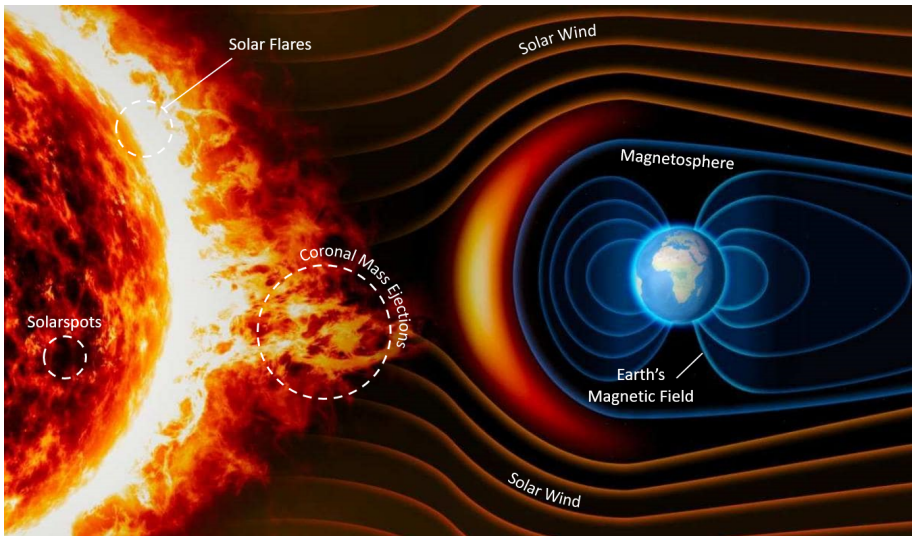

Figure 2.5: Representation of solar activity and Earth environment (adapted from NOAA (2019)).

CMEs are the most important drivers of space weather phenomena. When these particles and the magnetic field they carry along reach the Earth environment, they interact with the magnetosphere (Rothwell and McIlwain, 1960). The Earth's magnetosphere is defined as the region where the dominant magnetic field is the magnetic field of Earth, rather than the magnetic field of interplanetary space. The size of the magnetosphere is continuously changing as the Earth's magnetic field is hitted by the solar wind (Milan et al., 2017). To clarify, the Earth's magnetic field is also called

geomagnetic field and it is the magnetic field that extends from the Earth's interior out until the boundary of the magnetosphere. This magnetic field is generated by electric currents due to motion of convection currents in the Earth's liquid outer core.

A Geomagnetic Storm usually occurs when a strong solar wind reaches the magnetosphere. There is periodicity in the solar activity called solar cycle, which is typically about 11 years long (Hathaway, 2015). Although large storms can occur over time (Hayakawa et al., 2020), greater solar activity is expected during the maximum of solar cycle. The last maximum of solar cycle was in 2015 during cycle 24. Figure 2.6 shows a visual effect of a geomagnetic storm: Aurorae Borealis.

Figure 2.6: Impact of a cloud of plasma on the Earth's magnetosphere - Aurorae Borealis (from NASA (2016)).

2.2.2 Storm-induced electric fields

Geomagnetic storms (or geomagnetic disturbances) can represent a hazard to the normal daily lives of the Earth's population because of induced currents in grounded technological infrastructures.

According to the Faraday's law, when there is a rapid change in the magnetic field, there is also an associated electric field induced in a conducting medium permeated by magnetic field lines. This is the case for the Earth. The electric field ($\mathbf{E}$) induced in the Earth is particularly strong on the surface. It allows electric currents to flow on ground man-made facilities, such as power systems (Boteler and Pirjola, 2017), gas pipelines (Pulkkinen et al., 2001) and railway systems (Boteler, 2020).

The mechanism of conversion of magnetic field energy into sources of electromotive force can be explained according to Romer (1982). In his paper, he studies and discusses Faraday's law in a multiply connected region. A topological space is called simply connected if every closed path in that space can be continuously shrunk to a point while preserving all its points inside that region. If that doesn't happen, the region is multiply connected (Figure 2.7).

Figure 2.7: Illustration of a simply connected region (left side) and multiply connected regions (right side).

Figure 2.8 represents the circuit studied by the author. He considered a very long solenoid perpendicular to the plane in the Figure, carrying a varying current. The solenoid is surrounded by a circuit with two resistors (resistance values R_1 and R_2) and two identical voltmeters (readings V_1 and V_2).

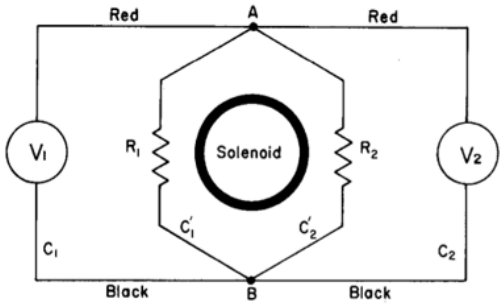

Figure 2.8: Circuit presented in Romer (1982) to study Faraday's law in a multiply connected region.

Briefly describing the circuit, there is a magnetic field produced inside of the solenoid because of the varying current on it. Outside the solenoid and near the coil, the magnetic field can be considered zero because of the long length of the solenoid. After introducing this circuit, the author questions the values of V_1 and V_2 and sustains that V_1 is always different from V_2 although they are connected to the same points. Measurements carried out by the author confirm this.

The reason the values are different is because there is an induced electromotive force (emf) in the path through the resistors generated by the time-varying magnetic field. This phenomenon can be easily explained by Faraday's law (equation 2.1) and Stokes' Theorem (equation 2.2).

$$\boldsymbol{\nabla} \times \mathbf{E} = -\frac{\partial \vec{B}}{\partial t} \tag{2.1}$$

$$\iint_S (\boldsymbol{\nabla} \times \mathbf{E}) \cdot dS = \oint_C \mathbf{E} \cdot d\mathbf{r} \tag{2.2}$$

By Faraday's law, in points where there is a varying magnetic field, $\boldsymbol{\nabla} \times \mathbf{E}$ is not zero. This means that $\boldsymbol{\nabla} \times \mathbf{E}$ is everywhere null except within the interior of the solenoid.

Stokes' theorem says that the line integral of a vector field over a closed path is equal to the flux of its curl through the enclosed surface bounded by the same path.

In this case, if we take the path through the resistors there will be a non-zero line integral of the electric field (an electromotive force, emf) because $\nabla \times \mathbf{E}$ isn't null in the region enclosed by that path (in spite of $\nabla \times \mathbf{E} = 0$ at all points along the path). In fact, only in a simply connected region can we associate $\nabla \times \mathbf{E} = 0$ to a conservative field. Although the resistors are in a region where $\nabla \times \mathbf{E}$ is null, this region is not simply connected.

In the case of the Earth, it is always permeated by geomagnetic field lines, that change at the time of geomagnetic storms. Faraday's law given by equation 2.1 then explains an induced electric field. Since the Earth is an electrical conductor with a certain conductivity, currents are induced that, by themselves, also contribute to the changing magnetic field. In the end, geomagnetic field variations during geomagnetic storms induce an electric field on the Earth's surface, to which the conductivity of the Earth is also important. From the time-varying magnetic field and a model of electrical conductivity for the Earth, the induced electric field on the surface can be computed (Boteler and Pirjola, 2017; Blake, 2017). If there are conductors connected to the ground, currents can flow on ground man-made technologies as shown in the Figure 2.9. The induced electromotive force between points A and B is obtained through

$$emf = \int_A^B \mathbf{E} \cdot d\mathbf{r} \tag{2.3}$$

where $\mathbf{E}$ is the induced electric field. Note that the integral gives in practice the same result if the chosen path is along the Earth's surface or along the phase line at altitude H (Boteler and Pirjola, 2017).

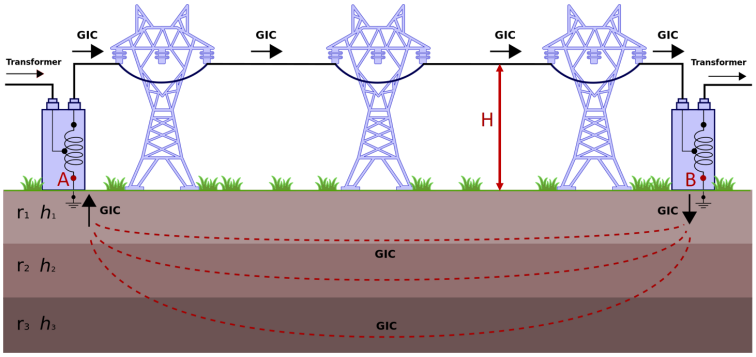

Figure 2.9: Representation of the electrical transmission system showing the path where the GICs flow. Adapted from Cardoso et al. (2019).

2.3 GIC main effects on the Electric Power Line Infrastructure

Electric power transmission grid, oil and gas pipelines, phone cables and railway systems are some examples where GICs are driven because they are infrastructures with long conductors and grounding connections (Pirjola, 2000). In the case of the electric power system, GICs flow to and from the ground through the winding neutral of power transformers because they are connected to the ground (Figure 2.9).

When flowing in the electrical transmission network, GICs can be considered quasi-DC current ($\sim$ 1mHz - 1Hz) compared to the 50Hz current in the transmission lines (Boteler and Pirjola, 2017). As a result, several power system devices such as generators, protective relays, capacitor banks, overhead line conductors, blocking devices and transformers are forced to operate under conditions outside their original specifications (Abda et al., 2020; Halbedl, 2019):

- **Generators:** Normally, generators are not directly affected by GIC due to the isolated connection between the generator and the power system. However, generators are exposed to harmonics in the electric current, resulting both in increased mechanical vibrations and in increased generator heating due to oscillating rotor flux. Retaining rings and wedges are examples of rotor components susceptible to damage due to rotor heating.

- **Capacitor banks:** Capacitor banks, which are a combination of numerous capacitors of similar rating to collect electrical energy, are generally used for Reactive Power Compensation. Reactive power is the portion of electricity that helps establish and sustain the electric and magnetic fields required by AC equipment, such as transformers and generators. Management of this reactive power to improve the performance of those AC systems is called Reactive Power Compensation. GICs can affect capacitors banks with harmonic over-currents generated during half-cycle saturation and resonance is also possible to occur too.

- **Overhead line conductors:** A DC exposure on overhead line conductors can lead to temperature rise and in turn, increase line sag, i. e. the vertical difference in level between points of support (pylons) and the lowest point of the conductor. (Halbedl, 2019).

- **Transformers:** A DC component of current circulating in power transformers produces half-cycle saturation (Bolduc and Aubin, 1978) leading to thermal losses, undesired tripping and mechanical vibration.

The most affected component is the transformer, so it will be better discussed below.

2.3.1 Transformers

In order to understand the impact of GICs in the transformers, their main functionality will be presented, as well as the most familiar types of transformers and the consequences of DC current saturation on them.

2.3.1.1 Principle of Transformers

The transformer consists of a magnetic circuit with an iron core and a winding (in an autotransformer), or two or more coupled windings for inducing mutual coupling between circuits. The iron core is composed of a ferromagnetic material with high magnetic permeability; it is permeable to a time-varying magnetic flux (Φ) and concentrates magnetic field lines, therefore promoting the magnetic coupling between the two windings.

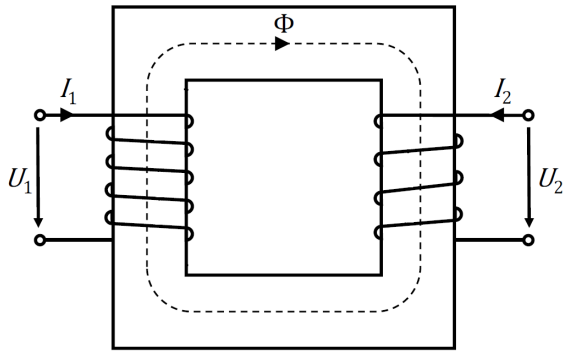

Figure 2.10: Basic construction of a single-phase two-winding transformer (adapted from Halbedl (2019)), i.e., galvanically isolated.

Figure 2.10 shows a simple representation of a two-winding transformer. The current I_1, created by the time-varying voltage source U_1, generates a magnetic flux through the first winding with N_1 turns, and produces a varying magnetic flux in the transformer's core (changing Φ). This magnetic flux is driven by the magnetizing current (I_m) into the core. Finally, the alternating flux induces a voltage U_2 in the second winding with N_2 turns, also around the same core.

The two voltages are related through $\frac{U_1}{U_2} = \frac{N_1}{N_2}$, showing how the transformer can vary the voltage level between two lines. This process may occur without a metallic (conductive) connection between the two circuits.

2.3.1.2 Types of Transformers

A single-phase two-winding transformer is nothing more than what Figure 2.10 shows: a primary and a secondary winding around the same magnetic core. Modern electrical systems are almost exclusively three-phase systems having, in most cases, three-phase two-winding transformers to convert voltages.

In three-phase two-winding transformers, the primary and the secondary have three phases. The most common ways to connect them are the Y and the Δ configurations. In the Y configuration, the three phase wires are connected like a star and there is a further neutral wire. In the Δ configuration, the three phase wires are connected one after the other, as in a triangle, and there is no neutral wire. The two most common ways to connect the primary and secondary are the Y-Y and the Δ-Y configurations (Figure 2.11 a) and b)).

There is other type of transformer that must be introduced: the autotransformer (Figure 2.11 c)). Unlike the previous examples of two sets of phase wires electrically isolated one from the other, an autotransformer has only one single winding set. This

winding set has two end terminals and one or more terminals at intermediate points having a portion shared by both the primary and secondary circuits.

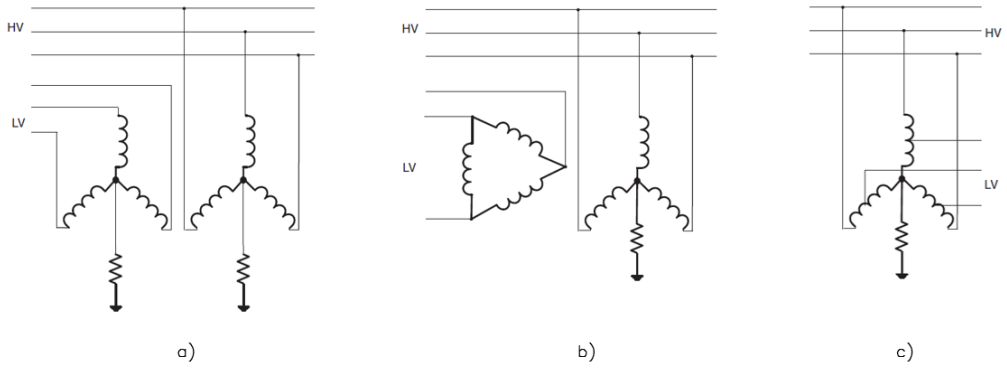

Figure 2.11: Representation of different types of transformers: a) Y-Y transformer; b) Δ-Y transformer; c) autotransformer. Adapted from Torta et al. (2014).

For GICs studies, transformers with connection to the ground, such as Y-connected winding, are the most interesting types of transformers because currents can flow to the transmission system by them (Boteler Pirjola and Pirjola, 2014; Koen and Gaunt, 2003).

2.3.2 DC current saturation

In practice, the direct consequence of GICs is the production of half-cycle saturation of transformer cores (Rodger et al., 2020; Zawawi et al., 2020). This can be explained by Figure 2.12 which shows how to get the magnetizing current I_m (ordinate axis) from the magnetic flux Φ (abscissa axis), in the transformer core, through the magnetization curve characteristic.

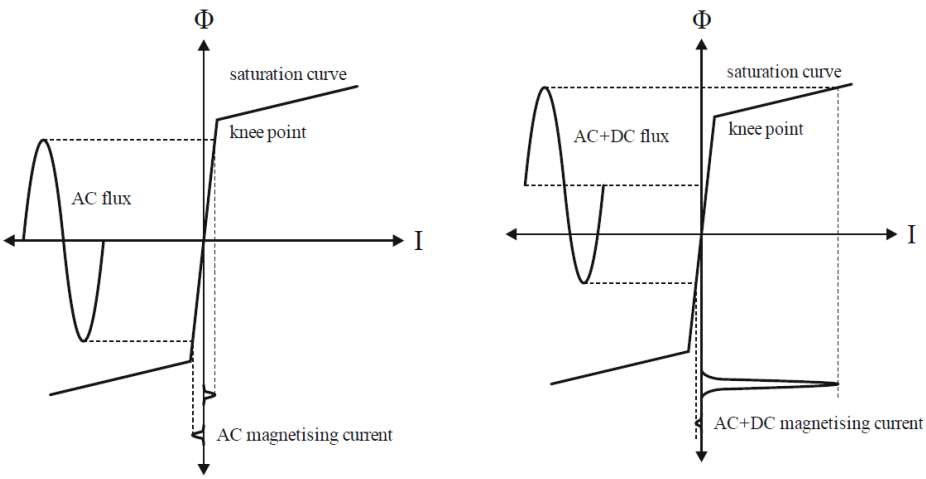

Figure 2.12: Simplified scheme of transformer magnetization: normal operation on the left and positive half-cycle saturation on the right. From Halbedl (2019).

On the left of this figure, the normal working principle of the transformer is represented. The AC magnetic flux operates in the linear range of the magnetization curve, where the maximum peak values are close to the knee point. If the transformer iron core did not saturate, the magnetizing current, generated by the flux, would be sinusoidal in shape and in phase with the flux. But because of transformers are operating near the knee point, some degrees of saturation already exists. As a consequence, the magnetizing current is symmetrical, but cannot be sinusoidal due to magnetization curve non-linearity, having presence of odd harmonics (Mari, 2020).

Resolving the magnetizing current wave into a series of component sine curves, it is equivalent to a sine wave of a fundamental frequency and a series of odd harmonics, with the third harmonic being the most dominant. Figure 2.13 shows the magnetizing current constituted by fundamental and third harmonic.

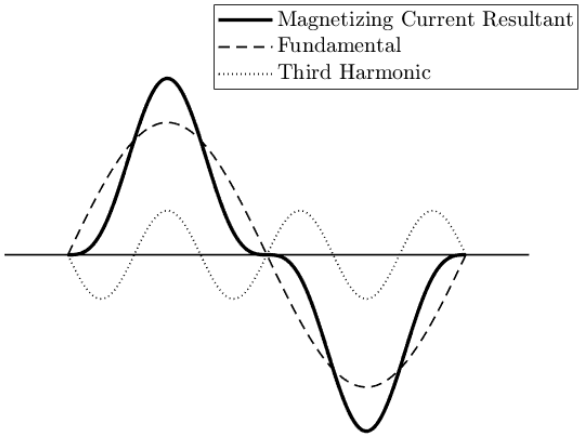

Figure 2.13: Magnetizing current wave composed by a fundamental and third harmonic. From Mari (2020).

Although this type of saturation leading to odd harmonics is not desirable, it is a standard consideration for electrical engineers. In fact, power engineers typically design systems to avoid the production and impact of odd-order harmonics.

The right side of Figure 2.12 shows the saturated condition of transformer operation where an additional DC component on the transformer windings causes an offset to the AC flux density in the magnetic core. As Figure 2.12 shows, the transformer core saturates in only one direction, such that the magnetizing current spike appears only once per cycle for only one polarity. This type of saturation is termed asymmetric saturation or "half-cycle" saturation resulting in not only odd but also even harmonics (Rodger et al., 2020).

Some consequences of half-saturation of the transformer are now listed and briefly explained as well as some examples of damaged transformers are shown in Figures 2.14 and 2.15.

Thermal Losses and overheating

The flux that does not follow through the iron core of the transformer is called the leakage flux. As it is expected, the larger the magnetizing current, the greater the leakage flux outside the core. As a consequence, there is a increase of eddy current losses in the windings and structural parts (Girgis et al., 2012; Molinski, 2002). Locally, hot spots can occur in those parts and lead to transformer failure.

Reactive Power Consumption

As mentioned before, the reactive power is the portion of electricity that helps establish and sustain the electric and magnetic fields required by AC equipment, such as transformers. When a transformer faces half-cycle saturation, the reactive power consumption increases. This causes a decrease in system voltage and therefore problems in voltage stability (Albertson et al., 1979).

Undesired tripping

As a result of generated harmonics, the protective relays can trip due to false operation. As a consequence, there can be a loss of power generation and simultaneously the line frequency will rise and the load flow will change in the network. In worst scenario, it can lead to power blackouts.

Mechanical Vibration - Noise

Another consequence of harmonics is the increase in mechanical vibrations and noise. The sound power of the transformer rises sharply.

Figure 2.14: Damaged transformer owned by the Public Service Electric and Gas Company of New Jersey damaged by the March 13-14th, 1989 geomagnetic storm. From Marusek (2007).

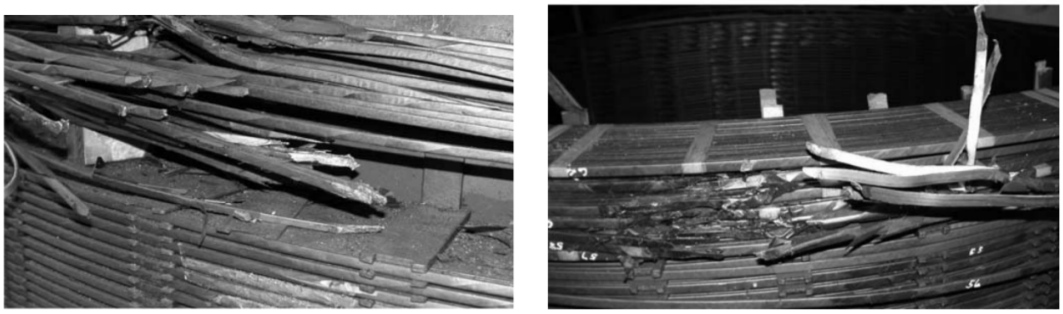

Figure 2.15: Windings of Eskom transformers, Southern Africa, presumed damaged by the geomagnetic storm on the October 29^{th}, 2003. From Bernhardi et al. (2008a).

As explained above, all those harmful effects make it important to study the effect of geomagnetic storms in the power systems and understand the hazard that it represents for the normal operation of the electrical network, so essential to human daily life.

2.4 GIC mitigation on Power Transmission Network

Since GICs can represent a hazard to energy transmission network, the study of this space weather phenomenon on power systems is required. Therefore, there are different fields and steps to be considered.

The first step is related with GIC sources forecasting, which consists in solar activity studies and predictions. The main goal is modeling the magnetic field of interplanetary space in association with CMEs to compute its fluctuations (Schatten et al., 1969).

The second step is to study the interaction of CME plasma with the Earth's magnetosphere, in particular how this originates GMDs. The third step consists in predicting the flow of high GICs in the transmission network, starting with the calculation of induced electric field up to GIC modeling on the energy transport network. The validation of these models is made with GIC measurements (fourth step).

Finally, the fifth step is related with hazard prevention. It is necessary to understand how to reduce the risk to the electrical network when it is prone to high GICs. In UK, Oughton et al. (2019) started to study the risk for the socioeconomic impact of electricity infrastructure failure due to space weather and showed that the costs associated with power systems failure can reach very high values (billions USD).

The study of this thesis focuses on the third and fourth points, so they will be better discussed in the next sections.

2.4.1 Modeling of GICs

In order to have a model that allows a calculation of GICs as close to reality as possible, it is necessary to consider several parameters implicated in their generating mechanism. These parameters belong to two separate fields: Geophysics and Engineering (see Figure 2.16).

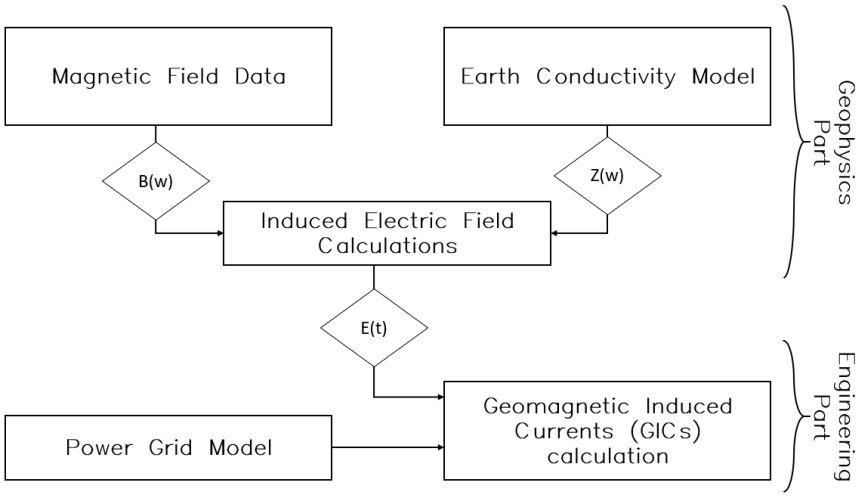

Figure 2.16: Flowchart of the GIC calculation, including Geophysics and Engineering contributions.

Regarding the contribution from Geophysics, the first step is to measure the geomagnetic field near the Earth's surface, either with permanent magnetic observatories to monitor and measure the local geomagnetic field (Thomson, 2014) or satellite missions to monitor the global field distribution. The second step is to calculate the induced electric field, for which an Earth's conductivity model is needed. These models are very dependent on the type of geological materials that compose the Earth. For example, in regions where geomaterials are overall more resistive, the induced electric field at the Earth's surface tends to be stronger. The model used to calculate the electric field can be one-dimensional (1D), two-dimensional (2D) or three-dimensional (3D). 1D layered model is the simplest and most commonly used model. However 2D and 3D models can provide more accurate results because they consider lateral variations, as e.g. proximity to the coast, and not only the variation with depth (Simpson and Bahr, 2005; Blake, 2017). The induced electric field $\mathbf{E}$(t) is computed from the GMD field $\mathbf{B}$(t) and the Earth's conductivity model, through equation 2.4 (see Alves Ribeiro et al. (2021); Torta et al. (2014)) where the calculation is first made in the Fourier space (frequency ω) and then the inverse Fourier transform is applied.

$$\mathbf{E}(\omega) = \frac{1}{\mu_0}\mathbf{Z}(\omega)\mathbf{B}(\omega) \tag{2.4}$$

In this equation, $\mathbf{Z}$ is the impedance tensor which relates the electric and magnetic fields at a certain location on the Earth's surface. It has information about the resistivity of the ground as well as the dimensionality and direction of those fields. μ_0 is the magnetic permeability of free space.

Knowing the induced electric field on the Earth's surface, the third step is to know the necessary power network parameters to be able to calculate the value of GICs in the power transmission elements. In order to have a good representing model of the power network, it is necessary to know:

- **Location of each substation**, that is, the coordinates of the sites where transformers are located and grounding nodes exist.
- **Transformers specifications**, for example, type of transformers, number of units of each type, winding resistances and connection of each transformer to different voltage levels.
- **Characteristics of the possible paths for GICs** (transmission line and shield wires) such as the voltage level for the transmission line, the line impedance and line length for both transmission line and shield wires (see chapter 3).
- Grounding resistance at each substation

Once the induced field was calculated in each point and the location of power lines is given, the induced emf along each line can be computed. These emf are equivalent to a DC voltage sources connected in series along the transmission lines located between substations and along the shield wires between pylons.

Finally, GICs (**I**) are obtained by solving the matrix equation 2.5 (see Boteler, David (2014); Lehtinen and Pirjola (1985)):

$$\mathbf{I} = (\mathbf{1} + \mathbf{YZ})^{-1}\mathbf{J} \tag{2.5}$$

where **1** is the unit matrix, **Y** is the network admittance matrix, **Z** is the grounding impedance matrix including the substations' grounding resistances of the system and **J** incorporates the induced voltages between substations.

2.4.2 Measurement of GICs

Measurement of GICs can be done using direct or indirect methods.

- **Direct method:** measurement of electric currents directly on the line connecting the transformer neutral to the ground;
- **Indirect method:** measurement of the differences in the magnetic field closer and farther away from the power lines.

Figure 2.17: Hall effect sensors.

Figure 2.18: Harmonic distortion sensor.

Direct measurements can be done with a Hall effect sensor (examples on Figure 2.17). A Hall effect sensor is a type of sensor which measures near DC magnetic field

having an output voltage proportional to the strength of the field (more information in chapter 4). There are studies in different countries that use a Hall effect sensor to measure GICs as is the case in Brazil (Barbosa, Cleiton et al., 2015), Austria (Bailey et al., 2018), Ireland (Blake et al., 2016) and New Zealand (Rodger et al., 2020), others use Hall effect probe or clamp like UK (Hübert et al., 2020), Korea (Choi et al., 2015) and Japan (Nakamura et al., 2018).

GICs can also be measured using the differential magnetometer method (DMM) (Hübert et al., 2020). This method consists in measuring the magnetic field in two different points (see Figure 2.19). The first measurement point (P1) is located directly under the power line and detects magnetic field caused by both the GIC and the natural fluctuations in the geomagnetic field. The second measurement point (P2) is placed away from any electric power transmission line and is used as reference which records mainly the natural fluctuation in the geomagnetic field. The difference between the two measurements and a model for the variation of GIC signal with distance, give an estimate of the magnetic field only due to the GIC.

New Zealand is the country that does the most monitoring of GICs. Besides having Hall effect sensors (LEM LT500 or LT505 types, see chapter 4) installed in 60 transformers in 22 substations (data from November 2018), they also have 3 magnetometers and a Schneider PowerLogic ION8800 meter (Figure 2.18) installed in each substation to measure the harmonic distribution caused by transformer core saturation (see section 2.3.2) (Rodger et al., 2020).

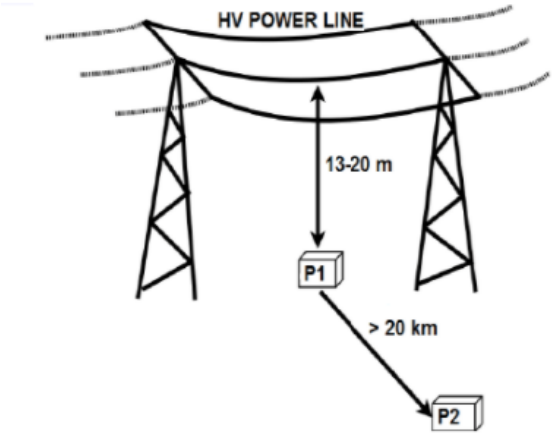

Figure 2.19: Magnetometer setup for differential magnetometer method. From Matandirotya et al. (2015).

Muchinapaya et al. (2018) recently published a paper in which the design of a low-cost system to monitor GICs in transformers neutrals is presented . He suggested a simple system with a Hall effect sensor, a band pass filter, a temperature sensor and a microcontroller. The temperature sensor is used because Hall effect sensors are sensitive to temperature variations (Cholakova et al., 2012) and it is important to calibrate the system. Analogue signals from Hall effect sensors need to be filtered to remove unwanted signals with lower or higher frequency. So a bandpass filter is used. Then, there's a microcontroller that handles data from the sensors to end users. Some specifications are also important for the system performance as flash memory,

power consumption, operation temperature and clock speed. Lastly, the data storage is made by a memory card. In Chapter 4, the measuring device that was developed during this thesis will be presented.

2.5 National Power Transmission Network

Nowadays, electricity is generated through different energy sources such as natural gas, potential energy of water, kinetic energy of winds, fuel oil, sun and biomass. The number of generators in Portugal mainland have been increasing for the past years with the increasing interest in renewable sources.

The National Transmission Grid (RNT) is the system which connects the generators to consumption centers and ensures a balance between energy supply and demand. The electricity transmission entity in Portugal that operates RNT is REN - *Redes Energéticas Nacionais, SGPS, S.A.*, under a concession agreement with the Portuguese state. The RNT delivery points feed the distribution network that supplies most final consumers.

According to 2020 data, REN has 9,036 km of lines and 68 substations all over the country (see appendix B.1). The extra high voltage grid is composed by 400 kV, 220 kV and 150 kV grid lines:

- **400 kV** grid lines mainly run north to south near the coast from Alto Lindoso power station in the north to Algarve, and west to east, where they interconnect with the Spanish grid.
- **220 kV** lines run between Lisbon and Oporto, diagonally between Miranda do Douro and Coimbra, along the River Douro and in Beira Interior.
- **150 kV** lines were the first lines in the RNT (since 1951).

Figures 2.20 and 2.21 are photographs of the Paraimo substation, which has 400, 220 and 60 kV lines. Figure 2.22 is a photograph of a transformer in that substation. The first instrument for measuring GICs will be installed in this substation (see chapter 5).

Figure 2.20: Area of Paraimo substation referring to 60 kV lines.

Figure 2.21: Area of Paraimo substation referring to 400 kV lines.

Figure 2.22: Power transformer at Paraimo substation.

REN is also in charge of the transportation of gas in pipelines of approximately 1375 km, mostly on the coast of Portugal (see appendix B.2). Although the effect of GICs in pipelines can be computed (Viljanen, 1989; Viljanen et al., 2006; Pulkkinen et al., 2001), it is outside the scope of this thesis.

In the framework of the MAG-GIC project, the study of GICs in the national power network started for the south region of Portugal. This was due to the existence of a simple 3D conductivity model for the South of Portugal and the fact that there exist only two voltage levels of the transmission network (150 kV and 400 kV). Transmission lines between substations have lengths from 850m to 97km, in this region (Alves Ribeiro et al., 2021).

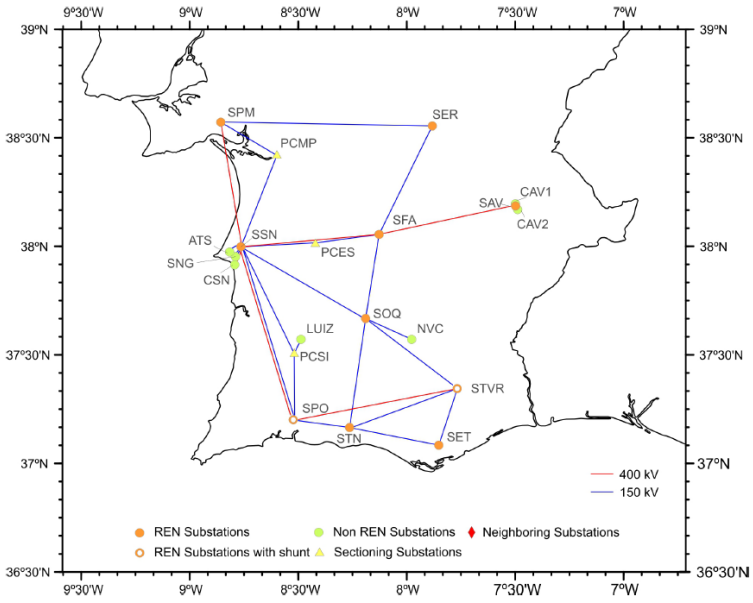

Figure 2.23: Portuguese south region network (Alves Ribeiro et al., 2021).

REN provided the network information essential for GIC modeling, as location of each substation and its grounding resistances (see Figure 2.23), characteristics of transformers in each substation and transmission line resistances. In chapter 3, both transmission lines between SSN (Sines) and SFA (Ferreira do Alentejo) and between SPM (Palmela) and SB (Setúbal) are used as case-studies.

With the most recent progress in the simulations of GICs in the whole Portuguese network, it is already possible to analyze which substations are more susceptible to high GICs. This simulation was also important to conclude about the order of magnitude of GICs in Portuguese territory. As stated in Alves Ribeiro et al. (2021) regarding the southern region of Portugal, also in the central and northern regions it is not expected GICs above 10A.

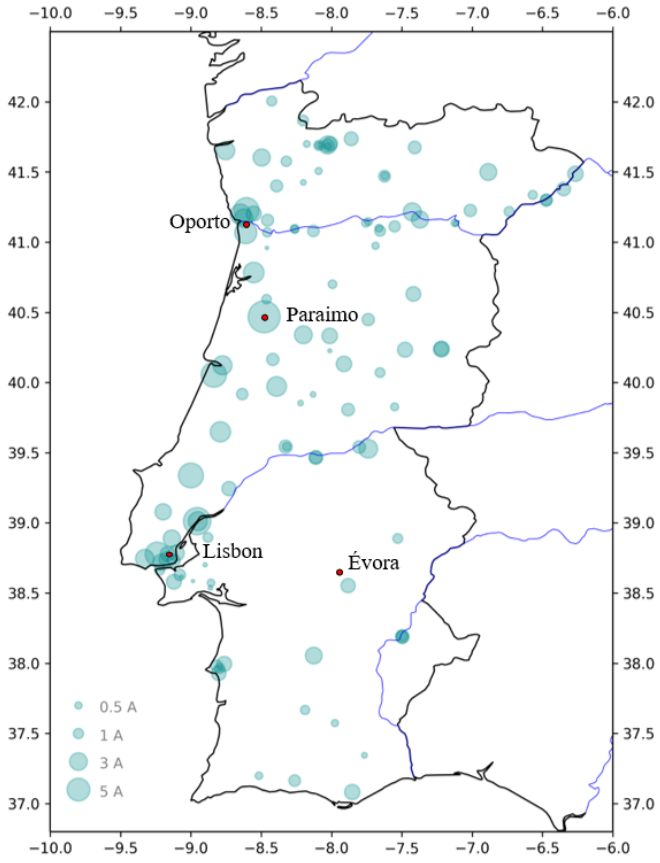

Figure 2.24: GIC estimated values for each Portuguese substation during St. Patrick Storm (Alves Ribeiro et al., communication at IAGA2021).

Figure 2.24 shows one of the results of preliminary simulations including all substations of the national power grid (Alves Ribeiro et al., communication at IAGA2021) during St. Patrick Storm in 2015. Note that the northern region has higher GICs than the southern region. One of the reasons is that in the northern region the granites predominate, while in the South there are more sedimentary rocks. Granite is typically more resistive than sediments so GICs tend to flow more easily into the power transmission grid in these regions. Taking this into consideration and considering that transmission lines at the highest 400kV voltage level have lower line

resistances, Paraimo substation (SPI, denomination given by REN) was chosen to install the GIC measuring system.

Figure 2.25 shows the variations of the magnetic field measured by COI magnetometer and a magnitude proportional to the GIC module at Paraimo Substation also during St. Patrick Storm.

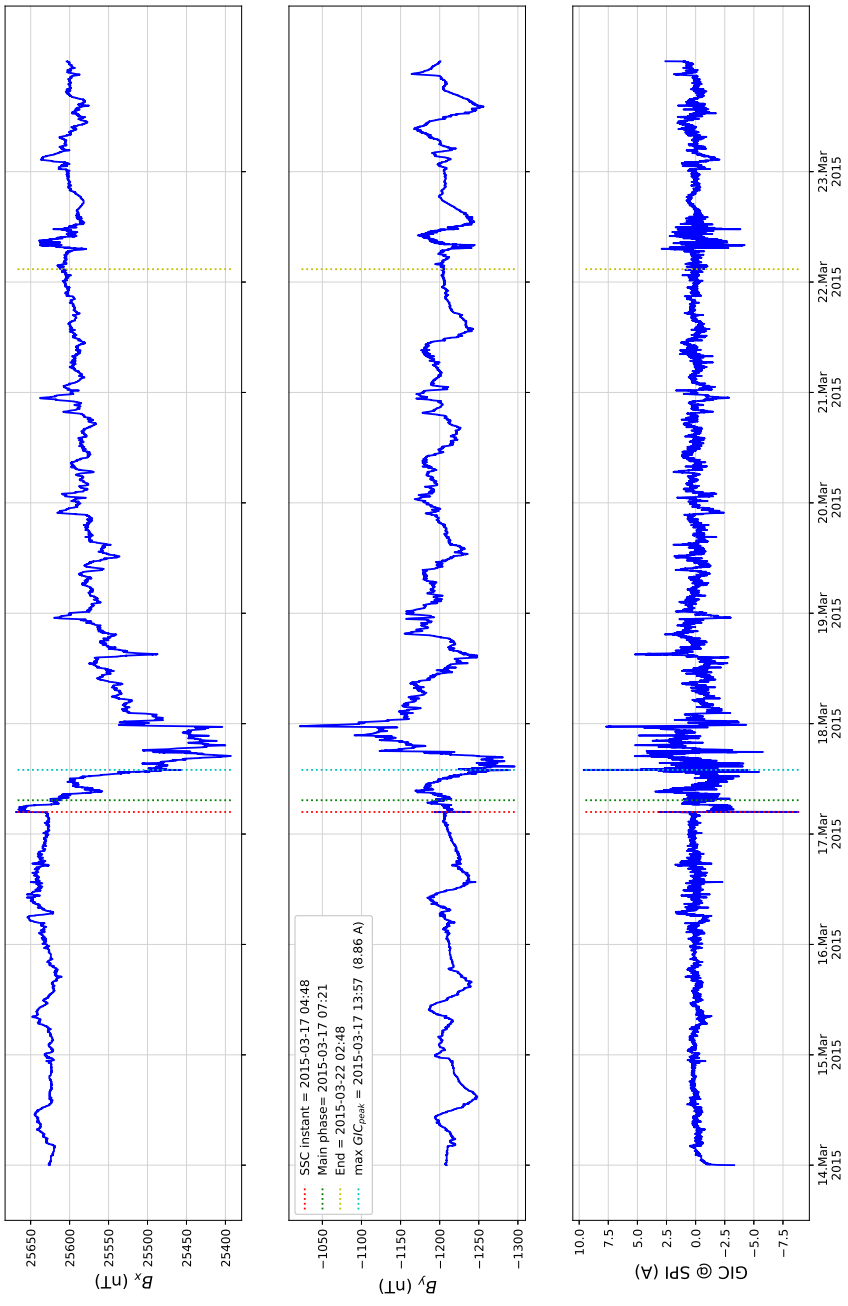

Figure 2.25: Magnetic field variations recorded at COI and GIC estimations at Paraimo Substation also during St. Patrick Storm. Credits due to F. Pinheiro.

Chapter 3

Effect of Shield Wires on computed GICs

Contents

3.1 Power networks with shield wires

Transmission power grids are protected by overhead shield wires, which main purpose is to protect the phase lines from atmospheric storms such as lightning strikes (Figure 3.1).

There are different types of shield wire connections to the substation and to pylons. According to Liu et al. (2020) the scenarios more commonly found are

- shield wires connected to the ground at each pylon as well as at substations at the end of the transmission line.

- shield wires connected to the ground at each substation, but not directly connected to the ground at each pylon.
- shield wires connected to the ground at each pylon, but not directly connected to the ground at each substation.

Likewise power transmission lines, shield wires can carry GICs because they are extended grounded conductors and so represent an extra path.

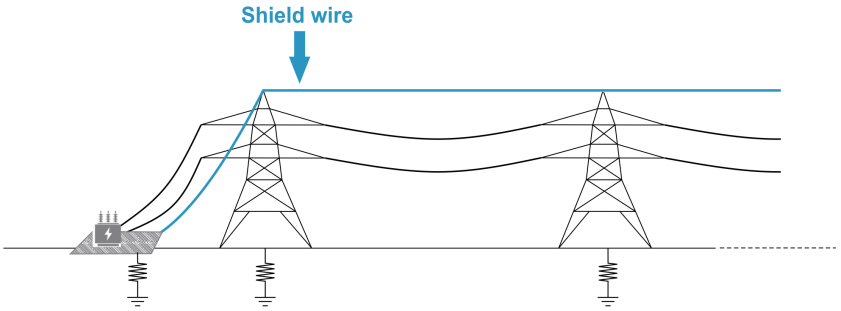

Figure 3.1: Power network with shield wires. Credits due to J.A. Ribeiro.

In the Portuguese power system network, shield wires are connected to the ground at each pylon and at each substation (first case above).

3.2 Elementary circuit model for power lines with shield wires

The large majority of GIC studies do not consider shield wires as a parameter in the models, neither for the induced geoelectric field along these conductors nor for their resistances. Nonetheless, Meliopoulos et al. (1994) carried out a study using the nodal analysis method, where the network model integrated besides a single transmission line and the nonlinear magnetization of transformer cores, also a shield wire connecting the two substations. They concluded that using shield wires could lead to significant differences in the calculation of GIC intensity, but did not study the effect of shield wires separately. Also Pirjola (2007), he modeled the influence of shield wires in the calculation of the induced voltage sources. He concluded that, for long lines, the distortion in the induced voltage due to shield wires was of the order of magnitude of the uncertainty due to the limited knowledge on the geophysical induced field itself and needed not be considered. More recently, Liu et al. (2020) showed that shield wires influence GIC calculation by changing the effective grounding resistance of the substations and sustained that neglecting shield wires lead to an error higher than 10%.

Liu et al. (2020) suggested a simple circuit model as a first approach to analyze the effect of shield wires on GICs in power systems (Figure 3.2). The meaning of the parameters used is explained in Table 3.1. This circuit consists of two substations and one transmission line as well as one shield wire between them. The shield wire

is grounded at each pylon and at both substations. Regarding the transmission line, the three phases are treated as one in the equivalent circuit, whose resistance (R_L) is one-third of that of a single phase, and carrying a GIC (I_L) three times larger than that flowing in a single phase (Meliopoulos et al., 1994). The reason why there are only resistances in the equivalent circuit, leaving out power system inductance and capacitance is because GICs are considered a quasi-DC current and the flow of these currents can be determined by resistances only (Bernhardi et al., 2008b). The electric field induced in the Earth ($\vec{E}$) by geomagnetic storms is at the origin of induced voltages along the grounded network (V_L and V_i in Figure 3.2).

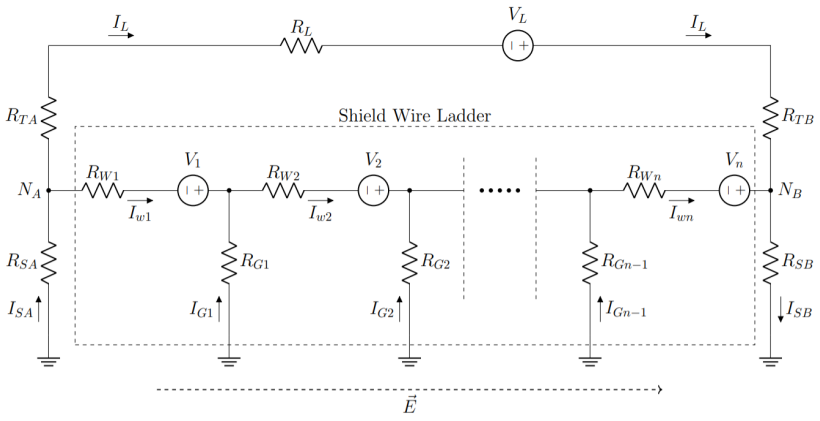

Figure 3.2: Elementary circuit model to analyze the effect of shield wires on GICs through the transformers.

N_A and N_B	neutral points at two substations
R_{SA} and R_{SB}	grounding resistances of substations
R_{TA} and R_{TB}	resistances of transformers at the substations
R_L	resistance of the transmission line between two substations
R_{W1}, R_{W2}, ..., R_{Wn}	resistances of the shield wire within each span length
R_{G1}, R_{G2}, ..., $R_{G(n-1)}$	footing resistances of the pylons
$\vec{E}$	induced geoelectric field
V_L	induced voltage source along the transmission line
V_1, V_2, ..., V_n	induced voltage sources along each shield wire span

Table 3.1: Parameters values used in Figure 3.2.

3.2.1 Derivation of the circuit matrix equations

Applying a mesh current analysis to the circuit in Figure 3.2, the matrix equation of the circuit can be written. This allows to calculate the value of GIC in transformer neutrals (current that will pass through resistances R_{TA} and R_{TB}) without doing any approximation or simplification in the circuit. By analyzing the elements of the matrix, it further allows to generalize to a circuit of arbitrary number of shield wire spans.

To derive the matrix equation, the following loops are considered:

- **Loop 0:** mesh which includes the transmission line and all the shield wire ladders.
- **Loop 1:** mesh which includes the first shield wire ladder, the footing resistance of the first pylon and the grounding resistance of the left substation.
- **Loop 2:** mesh which includes the second shield wire ladder and the footing resistances of the first and second pylons.
- **Loop n:** mesh which includes the last shield wire ladder, the footing resistance of the last pylon and the grounding resistance of the right substation.

The equation which relates all currents and the equations of each loop follows:

$$I_{SA} + I_{G1} + I_{G2} + ... + I_{G(n-1)} = I_{SB} \tag{3.1a}$$

$$I_{G(n-1)} = I_{SB} - I_{SA} - I_{G1} - I_{G2} - ... - I_{G(n-2)} \tag{3.1b}$$

Loop 0:

$$\begin{aligned} -(R_L + R_{TA} + R_{TB})I_L + V_L \\ +R_{W1}(-I_L + I_{SA}) - V_1 \\ +R_{W2}(-I_L + I_{SA} + I_{G1}) - V_2 \\ +... \\ +R_{Wn}(-I_L + I_{SA} + I_{G1} + I_{G2} + ... + I_{G(n-1)}) - V_n = 0 \end{aligned} \tag{3.2}$$

Loop 1:

$$R_{W1}(-I_L + I_{SA}) - R_{G1}I_{G1} + R_{SA}I_{SA} = V_1 \tag{3.3}$$

Loop 2:

$$R_{W2}(-I_L + I_{SA} + I_{G1}) - R_{G2}I_{G2} + R_{G1}I_{G1} = V_2 \tag{3.4}$$

Loop n:

$$\begin{aligned} R_{Wn}(-I_L + I_{SA} + I_{G1} + I_{G2} + ... + I_{G(n-1)}) \\ +R_{SB}I_{SB} + R_{G(n-1)}I_{G(n-1)} = V_n \end{aligned} \tag{3.5}$$

Note, as a particularity of this circuit with induced voltage sources, that V_L and V_i are not all independent and the following relation applies: $V_L = \sum_{i=1}^{n} V_i$.

Rearranging the above equations, a general matrix equation can be written, with which is possible to calculate all currents in the circuit:

$$[A][I] = [V] \tag{3.6}$$

with A, I and V in appendix A.

The GIC currents are then obtained by solving numerically

$$[I] = [A]^{-1}[V] \tag{3.7}$$

In order to check for the accuracy of the derived matrix equation, tests were done using LTSpice. This is a high performance simulation software, schematic capture and waveform viewer with models to facilitate simulation of analog circuits. It also includes macromodels for a wide range of devices such as switching amplifiers and regulators.

3.3 Equivalent circuit with only shield wire resistances

The circuit in Figure 3.2 can be very complex and computationally heavy, for a very large number of shield wire spans. So, an interesting procedure would be to try to simplify this circuit and get a faster way to calculate GICs in that circuit model.

3.3.1 The model in Liu et al. (2020)

Figure 3.3 represents the simplified model adopted by Liu et al. (2020), where shield wire and grounded pylons (Figure 3.4) are treated as an equivalent parallel resistance R_{eq}, which changes the effective ground resistance of the substation. This model does not take into account the equivalent voltage sources of the geoelectric field within each span length (V_i).

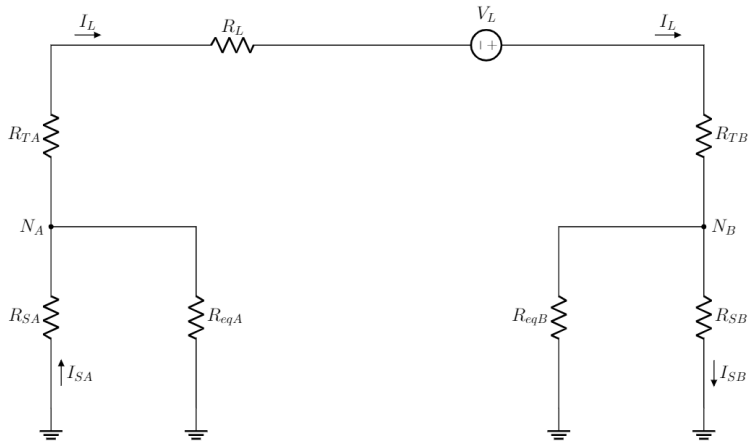

Figure 3.3: Equivalent circuit model considering only resistances along shield wires.

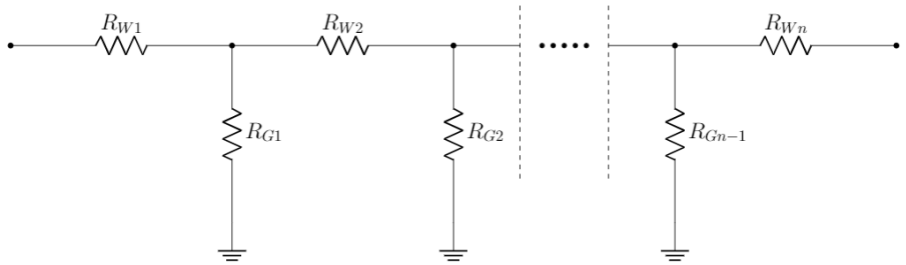

Figure 3.4: Shield wire and grounded pylons circuit.

The steps to get this simplified circuit follow. Assuming that in the ladder circuit model of Figure 3.4 :

$$R_{W1} = R_{W2} = ... = R_{Wn} = R_W \tag{3.8}$$

$$R_{G1} = R_{G2} = ... = R_{Gn-1} = R_G \tag{3.9}$$

and grouping the resistances as shown in the Figure 3.5, the equivalent resistance of the ladder circuit can be expressed as

$$R_{eqi} = R_W + \frac{R_{eq(i-1)} \times R_G}{R_{eq(i-1)} + R_G} \tag{3.10}$$

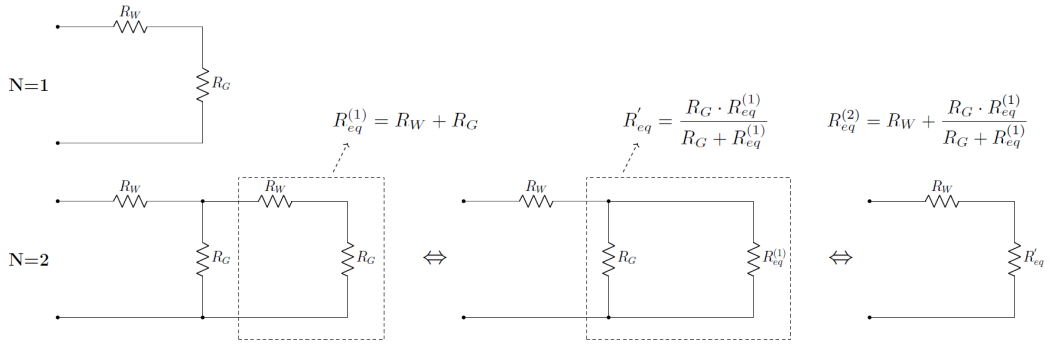

Figure 3.5: Grouping R_W and R_G resistances.

Figure 3.6 shows the variation of the equivalent resistance of the ladder circuit (R_{eqi}) with the number i of ladder steps.

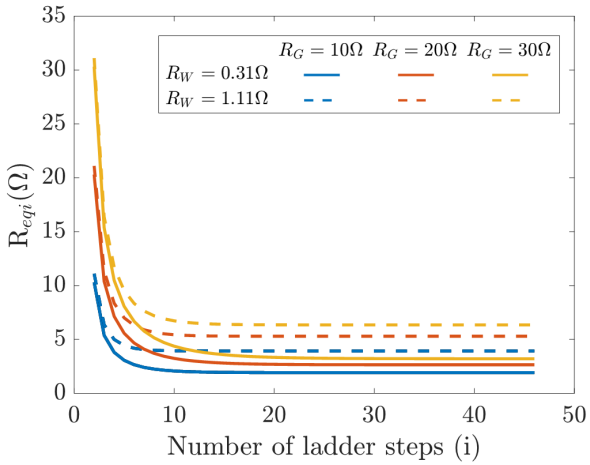

Figure 3.6: Equivalent resistance R_{eqi} of the ladder circuit for increasing ladder size.

From Figure 3.6 it can be seen that R_{eqi} is converged, in all cases, after the 30^{th} ladder step. Assuming that $R_W << R_G$ (as is usual the case in transmission power lines), then the converged value is given by:

$$R_{eq} = \frac{R_W}{2} + \sqrt{R_W \times R_G} \tag{3.11}$$

R_{eq} is connected in parallel to each substation grounding resistance, changing it to $R'_S = \frac{R_S \cdot R_{eq}}{R_S + R_{eq}}$. The resulting GIC current in the transmission line as well as in the transformers (I_L) and through the substations grounding resistances (I_{SA} and I_{SB}) is then:

$$I_L = \frac{V_L}{R_L + R_{TA} + R_{TB} + R'_{SA} + R'_{SB}} \tag{3.12}$$

$$I_{SA} = I_L \cdot \frac{R_{eq}}{R_{eq} + R_{SA}} \tag{3.13}$$

$$I_{SB} = I_L \cdot \frac{R_{eq}}{R_{eq} + R_{SB}} \tag{3.14}$$

3.4 Derivation of the equivalent circuit including storm-induced emfs

As explained in section 3.2.1, the effect of storm-induced emfs can be explicitly included in the estimation of GICs in simple circuits as that of Figure 3.2, using the matrix equation. However, such matrix equations lead to large time consuming computations when the number of shield wire spans is large. Based on the study by Liu et al. (2020), the next step in this study was to derive an equivalent circuit as simple as that in Figure 3.3, but now considering both resistance and induced voltage sources along each shield wire span (Figure 3.7). It is comparable with Figure 3.3 however, it additionally includes the effect of the induced voltage source along each

shield wire span. Note that the polarity of the voltage source terminal connected to one and the other substations' neutral points is symmetric. With this simple circuit, the heavy computational task of modeling the shield wire system explicitly may be bypassed.

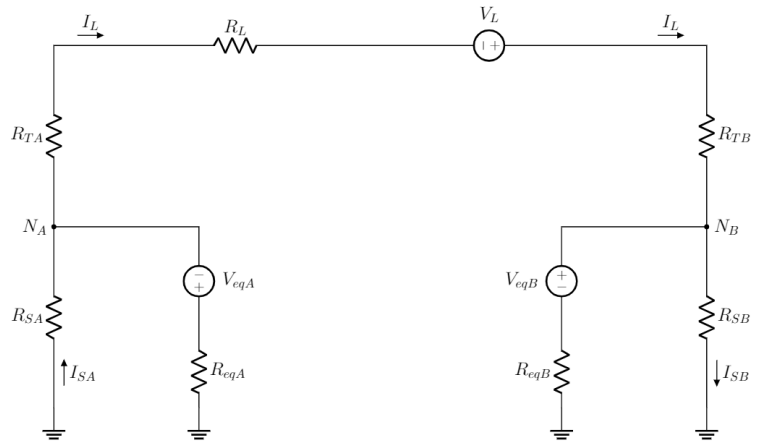

Figure 3.7: Equivalent circuit model considering the resistances and the induced voltage sources along shield wires.

The method used to derive values for V_{eq} and R_{eq} in the circuit of Figure 3.7 will be explained in the next subsections.

3.4.1 Recursive equations

From the side of substation A, the circuit connected to R_{SA} is a group of resistances and voltage sources arranged in ladders (Figure 3.8) with n loops in total.

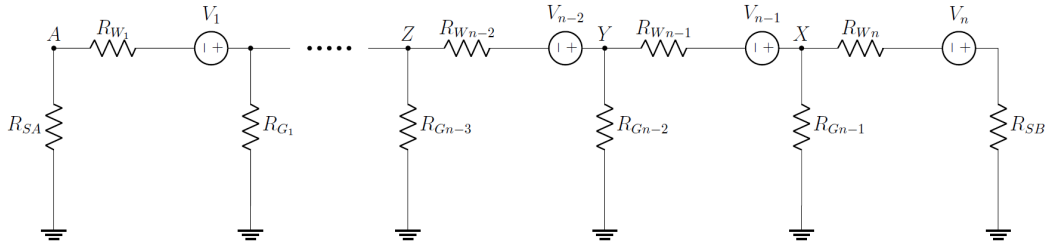

Figure 3.8: Circuit connected to R_{SA}.

Figure 3.8 shows the shield wire circuit to be simplified. Starting with the farmost step of the ladder circuit from the left substation connecting point (A) in the ladder, the one which includes R_{SB}, Thevenin's theorem can be applied (Figure 3.9 left) to get an equivalent circuit as shown in Figure 3.9 (right).

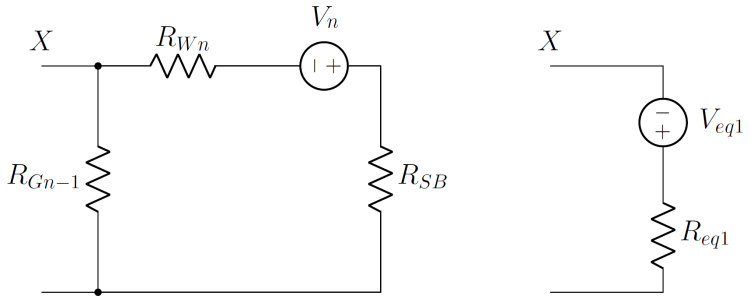

Figure 3.9: Left) first step of the ladder circuit; Right) Thevenin equivalent of the first ladder step.

The equivalent resistance in the Thevenin equivalent circuit (R_{eq1}) is the resistance seen in the load with the source in short circuit, that is,

$$R_{eq1} = R_{G(n-1)}//(R_{Wn} + R_{SB}) = \frac{R_{G(n-1)} \cdot (R_{Wn} + R_{SB})}{R_{G(n-1)} + R_{Wn} + R_{SB}} \tag{3.15}$$

And the equivalent voltage (V_{eq1}) (the voltage seen in the load with the circuit open) is obtained by multiplying the load $R_{G(n-1)}$ by the current in the isolated loop,

$$V_{eq1} = V_n \cdot \frac{R_{G(n-1)}}{R_{G(n-1)} + R_{Wn} + R_{SB}} \tag{3.16}$$

Adding the contiguous ladder step to the first Thevenin's equivalent circuit, the circuit in Figure 3.10 (left) is obtained. Then, the Thevenin's theorem is applied again Figure 3.10 (right).

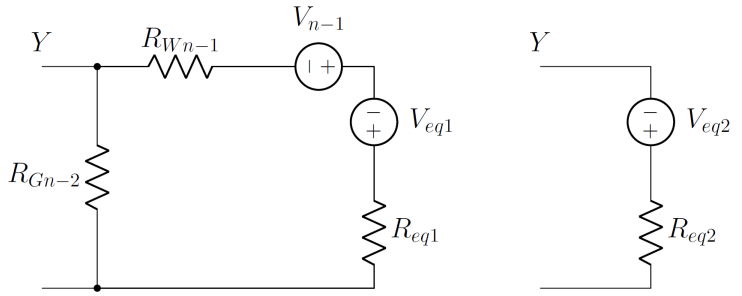

Figure 3.10: Left) first and second steps of the ladder circuit; Right)Thevenin equivalent of the first two ladder steps.

The equivalent resistance of Thevenin R_{eq2} is similarly obtained as R_{eq1}:

$$R_{eq2} = R_{G(n-2)}//(R_{W(n-1)} + R_{eq1}) = \frac{R_{G(n-2)} \cdot (R_{W(n-1)} + R_{eq1})}{R_{G(n-2)} + R_{Wn-1} + R_{eq1}} \tag{3.17}$$

To calculate the equivalent voltage V_{eq2}, first it is necessary to obtain the current i in the closed loop shown in 3.10 (left):

$$i = \frac{(V_{n-1} + V_{eq1})}{R_{G(n-2)} + R_{W(n-1)} + R_{eq1}} \tag{3.18}$$

With this expression, V_{eq2} can be also obtained.

$$V_{eq2} = (V_{n-1} + V_{eq1}) \cdot \frac{R_{G(n-2)}}{R_{G(n-2)} + R_{W(n-1)} + R_{eq1}} \tag{3.19}$$

Adding more ladder steps, one at a time, the same procedure leads to expressions for the Thevenin resistances and voltage sources that are identical to 3.17 and 3.19. As they can show, to compute values at a given ladder step i requires knowledge of values computed in step i-1. The general recursive equations are the following:

$$R_{eqi} = R_{G(n-i)}//(R_{W(n-i+1)} + R_{eq(i-1)}) = \frac{R_{G(n-i)} \cdot (R_{W(n-i+1)} + R_{eq(i-1)})}{R_{G(n-i)} + R_{W(n-i+1)} + R_{eq(i-1)}} \tag{3.20}$$

$$V_{eqi} = (V_{(n-i+1)} + V_{eq(i-1)}) \cdot \frac{R_{G(n-i)}}{R_{G(n-i)} + R_{W(n-i+1)} + R_{eq(i-1)}} \tag{3.21}$$

These equations allow to compute resistance and voltage source equivalents from iteration number 2 to n-1. This last equivalent will be added in parallel with R_{SA}, having in mind that it is important to keep the R_{SA} branch as a distinct branch, in order to calculate the current which passes through the grounding resistance of the substation.

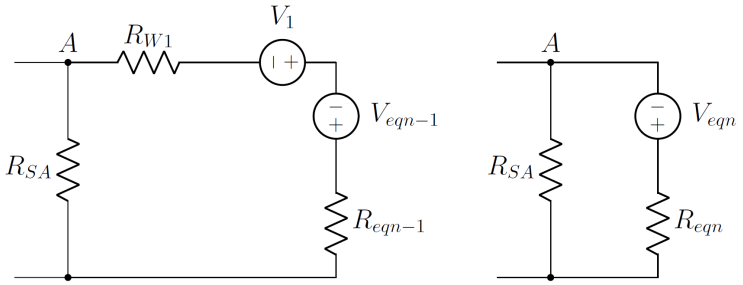

Figure 3.11: Left) last step of the ladder circuit; Right) Thevenin equivalent of n steps of the ladder circuit.

$$R_{eqA} = R_{eqn} = R_{eq(n-1)} + R_{W1} \tag{3.22}$$

$$V_{eqA} = V_{eqn} = V_{eq(n-1)} + V_1 \tag{3.23}$$

3.4.2 Behavior of recursive sequences

The equations derived above take a simpler form if the following simplification is applied

$$R_{W1} = R_{W2} = ... = R_{Wn} = R_W$$
$$R_{G1} = R_{G2} = ... = R_{Gn-1} = R_G$$

$$V_1 = V_2 = ... = V_n = V$$

Simplifying equations 3.15, 3.16, 3.20 and 3.21, yields

$$R_{eq1} = (R_W + R_{SB}) \cdot \frac{R_G}{R_G + R_W + R_{SB}} \tag{3.24}$$

$$V_{eq1} = V \cdot \frac{R_G}{R_G + R_W + R_{SB}} \tag{3.25}$$

$$R_{eqi} = (R_W + R_{eq(i-1)}) \cdot \frac{R_G}{R_G + R_W + R_{eq(i-1)}} \tag{3.26}$$

$$V_{eqi} = (V + V_{eq(i-1)}) \cdot \frac{R_G}{R_G + R_W + R_{eq(i-1)}} \tag{3.27}$$

The sequence values that represent the Thevenin equivalent resistance and voltage source for increasing number i of ladder steps are plotted in Figure 3.12, with R_{SB}, R_W, R_G and V as the only parameters that need to be defined. It can be seen that R_{eqi} as well as V_{eqi} approach an asymptotic value after a large enough number of steps.

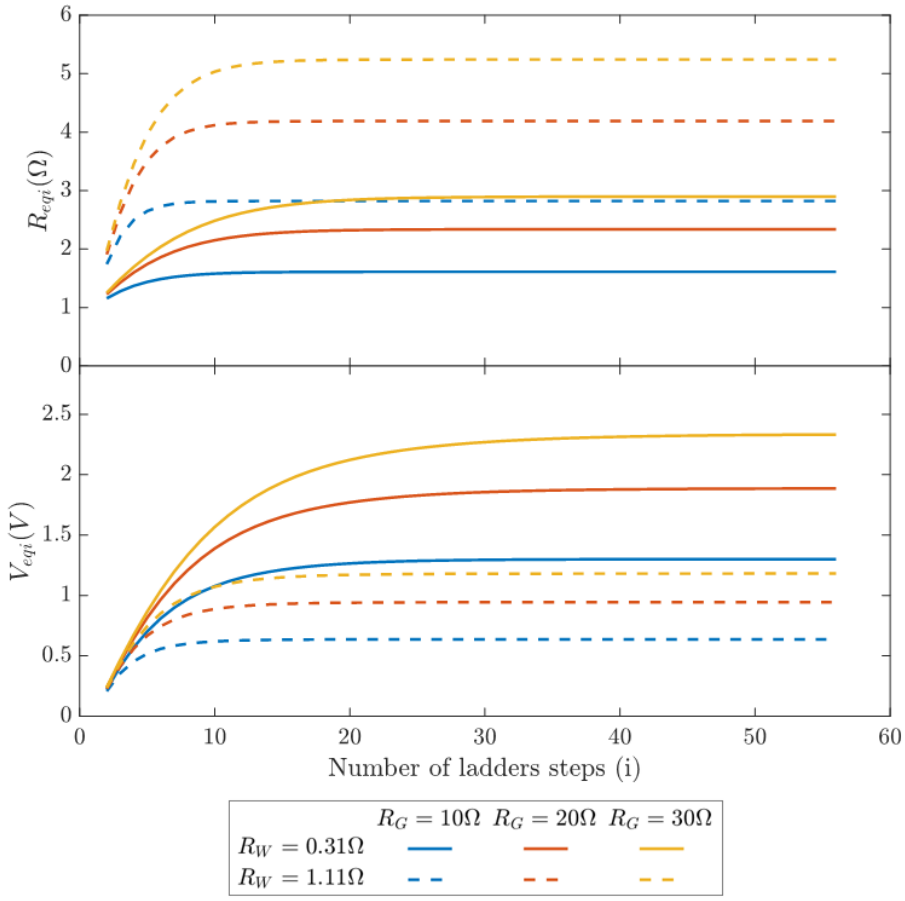

Figure 3.12: R_{eqi} and V_{eqi} of the ladder circuit for increasing number of ladder steps. V=0.5 V and different values of R_W and R_G.

3.4.3 Asymptotic expressions

From Figure 3.12, R_{eqi} reaches a stable value when i is large enough. The plateau value depends on the combination of parameters and tends to be higher for higher R_W and higher R_G. As can also be seen, the number of steps to reach the asymptote depends on the parameters R_W and R_G: the smaller (R_W/R_G), the slower the convergence.

In the asymptotic regime, $R_{eq(i-1)} \sim R_{eqi} = R_{asy}$. Using this approximation in the recursive equation for the equivalent resistance (equation 3.26), it yields

$$R_{asy} = \frac{R_G \cdot (R_W + R_{asy})}{R_G + R_W + R_{asy}} \tag{3.28}$$

This gives a quadratic equation and a solution:

$$R_{asy} = -\frac{R_W}{2} + \frac{1}{2}\sqrt{R_W^2 + 4R_W \cdot R_G} \tag{3.29}$$

Because in general $R_W \ll R_G$, R_W^2 in equation 3.29 can be neglected and the following expression for R_{asy} is obtained

$$R_{asy} = -\frac{R_W}{2} + \sqrt{R_W \cdot R_G} \tag{3.30}$$

Figure 3.12 also shows the dependence of V_{eqi} on the increasing order of the ladder step i. It can be seen that V_{eqi} approaches a stable value within ~ 30 ladder steps, at most. The rate at which the asymptote is reached depends again on the parameters R_W and R_G: the smaller (R_W/R_G), the slower the convergence. As to the plateau value, it is higher for higher R_G/R_W, but also for higher induced emf V (not shown in Figure 3.12).

For large iteration i, V_{eqi} reaches a stable value where $V_{eq(i-1)} \sim V_{eqi} = V_{asy}$. Using this approximation in equation 3.27, then

$$V_{asy} = (V_{asy} + V) \cdot \frac{R_G}{R_G + R_W + R_{asy}} \tag{3.31}$$

Solving the equation in order to V_{asy}, it can be obtained

$$V_{asy} = V \cdot \frac{R_G}{R_W + R_{asy}} \tag{3.32}$$

and finally, replacing the R_{asy} result from equation 3.30, the final expression for the converged value of the equivalent voltage source is obtained.

$$V_{asy} = V \cdot \frac{R_G}{\frac{R_W}{2} + \sqrt{R_W \cdot R_G}} \tag{3.33}$$

To check for the accuracy of the derived asymptotic expressions, relative differences between the predicted values from equations 3.30 and 3.33 and values from equations 3.26 and 3.27, respectively, were computed using i=90 to reach the asymptotic limit. Results are shown in Table 3.2.

For the test parameters, it stands out that the obtained asymptotic expressions represent very closely the behavior of the corresponding recursive sequences when

$i \geq 90$. In fact, the approximation for $i = 30$ is also very good, with errors below 2%. Also note that the approximation is so much better as the approximation $R_W << R_G$ is valid.

R_G (Ω)	R_W (Ω)	V (V)	V_{eqi} (V)	V_{asy} (V)	$error$ (%)	R_{eqi} (Ω)	R_{asy} (Ω)	$error$ (%)
30	1.11	0.05	0.2361	0.2371	0.4210	5.2422	5.2156	0.5079
		0.1	0.4723	0.4743	0.4210			
	0.31	0.05	0.4675	0.4681	0.1235	2.8985	2.8946	0.1358
		0.1	0.9350	0.9361	0.1235			
10	1.11	0.05	0.1271	0.1286	1.1812	2.8226	2.7767	1.6265
		0.1	0.2542	0.2572	1.1812			

Table 3.2: V_{eqi} and R_{eqi} values obtained from equations 3.26 and 3.27 with n=90 and the V_{asy} and R_{asy} obtained from equations 3.30 and 3.33 for different values of R_W, R_G and V. The resistance and voltage errors are calculated with the following equations $error(\%) = \frac{|R_{asy} - R_{eqi}|}{R_{asy}}$ and $error(\%) = \frac{|V_{asy} - V_{eqi}|}{V_{asy}}$, respectively, using i=90.

3.4.4 Equivalent shield-wire circuit at each substation

A very practical outcome of the asymptotic behavior of the recursive sequences is that expressions 3.30 and 3.33 can be used to characterize the Thevenin equivalent to the shield wire system, as long as the line lengths are large enough and the shield wire ladder parameters R_G and R_W, as well as the induced voltage source V , are homogeneous along the line.

Using the asymptotic expressions 3.30 and 3.33 in equations 3.22 and 3.23, the following equations for the equivalent parameters in Figure 3.7 are finally obtained:

$$R_{eq} = \frac{R_W}{2} + \sqrt{R_W \cdot R_G} \tag{3.34}$$

$$V_{eq} = V \cdot \left[\frac{R_G}{\frac{R_W}{2} + \sqrt{R_W \cdot R_G}} + 1 \right] \tag{3.35}$$

As in the equivalent circuit with only shield wire resistances (Figure 3.3), equations for I_L and I_{SA} (as for I_{SB}) were obtained for the circuit in Figure 3.7. R_{eq} and V_{eq} are connected in parallel to each substation grounding resistance. So $R'_S = \frac{R_S R_{eq}}{R_S + R_{eq}}$ and $V' = V_{eq} \cdot \frac{R_S}{R_S + R_{eq}}$ can be written and allow to characterize the equivalent circuit to connect to each substation.

$$I_L = \frac{V_L - V'_B - V'_A}{R'_{SA} + R'_{SB} + R_L + R_{TA} + R_{TB}} \tag{3.36}$$

$$I_{SA} = \frac{V_{eq} + I_L \cdot R_{eq}}{R_{SA} + R_{eq}} \tag{3.37}$$

$$I_{SB} = \frac{V_{eq} + I_L \cdot R_{eq}}{R_{SB} + R_{eq}} \tag{3.38}$$

Note that in the case V=0, the above 3.36 to 3.38 equations give exactly the same results 3.12 to 3.14 from Liu et al. (2020).

In the following section, it will be discussed in which conditions the equivalent circuit in Figure 3.7, with the parameters derived above, may be used in practice.

3.5 Application using real values from the Portuguese power network

The next step of this study was to apply both equivalent circuits (Liu's et al. and the circuit derived in this study) to real lines with real parameters and discuss possible improvements for the modeling of GICs. Therefore a briefly characterization of two lines in the Portuguese power network follows as well as the application of both equivalent circuit models to those two lines.

3.5.1 Characterization of the case-study lines

The national transmission system operator - REN - has provided relevant information for testing this study with realistic values from the Portuguese power network. Having access to this information is important to make it clear which range of values is usual in the Portuguese energy transmission network. Indeed, the use of very accurate real values is not required because this particular line does not exist alone but connected to a large number of other lines.

REN provided information of two different size lines: the line between Ferreira do Alentejo and Sines called LFA.SN, which has a voltage level of 400kV, and the much shorter line between Palmela and Setúbal called LPM.SB1, which has a voltage level of 150kV (see Figure 3.13). The characterization of both lines follows.

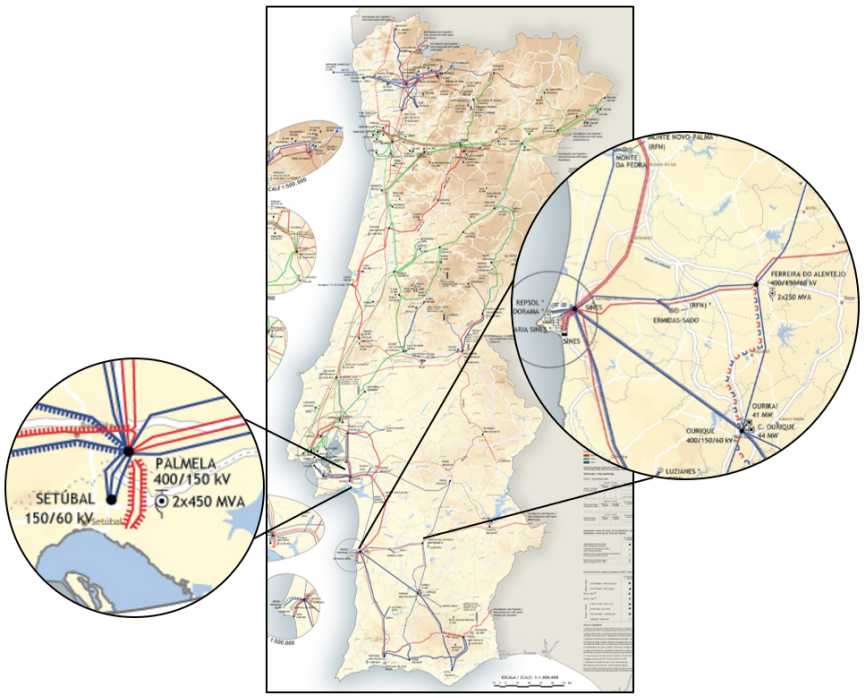

Figure 3.13: Location of the two lines that will be studied in this thesis.

LFA.SN line: Ferreira do Alentejo - Sines

The line between Ferreira do Alentejo and Sines (LFA.SN), which has 170 pylons, is shown in Figure 3.14 and characterized by the parameter values shown in Table 3.3.

On June 22^{th}, 2015 occurred a geomagnetic storm for which the estimated induced voltage source between the neutral points A and B was 7.0V (considering the ground conductivity model in Alves Ribeiro et al. (2021)). Then we use this value for V_L.

Line length (L)	59970 m
R_L	6.07 Ω
R_{TA}	0.80 Ω
R_{TB}	0.35 Ω
R_{SA}	0.10 Ω
R_{SB}	0.12 Ω
$\overline{R_{Wi}}$	0.126 Ω
$\overline{R_{Gi}}$	5.2 Ω

Table 3.3: Line length and resistance values for the line between Ferreira do Alentejo (substation A) and Sines (substation B).

Figure 3.14: Location and R_{Gi} values for each pylon i in LFA.SN line.

Knowing the values in Table 3.3, the R_{Gi} value for each pylon (see Figure 3.14) as well as the distance d_i (in meters) between consecutive pylons, all parameters of interest were calculated through the following equations.

$$V_i = V_L \cdot \frac{d_i}{L} \tag{3.39}$$

$$R_{Wi} = R_W \cdot \frac{d_i}{350} \tag{3.40}$$

$R_W = 0.1258\Omega$ is the resistance of 350 m of shield wire, for the material in use. Then V_i and R_{Wi} are the emf and wire resistance for each shield wire span. It is assumed that the electric field induced is uniform along the line.

LPM.SB1 line: Palmela - Setúbal

The line between Palmela and Setúbal (LPM.SB1), which has 13 pylons, is characterized by the values that are shown in Table 3.4 and Figure 3.15. For the same June 22^{th}, 2015 storm, the estimated value for V_L was 1.0V.

Line length (L)	4793.5 m
R_L	0.289 Ω
R_{TA}	0.049 Ω
R_{TB}	0.049 Ω
R_{SA}	0.10 Ω
R_{SB}	0.10 Ω
$\overline{R_{Wi}}$	0.122 Ω
$\overline{R_{Gi}}$	3.5 Ω

Table 3.4: Line length and resistance values for the line between Palmela (substation A) and Setúbal (substation B).

Figure 3.15: Location and R_{Gi} values for each pylon i in LPM.SB1 line.

As in the previous line, the equivalent voltage sources along each shield wire span due to the induced geoelectric field (V_i) and the R_{Wi} values can be calculated through equation 3.39 and 3.40.

3.5.2 Testing both equivalent circuit models

These two lines were used as case studies to test both equivalent circuits: the Liu et al circuit and the circuit derived in this study. Table 3.5 shows all I_L, I_{SA} and I_{SB} values calculated from different circuit models: (1) the complete (or true) circuit (Figure 3.2); (2) the circuit without shield wires; (3) the equivalent circuit with only resistance along shield wires (1^{st} equivalent circuit, Figure 3.3) and (4) the equivalent circuit with both resistance and emfs along shield wires (2^{nd} equivalent circuit, Figure 3.7). In the last two cases, R_W and R_G are mathematical averages of all R_{Wi} and R_{Gi} values. Errors were obtained through $error(\%) = \frac{|I_c - I_e|}{I_c}$ where I_c is the current calculated from the complete circuit and I_e is the current calculated through other circuits.

		LPM.SB1	**error**	**LFA.SN**	**error**
$\boldsymbol{I_L}$ (A)	complete circuit	1.603	-	0.939	-
	without shield wires	1.704	6.32 %	0.941	0.18 %
	1^{st} equivalent circuit	1.778	10.93 %	0.944	0.50 %
	2^{nd} equivalent circuit	1.596	0.428 %	0.935	0.412 %
$\boldsymbol{I_{SA}}$ (A)	complete circuit	1.819	-	0.883	-
	without shield wires	1.704	6.30 %	0.941	6.54 %
	1^{st} equivalent circuit	1.560	14.22 %	0.847	4.11 %
	2^{nd} equivalent circuit	1.912	5.134 %	1.132	28.17 %
$\boldsymbol{I_{SB}}$ (A)	complete circuit	1.869	-	1.080	-
	without shield wires	1.704	8.82 %	0.941	12.85 %
	1^{st} equivalent circuit	1.560	16.52 %	0.830	23.13 %
	2^{nd} equivalent circuit	1.912	2.308 %	1.109	2.742 %

Table 3.5: I_L, I_{SA} and I_{SB} values for LPM.SB1 and LFA.SN lines calculated with the complete circuit, with the circuit without shield wires, with the equivalent circuit with only shield wire resistances (*1^{st} equivalent circuit*) and with the equivalent circuit with both shield wire resistances and emfs (*2^{nd} equivalent circuit*).

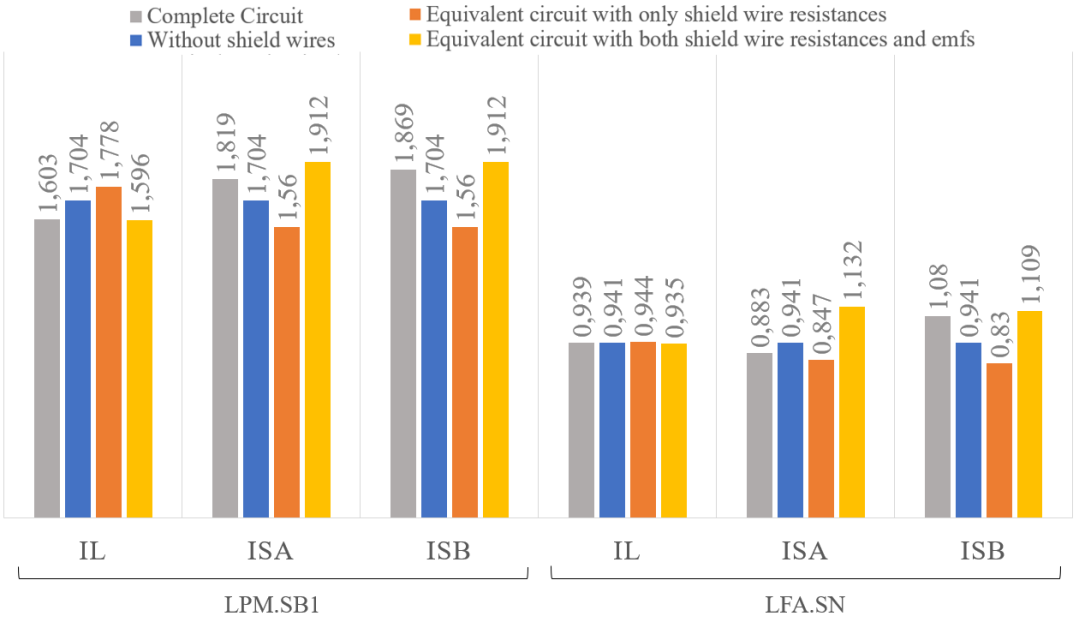

Figure 3.16: Graphical scheme of the values in Table 3.5

From this Figure, LPM.SB1 line presents higher current values than LFA.SN line due to lower R_T values (an order of magnitude lower). The decrease in the total line resistance compensates for the decrease in V_L.

When using the circuit model without shield wire on LPM.SB1 line, errors are above 6% (6.32%, 6.30% and 8.82%, respectively). Errors are also significant when using the equivalent circuit model with only shield wire resistances, i. e., errors above 10% (10.93%, 14.22% and 16.52%, respectively). However, if the equivalent circuit model with both shield wire resistances and emfs were used, errors are below 6% (0.43%, 5.13% and 2.31%, respectively). In short, and for the LPM.SB1 line, using the 2^{nd} equivalent circuit represents an improvement not only compared to neglecting shield wires, but also compared to using the 1^{st} equivalent circuit to model the shield wires effect.

For the LFA.SN line, the error of using either the circuit model without shield wires, or the equivalent circuit model with only shield wire resistances or the equivalent circuit model with both shield wire resistances and emfs in the current flowing through the transformer is below 1%. The current through the grounding resistance R_{SA} at substation A presents an higher error when using the equivalent circuit model with both shield wire resistances and emfs. The current through R_{SB} at the substation B presents an higher error when using the equivalent circuit model with only shield wire resistances. Higher errors associated to the current through R_{SA} must be clarified.

3.5.3 Discussion

The different reasons that could justify those errors are (1) the consequence of using mean values from scattered resistance values; (2) the small size of the LPM.SB1 line; the 13 pylons may not satisfy the asymptotic condition of the expressions used or (3) the consequence of not considering the equivalent voltage source in each shield wire ladders (V_i), in the case of the equivalent circuit model with only shield wire resistances. The examination of these simplifications one by one follows, to prove the direct influence of the use of emfs along the shield wires in the LPM.SB1 line and also to find explanations for the I_{SA} and I_{SB} errors in the LFA.SN line.

1. *R_{Wi} and R_{Gi} highly scattered:*
   Both models consider R_{Wi} and R_{Gi} have fixed values and for that mean values are computed (R_W and R_G).

LPM.SB1 line			
R_G	$\sigma^2_{R_G}$	R_W	$\sigma^2_{R_W}$
3.5 Ω	5.1 Ω	0.122 Ω	0.002 Ω

LFA.SN line			
R_G	$\sigma^2_{R_G}$	R_W	$\sigma^2_{R_W}$
5.2 Ω	60.2 Ω	0.126 Ω	0.001 Ω

Table 3.6: Mean and variance values for R_{Gi} and R_{Wi} of both lines.

Table 3.6 shows that R_{Gi} values are very scattered because have high variance, being the LFA.SN line the most influenced. In fact, Figure 3.14 presents a wide range of values.

To measure this specific error, the values of the complete circuit can be compared with the same circuit but replacing the individual values of R_{Gi} and R_{Wi} for their means, R_G and R_W (Table 3.7).

LPM.SB1 line		
I_L	I_{SA}	I_{SB}
0.4 %	3.7 %	0.9 %

LFA.SN line		
I_L	I_{SA}	I_{SB}
0.4 %	28.0 %	2.6 %

Table 3.7: Error associated from using mean values instead of real values in the complete circuit for both lines.

As R_{Gi} and R_{Wi} values in LPM.SB1 line are not very dispersed, low errors were predictable. On the other hand, LFA.SN line presents a higher error for I_{SA}, just as we see in Table 3.5. This suggests that R_{Gi} values are more far from the mean near substation A and for that reason, the use of average values along the line instead of real values is influencing the I_{SA} calculation.

2. *R_{eqi} and V_{eqi} asymptotic limits:*
   In the case of the smaller line (LPM.SB1), a relevant question is whether the

asymptotic limit has already been reached. This can be easily tested by confirming if n=13 pylons is a sufficient number of pylons to achieve the converged value in R_{eqi} (equations 3.10 or 3.26) and in V_{eqi} (equation 3.27). Calculating $R_{eq(i=13)}$ and $V_{eq(i=13)}$, all deviations are less than 3%.

3. *V_i not considered:*
   In the case of the equivalent circuit model with only shield wire resistances, the induced voltage source in the shield wire ladder (V_i) was neglected and the implications of this simplification can also be tested by comparing the complete circuit with the same circuit but with $V_i = 0$. The errors follow.

LPM.SB1 line		
I_L	I_{SA}	I_{SB}
12.2 %	17.6 %	17.6 %

LFA.SN line		
I_L	I_{SA}	I_{SB}
0.8 %	25.1 %	25.1 %

Table 3.8: Errors due to neglecting V_i in the complete circuit for both lines.

Here, results are very interesting. Not only there are errors associated with I_{SA} and I_{SB} but also with I_L which is the current of interest (since it flows through the transformer windings). In LPM.SB1 line, the I_L error calculated is 12.2% which can not be neglected.

To conclude, the errors in Table 3.5 can be explained, considering the reasons mentioned above. Regarding LPM.SB1 line, it can be confirmed that the errors of using the equivalent circuit with only shield wire resistances is only due to not considering the emfs along shield wires. When using the equivalent circuit with both shield wire resistances and emfs, errors are negligible. In the case of the LFA.SN line, I_L errors from using both equivalent circuits are negligible. In the case of the I_{SB}, the error is also associated to when emfs are neglect. As for the I_{SA} error associated to the use of the equivalent circuit with both shield wire resistances and emfs is due to the use of R_G and R_W mean values.

Thus, it was confirmed that, in the case of lines of the Portuguese power network where the line size is not very high, ignoring the induced voltage source is incorrect and leads to significant errors. On the other hand, in the case of large dispersion of R_G values, the equivalent circuits are probably not a better solution compared to neglecting shield wires.

3.6 Towards more complex circuits

In a real power transmission network, a substation neutral point has multiple lines connected to it. For this reason, the model presented in the previous section was tested including more lines connected to the neutral point and also more transformers in the model. The main purpose of this extra analyses is to understand what happens to the value of estimated GICs when adding more lines to the circuit.

The first step towards a higher degree of complexity was to consider a two-line model (2-line-model) with three transformers and two phase lines connecting them (Figure 3.17). The transformer A has both lines connected to it and Figure 3.18 represents the corresponding equivalent circuit.

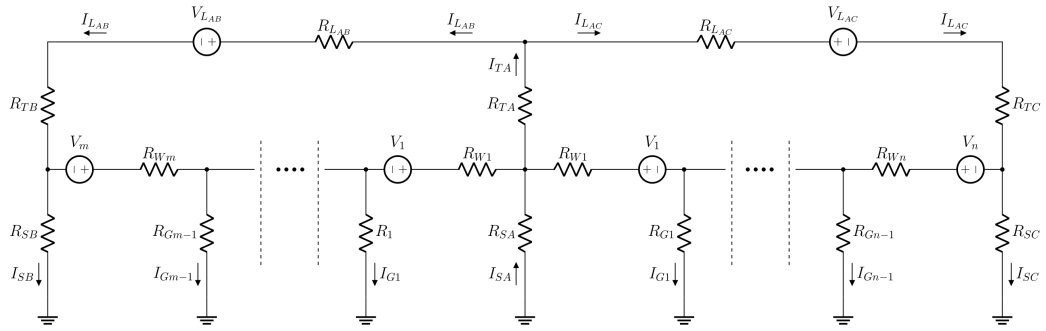

Figure 3.17: Circuit model with two phase lines and three transformers (2-line-model).

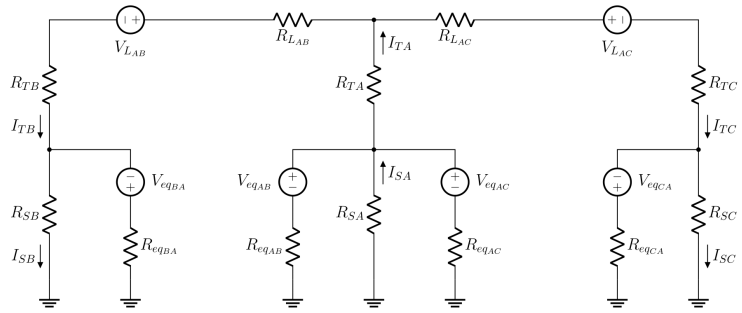

Figure 3.18: Equivalent circuit concerning circuit in Figure 3.17.

The second model was a three-line model with also three transformers, each of them having two phase lines connected to them, as in a triangle. Figure 3.19 represents this circuit and the corresponding equivalent is in Figure 3.20 ($\triangle$-3-line-model).

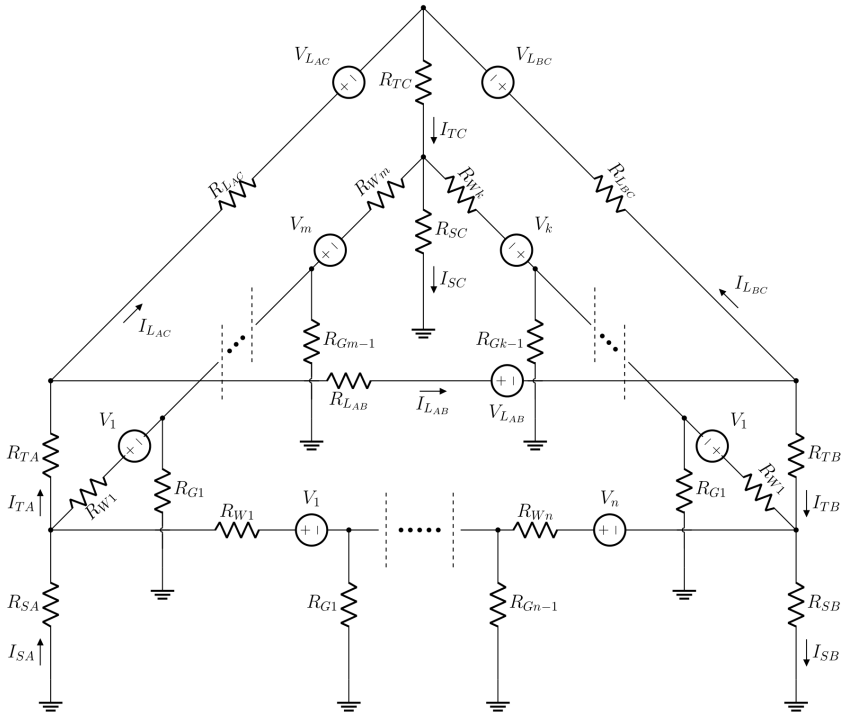

Figure 3.19: Circuit model with three phase lines and three transformers (△-3-line-model).

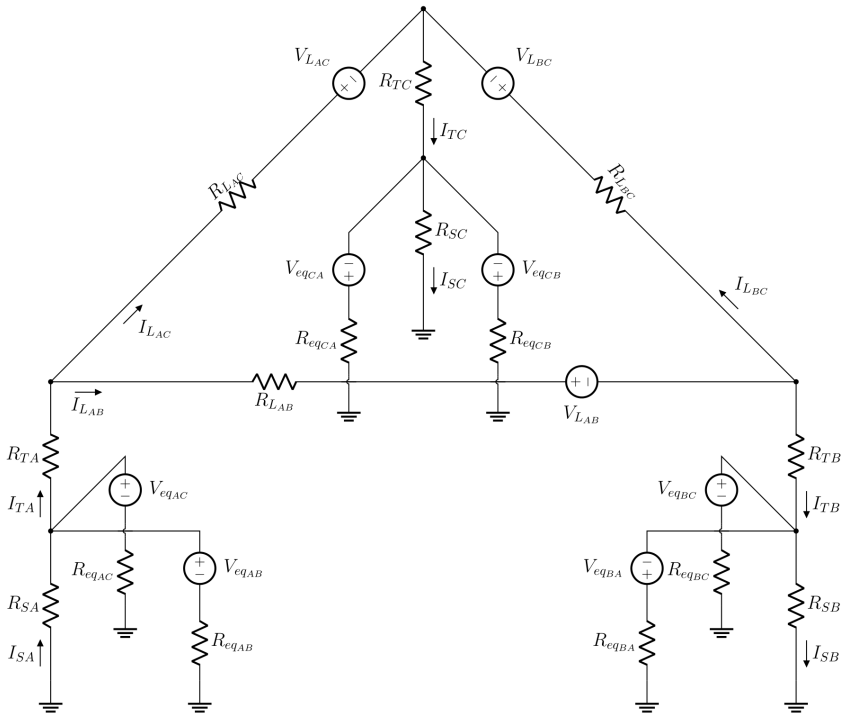

Figure 3.20: Equivalent circuit concerning circuit in Figure 3.19.

Finally, the last circuit model studied was also a three phase line model with all lines connected to transformer A as in a star configuration ($\star$-3-line-model).

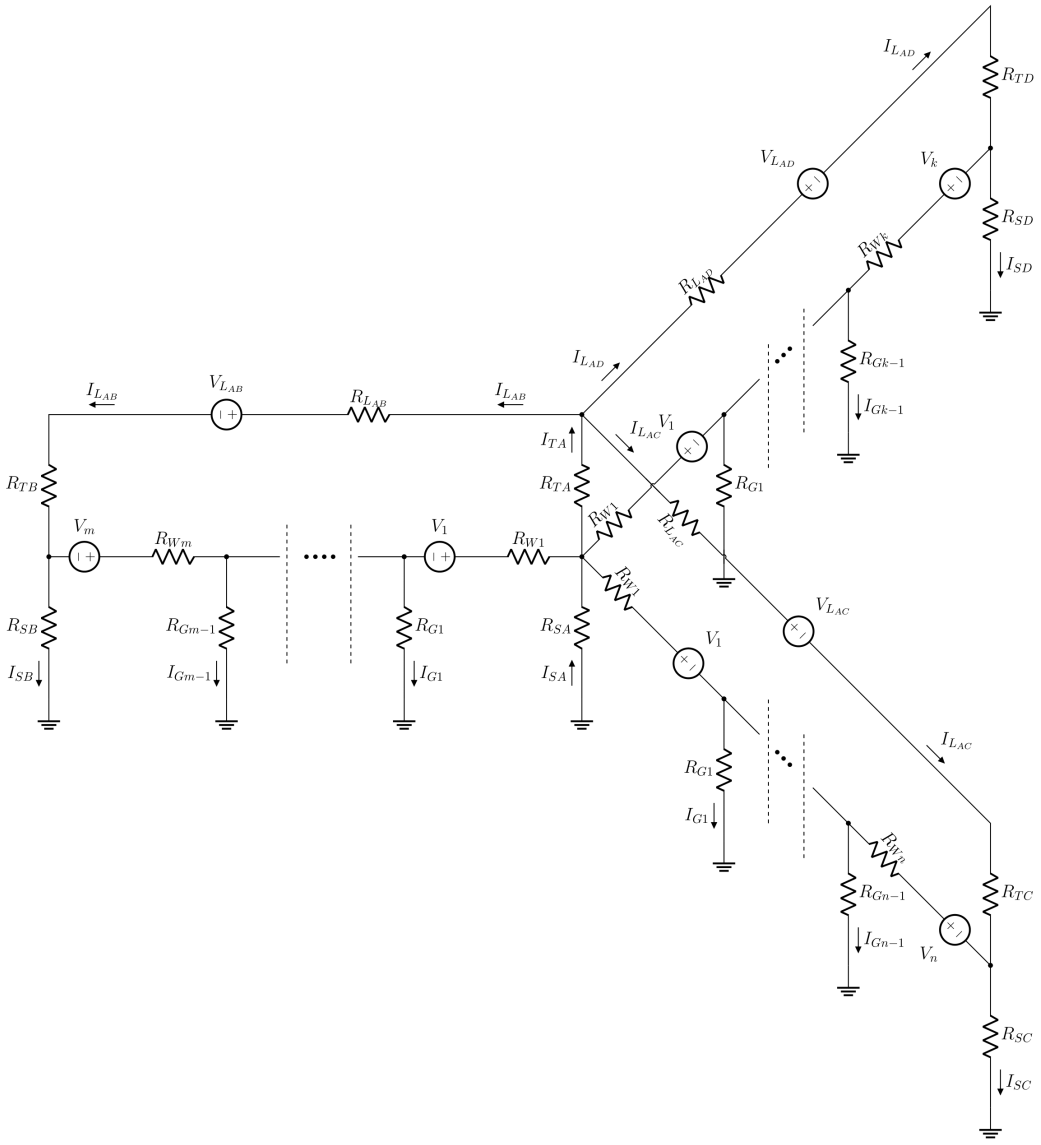

Figure 3.21: Circuit model with three phase lines and three transformers ($\star$-3-line-model).

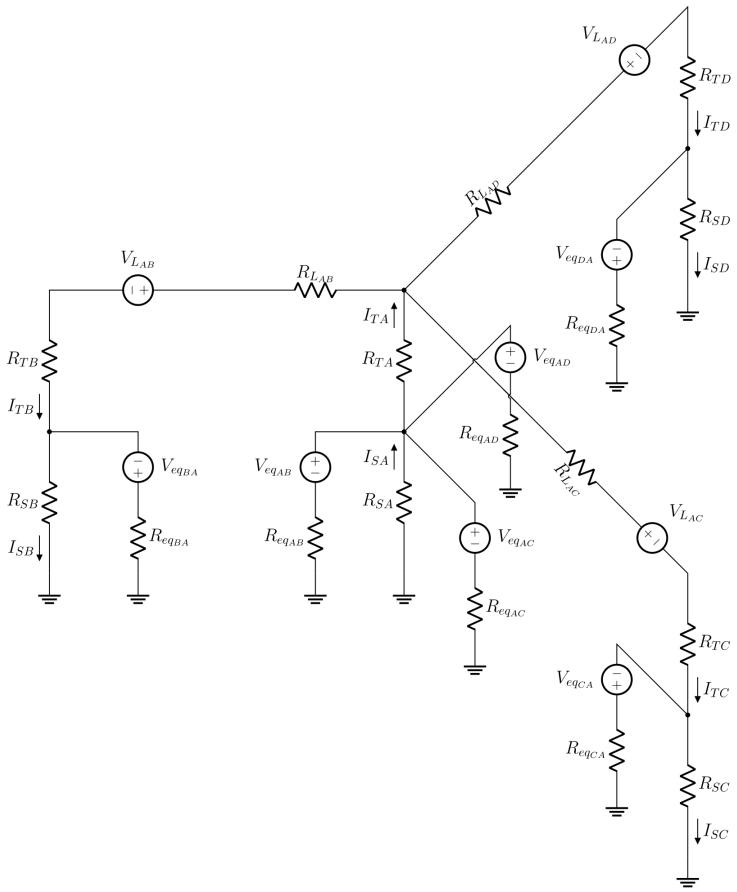

Figure 3.22: Equivalent circuit concerning circuit in Figure 3.21.

Table 3.9 shows all parameters used in all network models in this section.

R_L	0.289 Ω
$R_{TA} = R_{TB} = R_{TC} = R_{TD}$	0.049 Ω
$R_{SA} = R_{SB} = R_{SC} = R_{SD}$	0.10 Ω
R_G	3.0 ± 2.0 Ω
V_L	1.0 V
d_i	350 ± 100 m
n	13

Table 3.9: Network parameters used in this section.

	Single-line-model		2-line-model	
	I_{TA}	error	I_{TA}	error
Complete circuit	1.6027	-	2.5824	-
Without shield wires	1.7036	6.30%	2.7174	5.23 %
Equivalent circuit with only R_{eq}	1.7778	10.93 %	2.9311	13.50 %
Equivalent circuit with R_{eq} and V_{eq}	1.5959	0.42 %	2.5509	1.22 %

Table 3.10: I_{TA} values in the single-line model and two-line model. Errors are calculated comparing with the complete circuit.

	$\triangle$-3-line-model		$\star$-3-line-model	
	I_{TA}	error	I_{TA}	error
Complete circuit	2.6884	-	3.2526	-
Without shield wires	2.7174	2.99 %	3.3898	4.09 %
Equivalent circuit with only R_{eq}	2.9686	12.51 %	3.8191	17.27 %
Equivalent circuit with R_{eq} and V_{eq}	2.5939	1.69 %	3.1973	1.82 %

Table 3.11: I_{TA} values in the $\triangle$-3-line-model and $\star$-3-line-model. Errors are calculated comparing with the complete circuit.

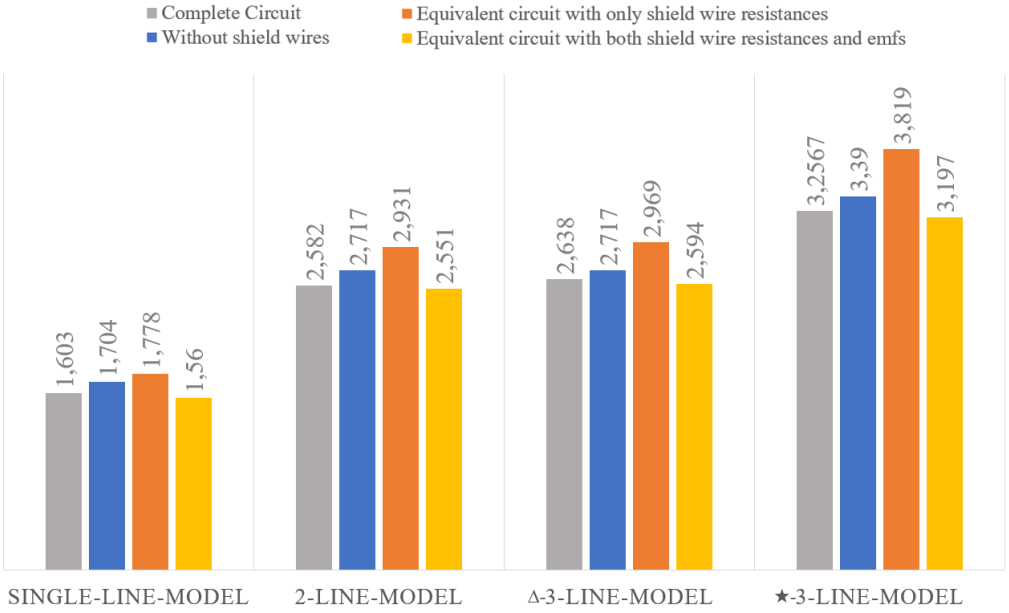

Figure 3.23: Graphical scheme of the values in Tables 3.10 and 3.11

With these circuits and preliminary tests, it is possible to conclude:

- As the number of lines connected to the transformer increases, the GICs also increase (1.60A-2.58A-3.25A);
- As the number of lines connected to the transformer increases, the error associated by using the equivalent circuit with only shield wire resistances increases (11%-13%-17%);
- The error for using the circuit model without shield wires remains approximately constant;
- In the case of 2 lines connected to the transformer, there is not much difference whether the other two transformers are also connected by a line ($\triangle$-3-line-model) or not (2-line-model);

Chapter 4

Development of GIC measurement instrumentation

Contents

4.1 Introduction

Given the different assumptions taken for the calculations, GIC estimated results are not enough to conclude on the magnitude of GICs flowing in the network. Thus, measurements should be taken in order to validate predicted GIC values. The first instrumental system for GIC measurements on the Portuguese transmission network is discussed in this chapter as well as its performance analysis in laboratory.

The system developed during this thesis is the follow-up of an already started prototype (see Cardoso et al. (2019)). This chapter presents the main components of a prototype system design to continuously measure GICs.

4.2 Requirements Analysis

The first step in designing a GIC measurement system is to clarify and list all requirements and restrictions, as is done in Table 4.1.

Starting with the input data type, this system has to measure an analogue signal proportional to a quasi-DC current flowing in the transformer neutral and convert it to digital data. An user interface would be convenient too, like a dashboard showing the real-time acquired data and with the possibility of doing simple data processing or downloading selected data to a file.

The functionality of this system is to measure an analogue signal, convert it to a digital signal with an ADC converter, apply some signal filtering and save this information in a database. This database should be locally or remotely reachable by interested parts. Because GICs are quasi-DC currents (see chapter 2.3), even if the sampling frequency is of the order of kHz, it can be downsampled to 1Hz.

The current must be measured with a non-invasive sensor for the power transmission network. To this end, it is preferable that the cable be enclosed by the sensor, without the need to disconnect the neutral cable from the ground. In this way, it will be easier to make the system mobile, by making it easy to disassemble for maintenance or move to another transformer.

Concerning the system's performance, it has to measure a range from ±1mA up to ±50A and it should guarantee a precision of at least tenths of amperes because the magnitude will be below 10A, most of the time.

Since this system will be built to acquire data in a continuous mode for several months, power consumption should be provided from local supply (230V 50Hz) instead of a battery.

Functional requirements	
Ability to measure a quasi-DC current and save that information in a database to be accessed later at any time	
Non-functional requirements	
Performance	**Accessibility**
Input currents from 1mA up to 50A Precision of tenths of amperes Sampling frequency of 1Hz	Easy and quick installation on the transformer Remote access to measured data
Security	**Usability**
Remote access only by authorized users	Simple interface with access to the measured data
Power	**Storage Capacity**
Local Power Supply 230V 50Hz	Several months
Space	
40mm cable entry hole diameter	

Table 4.1: System requirements.

There are some physical constraints that have to be clarified, such as the cable diameter and exterior restrictions such as the presence of other cables or structures around. By contacting the Portuguese operator REN, it was possible to find out that the standard diameter of the cable used for the transformers' neutrals is 40mm.

Lastly, the system must be weatherproof, ideally with IP65 enclosure specifications. It was decided that a protective cover could be done on site and it was decided to open some ventilation vents (active and passive) to guarantee proper cooling of the electronic and sensing elements.

4.3 Architecture

4.3.1 Sensing

The main component of the system is the current sensor because it will most directly influence the sensitivity of the entire system. The sensitivity of the sensor is defined as the ratio between the variation range of the output quantity and the variation range of the input quantity.

As it was said before, the sensor shouldn't be invasive to the power grid, thus a Hall effect sensor is the best choice. A Hall effect sensor is a current transducer that measures a certain magnetic field nearby, having an output voltage directly proportional to the strength of the field. Figure 4.1 shows a scheme of how an open loop Hall effect sensor works. A primary current I_P flowing through a wire induces a magnetic field (B) in the sensor core according to Biot-Savart law. This magnetic field is concentrated by a magnetic core and is proportional to I_P. The core has a gap cut through it and a Hall generator is used to sense the magnetic flux density in the gap. In this Hall generator, there is a control current (I_C) applied. The presence of a magnetic field, perpendicular to the direction of the current, deflects the charge carries, producing a difference in electric potential (V_H) between the two sides of the Hall generator. This signal is then amplified and the output signal of the sensor is V_{OUT}.

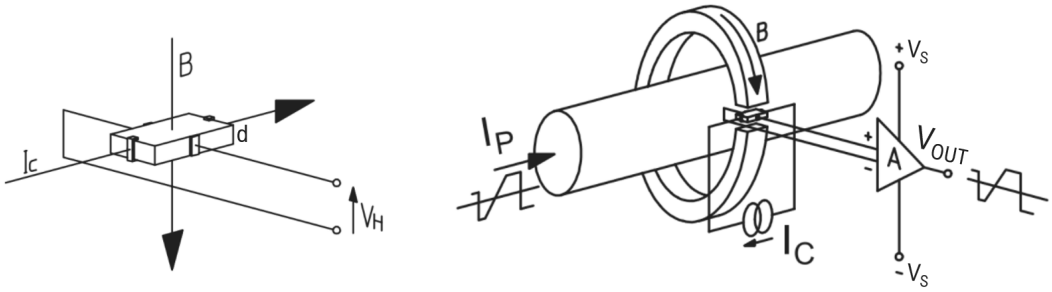

Figure 4.1: Conversion of the primary current I_P into an output voltage V_{OUT} in an open loop Hall effect sensor. From LEM Components Brochure.

From the arrangement described above and from LEM Components Brochure, the following equation is verified:

$$V_H = \frac{K}{d} \cdot I_c \cdot B + V_{OH} \tag{4.1}$$

where K is the Hall constant of the conducting material, d is the thickness of the sheet, and V_{OH} is the offset voltage of the Hall generator, i.e., the output voltage of the Hall generator in the absence of an external field. Such an arrangement is referred to as a Hall generator and the product $K/d \cdot I_C$ is generally referred to as the Hall generator sensitivity. Both sensitivity and offset voltage are usually temperature dependent.

Looking at the sensor as a whole, i. e., considering the Hall generator and the amplifier, the output voltage (V_{OUT}) is given by equation:

$$V_{OUT} = \alpha I_P + V_O \tag{4.2}$$

where α is the sensor sensibility, V_O is the sensor offset voltage.

The Hall effect sensor chosen was an Open Loop Current Transducer HOP 1000-SB from LEM (see Figure 4.2 and Table 4.2 for main specifications). The main reason for this choice was the 40 mm height of the rectangular hole, essential for the transformer's neutral cable to fit. Another determinant reason was being a split-core sensor, which means that the sensor will embrace the neutral cable with no need to disconnect it from the ground. The only downside of the sensor is its wide dynamic range, i. e., its input nominal current is between 0 and 1000A, which is a much wider range than what is expected to measure. As a matter of fact, most sensors with lower dynamic range have too small hole dimensions, so they are non-viable for this project.

Specifications	
Series	LEM HOP 1000-SB
Primary Nominal RMS Current (RMS(I_P))	$1000A$
Output Voltage (V_{OUT})	$\pm 4V$
Supply Voltage (V_S)	$\pm 12 - 15V$
Current Consumption (I_C)	$\leq 20mA$
Accuracy	$\leq \pm 2\%$
Electrical Offset Voltage (V_{OE})	$\leq \pm 20mV$
Magnetic Offset Voltage (V_{OM})	$\leq \pm 20mV$
Op. Temperature	$-10C/70C$
Temperature variation of V_O	$\leq \pm 25mV$
Rectangular hole size	$104 \times 40mm$

Table 4.2: Current Transducer HOP 1000-SB specifications. Total offset voltage $V_O = V_{OE} + V_{OM}$.

Figure 4.2: Current Transducer HOP 1000-SB.

Since the sensor takes bipolar measurements, the maximum variation amplitude is 2000A and the output signal is ±4V for the 2 directions of the current, therefore the sensitivity of the sensor (α value in equation 4.2) is, directly from factory specifications, 4 mV/A . In the following, it will be shown that laboratory tests give a very close value.

4.3.2 Data Acquisition

In order to quantify the signal measured by the Hall effect sensor, an input channel in the ADC with a channel width larger than the sensor's sensitivity is required. Generally, an N-bit ADC has a resolution (channel width) of:

$$V_{OUT_{LSB}} = \frac{\Delta V_{OUT}}{2^N - 1}(V/bit) \tag{4.3}$$

$$I_{P_{LSB}} = \frac{\Delta I_P}{2^N - 1}(A/bit) \tag{4.4}$$

with $\Delta V_{OUT} = 8V$ and $\Delta I_P = 2000A$, LSB is the *Least Significant Bit*.

Since currents above 10A are not expected, the choice of ADC channel width resolution should be at least one order of magnitude below the sensor's sensitivity (see Table 4.3). Given this criterion, 16 bits of resolution is the minimum required. Note that this is a theoretical analysis and is performed on a noiseless scenario. To minimize noise, the ADC should make a minimum sampling rate on the order of 1000 samples per second, to average the input signal on the order of 10^3.

N-bit ADC (bits)	$V_{OUT_{LSB}}$ **(mV/bit$_{LSB}$)**	$I_{P_{LSB}}$ **(A/bit$_{LSB}$)**
8	31.13	7.78
10	7.80	1.95
12	1.95	0.49
16	**0.12**	**0.031**
18	0.031	0.00763
24	0.00048	0.000119

Table 4.3: Output signal and nominal current resolutions values for different N-bit ADC of an acquisition channel.

The best solution found was to use a Raspberry Pi 4 Model B with a high resolution 24-bit digitizer shield. This configuration is more useful than Arduino because it allows more processing (C or Python), network or wireless connectivity, local interface, but above all it allows memory expansion to microSD card to make storage for long periods, as required. Another powerful feature of the Raspberry Pi is the row of GPIO (general-purpose input/output) pins along the top edge of the board that permit an easily connection to an ADC module.

Raspberry Pi unit (see Figure 4.3 and Table 4.5 for main specifications) has 4 GB of memory and has also a micro-SD card slot for data storage as well as for loading operating system. This modular networked platform allows easy Python scripting along with a group of easily interfaceable web services (see section 4.4).

The ADC module used (see Figure 4.4 and Table 4.6 for main specifications) is a Waveshare AD/DA 24 bits Raspberry piggyback module. It is based on an ADS1256 8-channel converter with resolution around $120\mu A/bit$. According to the ADC specifications, the full-scale input voltage is ±5V (bipolar) with a programmable gain of 1 (PGA = 1) (Table 4.4) with a $V_{ref} = 2.5V$. Although better resolutions are achieved with higher gains, especially if the current to be measured is very small, it was chosen to work with PGA=1 to guarantee full-scale for the "worst" case of 1000 A primary current range.

PGA setting	**Full-scale input voltage (V_{REF}=2.5V)**
1	$\pm 5V$
2	$\pm 2.5V$
4	$\pm 1.25V$
8	$\pm 0.625V$
16	$\pm 312.5mV$
32	$\pm 156.25mV$
64	$\pm 78.125mV$

Table 4.4: Full-Scale Input Voltage vs PGA Setting.

The data rate (samples per second) of this ADC and is given by Equation 4.5.

$$DataRate = \frac{f_{CLKIN}}{256} \frac{1}{Num\_Ave} \tag{4.5}$$

where Num_Ave is the number of averages per sample and f_{CLKIN} is the data rate frequency. With a data rate frequency of 7.68MHz, it is possible to make 3000 averages for each sample and have a data rate of 10 samples per second for the 8 channels. Consequently, each channel collects data every 1.25 seconds which means a 0.8Hz data rate (within the frequency range of the GICs).

Raspberry Pi 4 Model B

Figure 4.3: Raspberry Pi 4 Model B.

Specifications	
Supply Voltage	$2.7 - 5.5V$
Consumption	$3.0A$
Memory	4 GB
Ambient Operating Temperature	$0 - 50°C$

Table 4.5: Raspberry Pi 4 Model B specifications.

High-Precision AD/DA DAQ Module

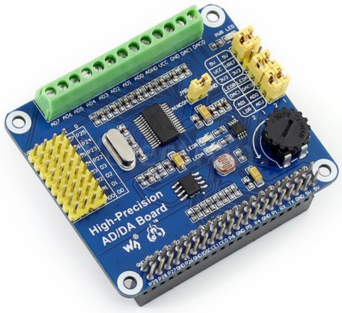

Figure 4.4: High-Precision AD/DA DAQ Module.

Specifications	
Supply Voltage	3.3 or 5 V
Component ADS	ADS1256
Resolution	24 bits
Number of channels	8
Sensitivity	120 $\mu A/bit$

Table 4.6: High-Precision AD/DA DAQ Module specifications.

4.3.3 Casing

All electric components must be protected from ambient weather and significant temperature variations so using IP65 (or higher) specifications for the casing is the best choice. IP (or 'Ingress Protection') ratings are international standards to define levels of sealing effectiveness of electrical casings against intrusion from external bodies. In this case, the most appropriate IP ratings are 65 and 66 which offer full protection against dust and other particles and protection against medium-pressure water jets.

4.3.4 Control System

As the current sensor is sensitive to temperature variations, a continuous temperature monitoring was integrated, even with the system inside an insulated casing. By having a continuous record of the system temperature, it is easy to make a temperature correction of the signal. A TMP36 temperature sensor is used, which has a scale factor of $10mV/°C$ and a power supply of $2.7 - 5.5VDC$.

In addition to temperature monitoring, it was included an active ventilation to prevent overheating of the casings. For these cases, active fans (MC32909 and RDM8025SA) are used.

4.4 Logical Structure

4.4.1 Data Acquisition control and Storage

Raspberry Pi 4 is able to run a Python 3.7 scripting with the instructions to data acquisition and storage. Data is continuously stored to an InfluxDB streaming time series database locally. In this first prototype, the data is saved in a local database and obtained through a micro SD card. Furthermore, a remote connection to the Raspberry Pi is guaranteed.

Python scripting

The script used is an open-source Python code under the PiPyADC library [1]. This code provides access to GPIO and other IO functions on the Raspberry Pi, allowing access to the GPIO pins and consequently to the signals of the Waveshare AD/DA channels.

In this script, the data rate is set to 10 samples per second, and the Hall effect sensor signal as the temperature signal are read and written into a local database (pseudo-code follows).

Algorithm 1 PiPyADC

1: ads ← Initialize ADC object with specified PGA, f_{CLKIN}, data rate and V_{REF} values
2: **while** True **do**
3: $raw\_channels$ ← read input channels
4: $voltages$ ← convert $raw\_channels$ data in voltage values
5: $time$ ← current time in milliseconds
6: $saveInflux$ ← save data in the local database ($voltages$, $time$)
7: **end while**

InfluxDB

InfluxDB is an open-source Time Series Database (TSDB), a database which was developed especially for time series. It means that it optimizes the data for time, and comes with several features to keep the more demanding databases small. This database is optimized for fast, high-availability storage and retrieval of time series data in fields such as Operations Monitoring and Internet of Things sensor data. It provides a similar SQL language, listening on port 8086.

Remote connection - TeamViewer

TeamViewer is a free, fast and safe remote management tool with easy implementation in Raspberry Pi. Setting an ID and password on the Raspberry Pi, it is possible to access it remotely as long as it is connected to the internet. For this purpose, the system also has a mobile internet router.

[1] https://github.com/ul-gh/PiPyADC

4.4.2 Data Visualization

4.4.2.1 Grafana

A commonly used combination is Grafana with InfluxDB (see Figure 4.5 for an example). Grafana is a web application for data visualization through graphical primitives and uses InfluxDB as data source. As InfluxDB supports a huge amount of reads and writes, it is possible to generate graphs in real time and keep a history of years, as well as query old data without causing too much load on the server.

Figure 4.5: Example of Grafana dashboard graphs.

4.5 System Integration

Once all components were chosen, the next step was to integrate everything into a single functional system. The system consists in 2 casings: the first has the sensor and the data acquisition setup and the second has all the power supplies needed to power the first casing and the mobile router (see Figure 4.6).

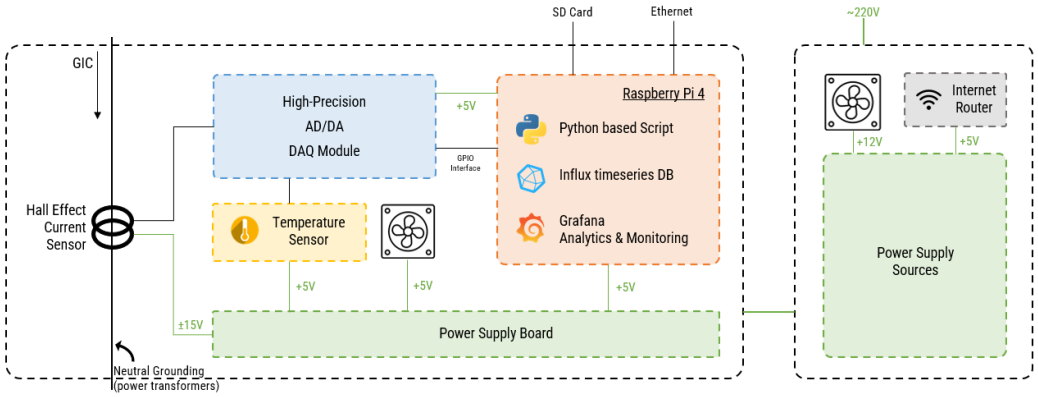

Figure 4.6: System diagram.

Casing 1

This casing has all main components: the Hall effect sensor, the Raspberry Pi with the 24-bit digitizer shield, the temperature sensor and the power supply board along with an active fan (Figure 4.7).

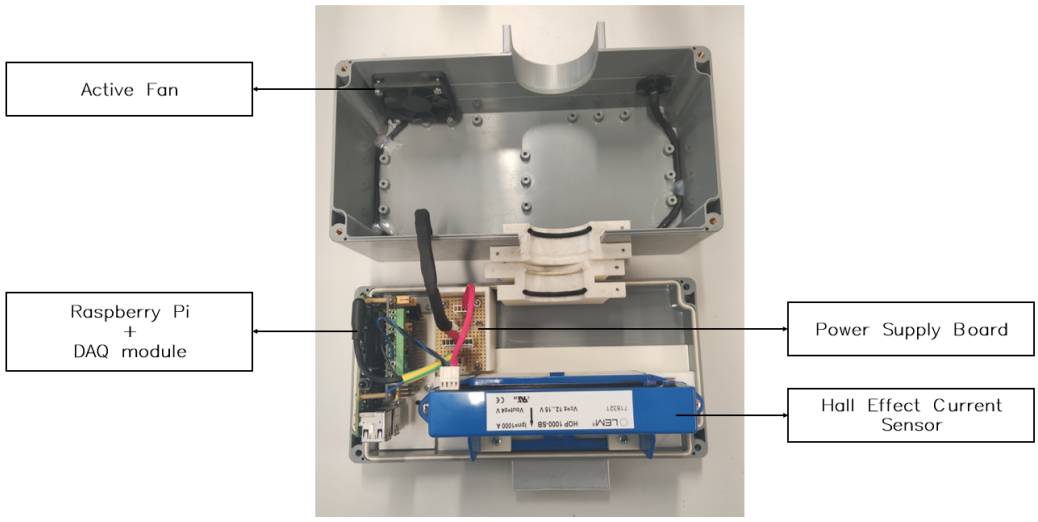

Figure 4.7: Inside view of the system.

Having in mind that the system will embrace the transformer's neutral, some required 3D pieces were printed to improve components stability. In order to immobilize the transformer's cable inside the hole of the Hall effect sensor, two removable pieces were printed with the shape of the cable (see Figure 4.8). Another considered detail taken into account was minimizing the probability of water entering from the upper hole of the casing, therefore further PLA[2] 3D elements were designed and built in order to totally embrace the cable. Finally, more 3D PLA elements were printed to fix the Hall effect sensor, the Raspberry Pi module and the power supply board to the casing. In the end, all wires were connected to the power supply board, except for the signal and ground wires from the Hall effect sensor which were intertwined and connected directly to the Raspberry Pi, in order to cancel external magnetic disturbances.

Figure 4.8: 3D printed pieces to embrace the neutral cable. Black cylinder imitates neutral cable.

Figure 4.9 shows the front and rear views of this casing. In the rear view, there is a ventilation grid, the connection to the system power supply cable as well as the hole to the transformer's cable passing through. In the front view, there is a hole for the same cable to pass through and 3D printed pieces to embrace it.

[2]Polylactic Acid Polymer, one of the most popular materials used in 3D printing.

Figure 4.9: Left) front and Right) rear views of the system. Black cylinder imitates neutral cable.

Casing 2

The second casing has all sources needed to power the system, a second fan for active ventilation and a mobile router for Raspberry Pi communications (Figure 4.10). It is composed by three sources and one DC converter.

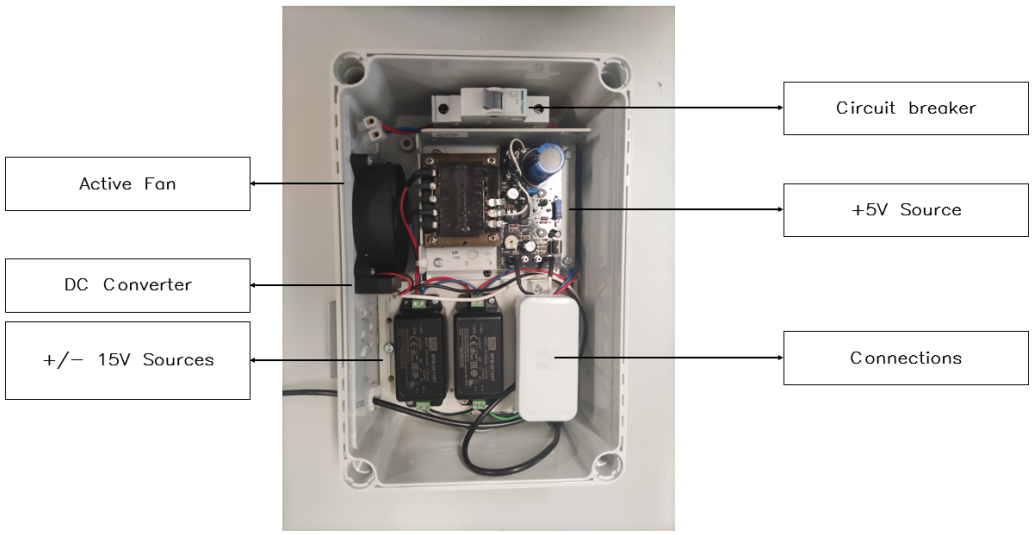

Figure 4.10: Inside view of the power supply casing. The mobile router locates at the casing cover.

1. *Power-one HB5-3/OVP-A*: a DC source with 5V 3.0A output to power the Raspberry Pi, the temperature sensor, the fan for casing 1 (MC32909) and the mobile router.

2. *MPM-30-15ST*: two DC sources with 15V output to power Hall effect sensor ($\pm 15V$) with a output current of 2A.

3. *NMXD0512SO*: a DC converter from 5V to 12V to power the second fan for casing 2 (RDM8025SA).

The two first sources are switched sources. These sources have lower ripple which means less noise and greater stability in the output signal of the system.

Figure 4.11: Outside view of the power supply casing.

4.6 Test performance analysis

4.6.1 Offset behavior

One of the most important parameters of the Hall effect sensor is the offset voltage (V_O in equation 4.2). The offset voltage is the output potential difference in the absence of an external magnetic field. In order to test the behavior and stability of the sensor offset, a signal was acquired without currents flowing through the sensor. Figure 4.12 represents the voltage offset measured by the system at constant temperature equal to 22.5°C. Its average value is -1.4648mV and has a standard deviation of 0.2392mV.

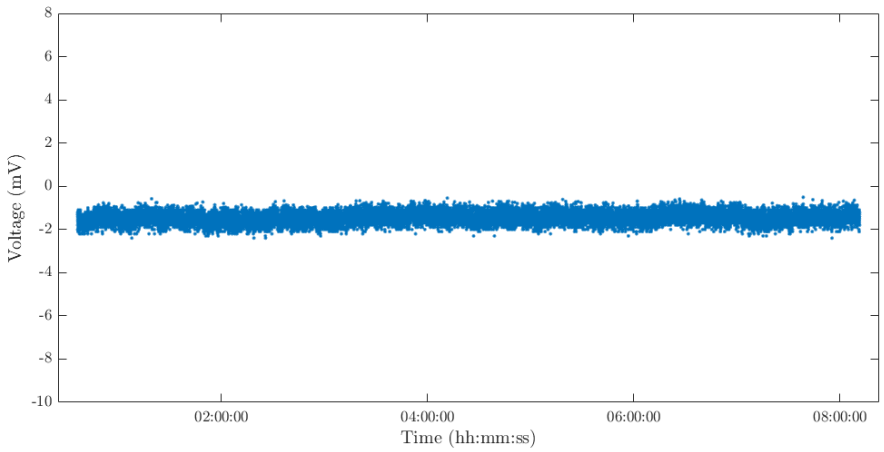

Figure 4.12: Offset level.

4.6.2 Calibrated nominal current tests

In order to calibrate the system, a testing setup was mounted in the laboratory (Figure 4.13). Controlled current between 0 A and 20 A passed in a cable through the sensor. As it was said in section 2 , it is not excepted that the sensor will experiment currents above 10 A. The system response over time is plotted in Figure 4.14.

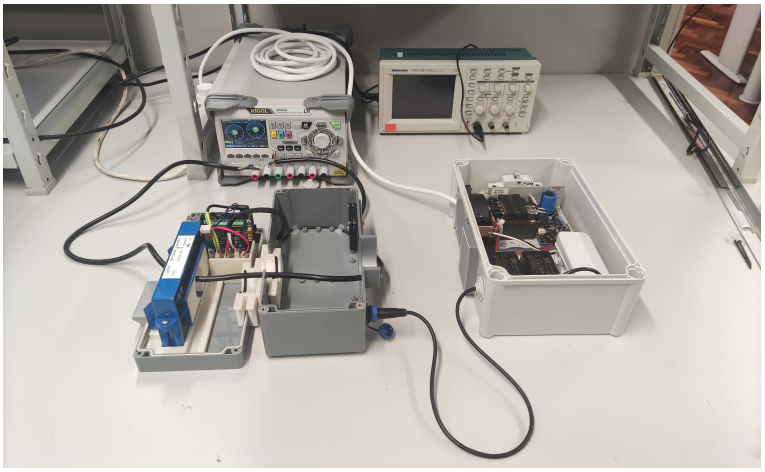

Figure 4.13: Setup for system calibration in laboratory.

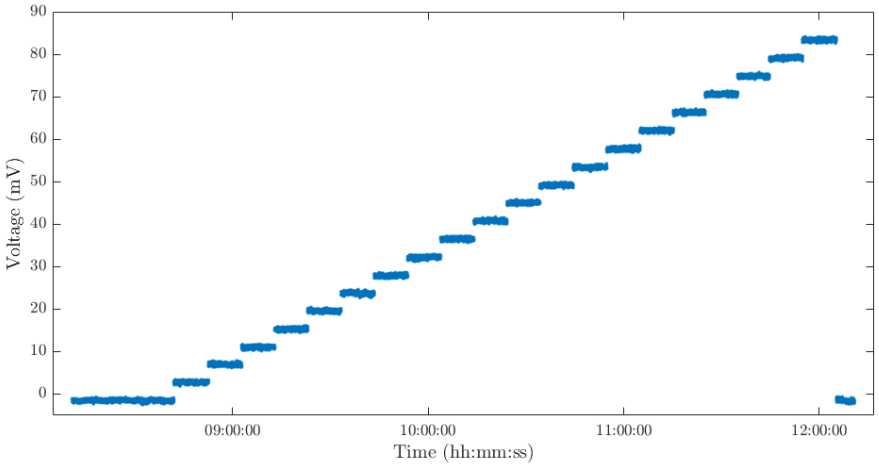

Figure 4.14: Output voltage in the presence of current passing through the sensor.

Figure 4.15 shows the relation between the output voltage and the test current that was flowing through the system.

It also shows the fitting function that corresponds to the calibration line:

$$y = 4.247x - 1.648 \tag{4.6}$$

where x is the value of the current in A and y is the value of the voltage in mV.

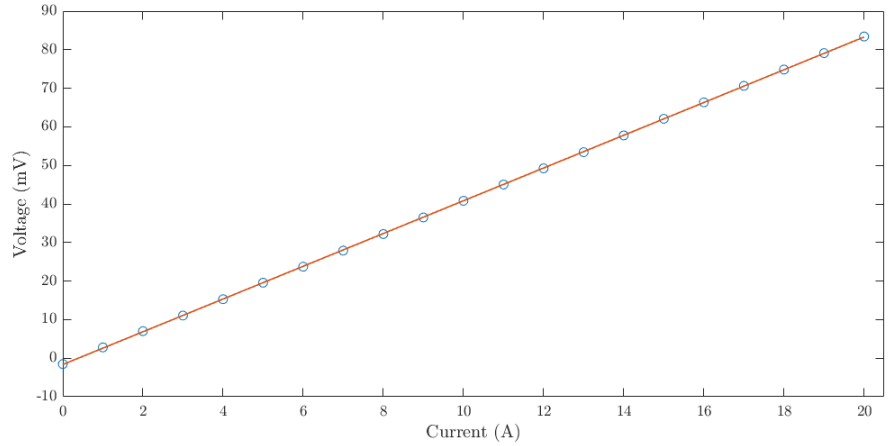

Figure 4.15: Calibration line graphic at room temperature (23ºC).

The value of R-square for this fitting is 1.00 which means a very good linearity approximation. The value of 4.247mV/A is the calibration coefficient and the value -1.648 mV is the ordinate at the origin that corresponds to the sensor offset voltage, V_O, at temperature 23ºC. Note that this offset value, taken from the linear regression to the data, is relatively close to the value -1.4648mV, that was measured in section 4.6.1 for a fixed temperature of 22.5ºC. The offset estimated in this section takes into account a wider range of measuring conditions (currents and temperatures), and because of that it was the value chosen for the offset correction. Checking the sensor datasheet, this value is less than the maximum offset value guaranteed by the manufacturer ($\pm 40mV$) (see Table 4.2). As to the experimental calibration coefficient 4.247 mV/A, this is a more precise value for the sensitivity than given previously (section 4.3.1) based simply on the sensor manufacturer specifications.

4.6.3 Temperature influence

Another relevant factor in Hall effect sensors is the temperature (Cholakova et al., 2012). The calibration coefficient and the output offset voltage are temperature dependent and it is important to understand if the system casing is sufficient to prevent high temperature variations and what effect do they have on sensor performance.

A test setup was designed to test the dependence of the measurement system on ambient temperature variations. The system was thermally stressed and then allowed to cool to room temperature. The temperature was measured by the temperature sensor (Figure 4.16).

Additionally, the Hall effect sensor offset as a function of the temperature was plotted (Figure 4.17). The fitting linear function is also represented and is given by the equation 4.7:

$$y = 0.144x - 5.157 \tag{4.7}$$

where x is the temperature value in °C and y is the sensor offset voltage value in mV. Note that at room temperature, a value is retrieved which is in agreement with equation 4.6. The value of R-square for this fitting is 0.65 which means a

low linearity approximation. This is a low value because the temperature reading by the temperature sensor is not the temperature sensed by the Hall effect sensor derived from dense and protective sensor encapsulation. The value of 0.144mV/°C is the temperature variation rate for V_O. According to the sensor datasheet, the manufacturer guarantees a maximum of ±25mV in temperature variation at the offset value. Since the ambient operating temperature range of the sensor is between -10°C and 70°C, the maximum value of temperature variation of the offset, according to the laboratory tests, is 10.08mV (0.144mV/°C × 70°C), about one half the manufacturer specifications.

No hysteresis was observed and since only ambient variations will be considered (far less demanding than the apparatus hereby described) it was decided to ignore the cooling gradient sign. Note that the dependence of the calibration coefficient on the temperature was not obtained.

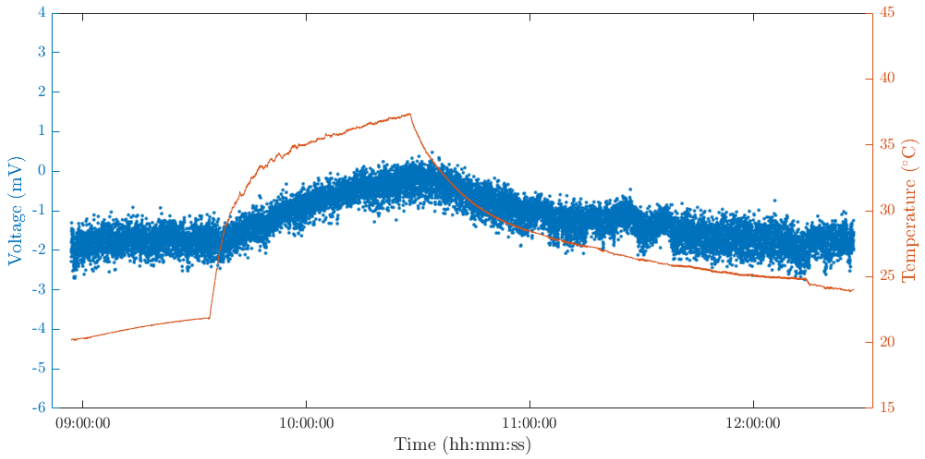

Figure 4.16: Offset behavior in the presence of temperature variations.

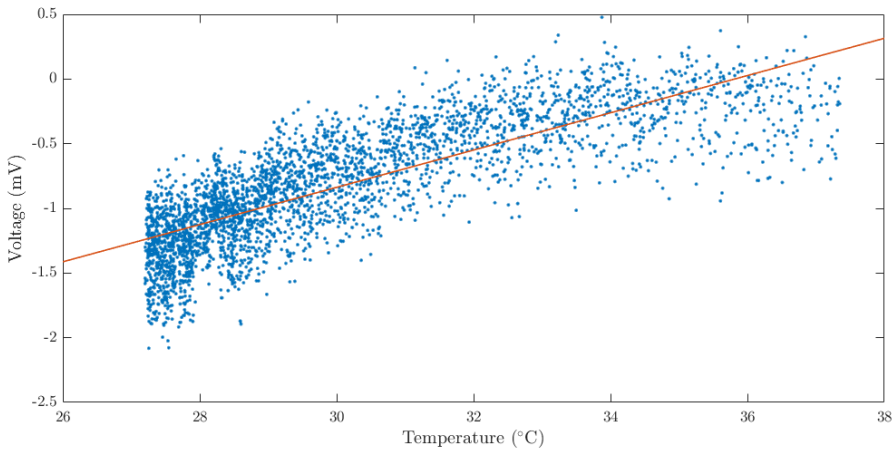

Figure 4.17: Voltage dependence varying temperature.

4.7 Final comments

4.7.1 The sensor performance parameters

A GIC measurement system was proposed in this chapter fitted in 2 casings. The first casing has the sensor and the data acquisition setup and the second has all the power supplies needed to power the first casing and the mobile internet router. All component integration was designed to minimize installation time and effort at the substation.

With this system, it will be possible to measure currents flowing through the cable neutral of the transformer. The Hall effect sensor of the system has a sensitivity of 4 mV/A, which was more precisely determined to be 4.247 mV/A.

The output data sorting from this system is the measured current calculated from equation 4.8:

$$Current(A) = \frac{Voltage(mV) + 1.648}{4.247} \tag{4.8}$$

The offset behavior of the system was characterized with a standard deviation of 0.2392mV, which once converted to current, is equal to 0.056A. This value represents the precision of the system in a laboratory environment.

In this first prototype, the temperature correction will not be done a priory and so it will be something to take into account after having data in the field to better discuss this question.

Future work will be to decrease the dynamic range and consequently improve the system's sensitivity. In addition, data transfer must be autonomous via email or by continuously uploading acquired data to a remote database server.

4.7.2 Possible improvement of the Hall effect sensor

As it was said before, the main reason for choosing the Open Loop Current Transducer HOP 1000-SB from LEM was its 40 mm height of the rectangular hole, essential for the transformer's neutral cable to fit. Because of this, the dynamic range is much larger than necessary. In fact, sensors with smaller dynamic range almost always have small hole dimensions.

So what if a Hall sensor with smaller dynamic range and chosen dimensions for the hole was built?

In fact, it is possible to build a Hall effect sensor by choosing its dimensions and the Hall sensing element. Dewi et al. (2016) developed a DC current sensor by using the Hall effect. The SS49E (Honeywell) magnetoresistive sensor was employed to sense the magnetic field from the field concentrator (see Figure 4.18).

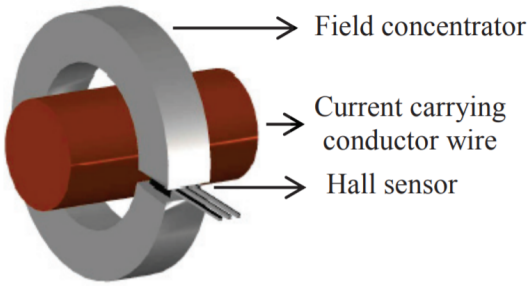

Figure 4.18: Design of current measurement using Hall effect sensor.

Gillet and Friedrich (2019) detail some factors that influence the efficiency of a concentrator of the current sensing system such as the core material and dimensions, the air gap and the core geometry.

In an attempt to put this idea into practice, an experiment was carried out with the sensor used for measuring GICs, the LEM HOP 1000 SB Hall sensor. Looking at its datasheet, the two Hall elements are positioned on top of the sensor, meaning that the bottom must be just a core of ferromagnetic material. So, this one can be replaced by other ferromagnetic material with other dimensions. Clearly, the sensor calibration is lost due to the change of the dimensions and probably the ferromagnetic material too. Three ferrite bars (Ferroxcube, 2008) were used to close the magnetic field path and then 3D pieces were printed to encapsulate them (see Figure 4.19).

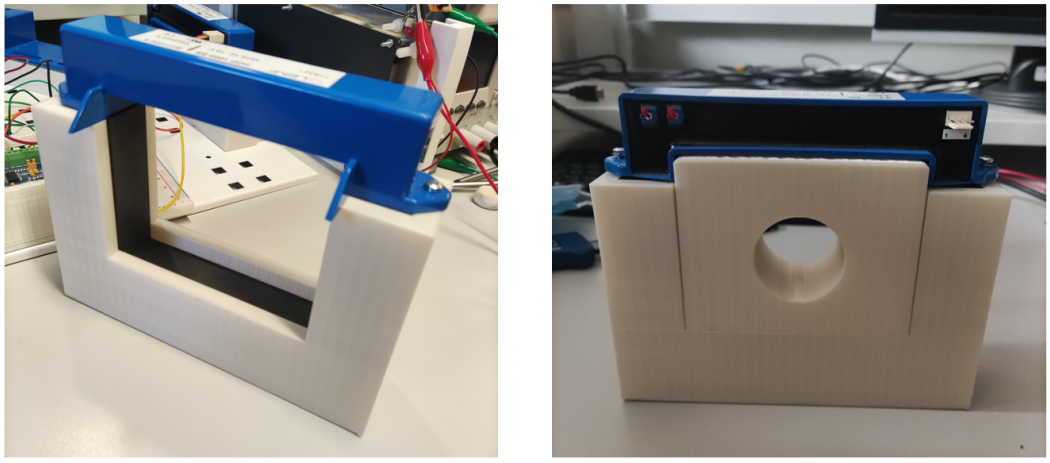

Figure 4.19: Photograph of the built Hall effect sensor. Three ferrite bars were used to close the bottom part of the field concentrator in order to increase hole space.

Current was made to flow in a conductor through with this new field concentrator and its calibration was plotted in Figure 4.20 along with the calibration of the original sensor.

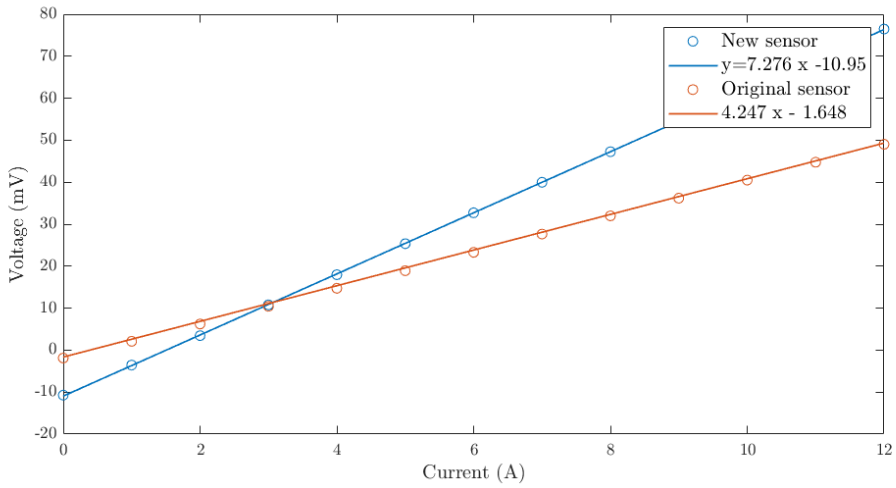

Figure 4.20: Calibration lines of both sensors.

Comparing both slopes, the built sensor has almost twice the sensitivity of the original sensor. This is an interesting result since the original sensor has the dynamic range too high, which decreases sensitivity. However, this is no longer a calibrated sensor and usage should always be preceded by a proper calibration procedure.

To conclude, for the future, the difficulty of finding a Hall sensor with a sufficiently large hole and with a smaller dynamic range, in the order of tens of amps, can be overcome by building a Hall sensor from scratch.

Chapter 5

Installation of the GIC measuring instrument

Contents

5.1 Pilot Installation at the Paraimo Substation (SPI)

In section 2.5, the rationale leading to the choice of the Paraimo substation to install the pilot system of the sensor prototype, was explained.

The Paraimo Substation is located in the Coast/Center part of Portugal (see Figure 5.1) . It is connected to more than one 400kV transmission lines, represented by red lines, and also 220kV and 60kV transmission lines represented by blue and green lines, respectively.

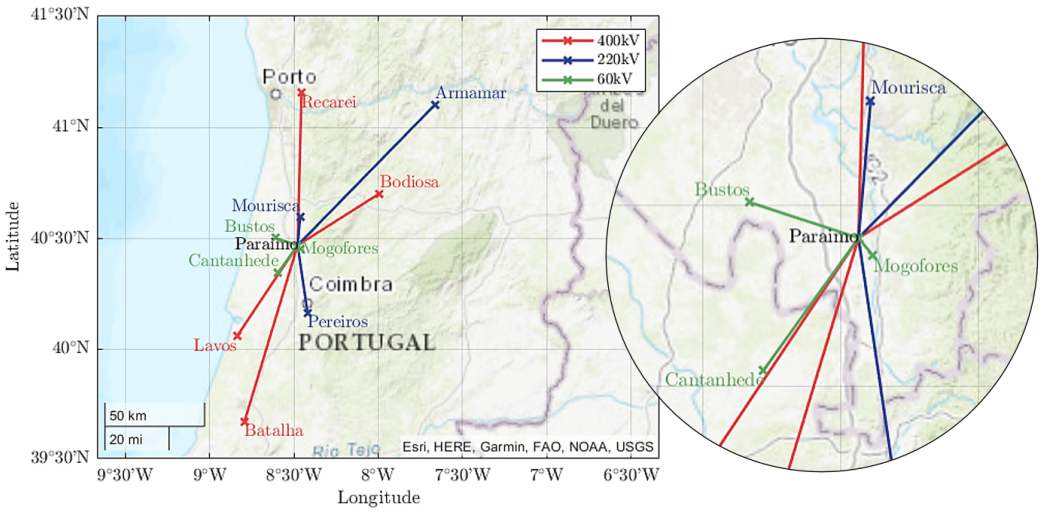

Figure 5.1: Location of Paraimo Substation and the substations connected to it.

Paraimo Substation has two 400kV–60kV power transformers (TRF4 and TRF6) and one 400kV–220kV autotransformer (AT3). Although all three are in the same substation, they have different characteristics (mainly winding resistance values) so, more simulations were carried out to understand which transformer is more susceptible to GICs (Alves Ribeiro et al., personal communication). The decision was to install the system on the TRF6 transformer neutral cable.

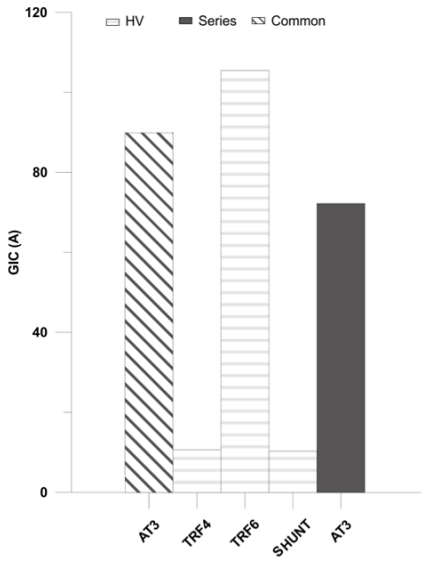

Figure 5.2: Simulation of GICs in Paraimo substation transformers under a severe geomagnetic storm (1V/km). AT3 is the autotransformer represented by both common and series neutrals, TRF4 and TRF6 are the transformers represented by their high voltage neutrals and the shunt resistor, connecting the LV bus to the ground. Credits due to J. Alves Ribeiro.

The system was installed at the TRF6 power transformer which is a 400kV to 60kV transformer (see Figure 5.3). TRF6 has two different neutral cables, one refers to the 400kV and the other one refers to the 60kV. The system was installed in the first one because resistances are lower along the transmission lines at this voltage level which means higher GICs are expected.

The installation and fixing of both casings were carried out with the support of the local REN team. The power supply casing (Casing 2) was simply fixed to the nearby support pole using mounting profiles. On the other hand, the sensor casing (Casing 1) had a more complex installation process. Both Hall effect sensor and 3D printed pieces were disassembled to enclose the neutral cable and adjust it conveniently. In the end, the neutral cable was tight to the system. Figure 5.4 shows both casings installed and Figure 5.5 shows more details.

After assembling all components of the system, the data acquisition was initialized via remote connection and remote access to the signal was successfully obtained via the mobile router.

Figure 5.3: TRF6 power transformer. On the left, collaborators from REN working on the neutral cable of the transformer where the GIC measurement system was installed.

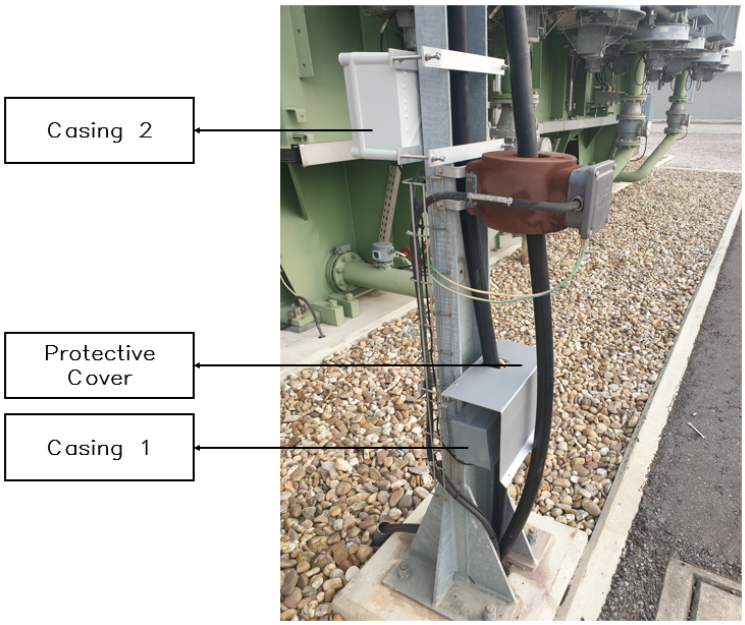

Figure 5.4: Casing 2 installed above and casing 1 installed below with a protection from direct rain and Sun radiation.

Figure 5.5: Details of both casings in the field (top photos: Casing 1; bottom; Casing 2).

5.2 First measurements on the transformer's neutral

The access to the measured signal is made remotely (see section 4.4) as well as save data in a spreadsheet file and export it.

In Figure 5.6 is represented the measured data between September 4^{th} and 7^{th} and in Figure 5.7 is represented the measured data on September 9^{th}. The blue line is the measured current and the orange line is the measured temperature.

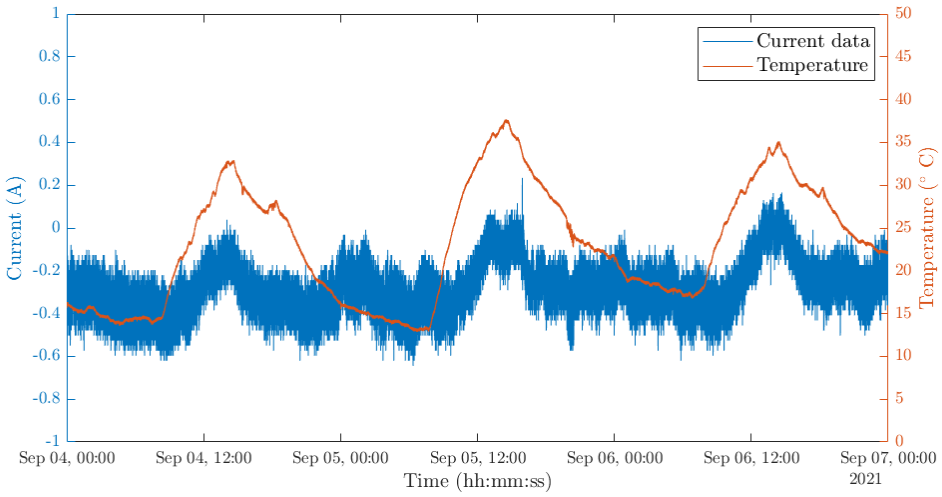

Figure 5.6: Current and temperature measured data during the first days after installing the GIC measurement system.

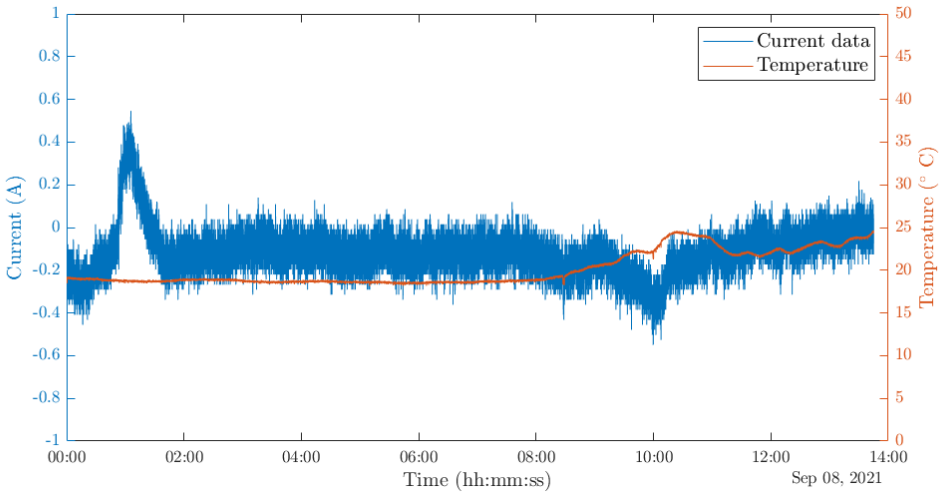

Figure 5.7: Current and temperature measured data, with two distinct peaks, on September 9^{th}.

The sensor signal recorded and shown in Figure 5.7 between 02:00am and 08:00am, presents an average offset of -0.1123A and a standard deviation equal to 0.0601A.

5.3 Preliminary interpretation

From Figure 5.6, it can be seen that the current signal shows a temperature dependency. This dependency can be explained either by a temperature dependency of the electronic system or by the daily quiet variation of the geomagnetic field, i. e., smooth cyclic variation of the geomagnetic field in the absence of larger geomagnetic disturbances.

It is also clear that there is a deviation from the horizontal zero line, although this current data has already an offset correction. This suggests that the system has a different offset in the field, compared to laboratory conditions. As to the sensor precision in the field, it is very close to that observed in the laboratory.

From Figure 5.7, the temperature variation is very small. Nonetheless, two current peaks appear (one positive and the other negative), which could be due to GIC events. There is a peak of about 0.6A above baseline at 1:00 am and other one of about 0.2A below baseline at 10:00am. Therefore, the following steps were to understand if the system was measuring GICs or not.

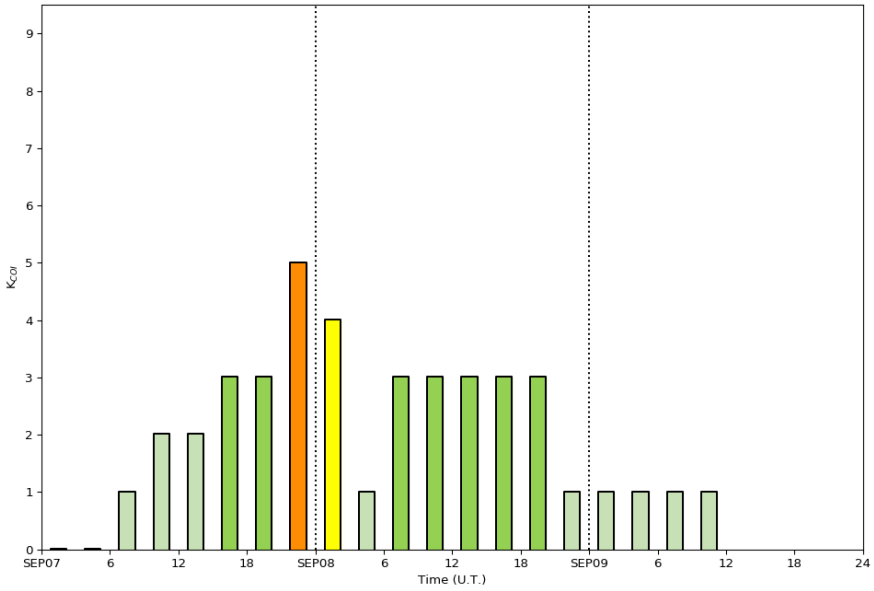

Figure 5.8: K index at COI between September 7^{th} and 9^{th} where higher values were registered at the beginning of September 8^{th}. From the OGAUC server: https://spinlab.ogauc.pt.

Figure 5.8 shows the K index at COI between September 7^{th} and 9^{th}. To clarify, K index is a proxy used to characterize the magnitude of geomagnetic storms. From this Figure, it is clear that there was a geomagnetic disturbance in the geomagnetic field, at the beginning of September 8^{th}, which could have led to the induction of electric field B in the Earth and consequently there could be currents flowing in the transformer neutral.

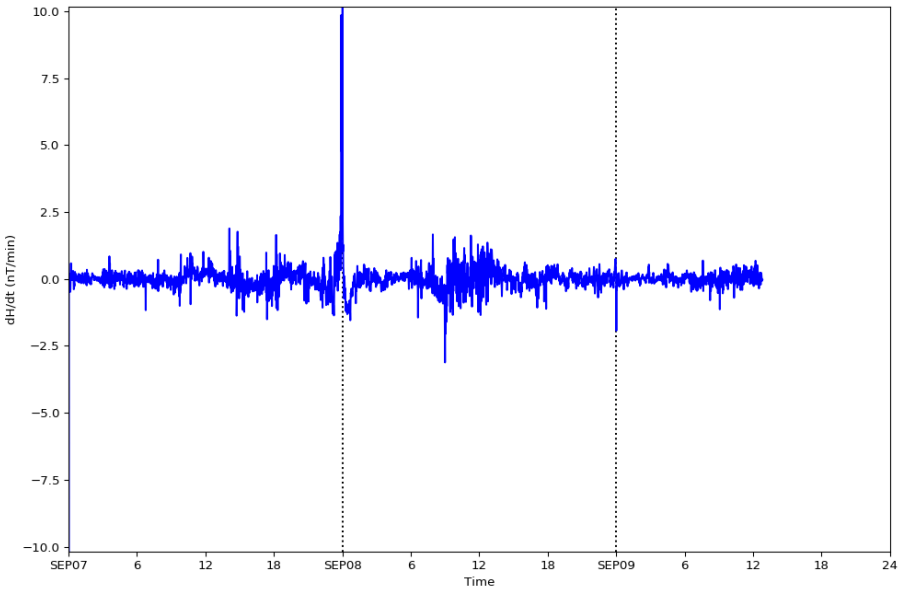

Figure 5.9: Rate of variation of the geomagnetic field, dB/dt, computed from the magnetic field B measured by the magnetometer at COI (see chapter 2.1.2). From the OGAUC server: https://spinlab.ogauc.pt.

The rate of variation of the geomagnetic field measured by the magnetometer at COI shows the effect of the geomagnetic storm in Portugal mainland, through the signal dB/dt which is more directly related with possible induced GICs. Figure 5.9 shows a rapid magnetic field time variation at the beginning of September 8^{th} as well as a less pronounced but with larger duration disturbance at midday of the same day.

Furthermore, other countries, like Finland, have also measured disturbances in the GIC measurement systems they have installed (see eurisgic.org).

Chapter 6

Conclusion

The effect of shield wires on computed GICs can be studied using an elementary circuit model for power lines with shield wires. An equivalent circuit model with both shield wire resistances and emfs induced along the shield wire lines was proposed in this thesis. This approach is new compared with other studies of this problem, that neglect the contribution of the emfs on the shield wires.

The national transmission system operator (REN) provided relevant information from two Portuguese power transmission lines in order to be used as case studies. The conclusion of this first part of the study was that the equivalent circuit model presented in this thesis has a higher accuracy than both the equivalent circuit model previously proposed for transmission grids with shield wires, and the circuit model without shield wires, for shorter lines (usual in Portuguese network). To be able to evaluate these accuracies, there was also the need to solve the complete circuit equations, which was done both solving numerically the circuit matrix equations and also using LTSpice free simulation software. Errors go down from 6.32% (without shield wires) and 10.92% (the equivalent circuit model without induced emfs) to 0.428%. Beyond this, scattered values can influence the current in the substations but may not influence the value of GICs. Lastly, when increasing the complexity of the circuit model by adding more power transmission lines to a substation node, the value of GICs increases. If the equivalent circuit model with only shield wire resistances is used, the error increases when adding more power transmission lines to a node. On the other hand, the equivalent circuit with both shield wire resistance and emfs presents a very high accuracy.

GIC estimated values may not be accurate because there are many parameters and models involved in GIC calculations. So, a prototype GICs measuring system was designed, assembled and installed in a Portuguese substation in order to get observational constraints for estimated GICs values in the national power network. This system consists of a Hall effect sensor with a sensitivity of 4.247mV/A, a Raspberry Pi 4 Model B platform with a high resolution digitizer (24 bit resolution) expansion board (Waveshare AD/DA) for data recording. This data is stored in a local database and data can be downloaded through a remote connection. Laboratory tests shows an offset deviation of -0.388A with standard deviation of 0.056A.

The system was successfully installed at Paraimo substation from REN and it is currently fully operational. This system will be the workbench for future developments and tests envisaging a multi-system GICs monitoring network in Portuguese

power substations. First measurements shows an offset deviation of -0.112A with standard deviation of 0.060A, i. e., measurements with slightly greater accuracy and similar precision. Nevertheless, this preliminary data revealed not only the expected diurnal modulation (temperature dependent), but also some current oscillations, that are strong candidates to GIC events.

6.1 Future work

The work in this thesis has the potential to be continued and improved in several points:

1. *Influence of each input parameter on the proposed equivalent circuit*

   Perform sensitivity tests with different power grid parameters (R_L, R_G, R_W, R_T, R_S) and different geomagnetic storm intensities (V_L, V_i) in the equivalent circuit model where both shield wire resistances and emfs are taken into account.

2. *Second generation of the GIC measuring system*

   Development of a Hall effect based sensor optimized for recording GICs (optimized sensitivity to the expected range of GICs) and with the mechanical contingencies involved. In this new generation, the system will be design to daily send data via email or to continuously upload acquired data to a remote database server. It will also be interesting to include an RTC (Real time clock) and/or a GPS module for time synchronization when more systems are installed.

3. *Effect of GICs on Power Transformers*

   Integrate a more in-depth study of the effect of GICs on power transformers to mitigate their impact before rising to a certain threatening level.

4. *Portuguese natural gas pipeline network*

   GICs flow not only in power networks but also in gas pipelines because they are grounded conductors too. One step further will be to study the feasibility of extending this kind of study to GICs modeling and measuring in the Portuguese natural gas pipeline network.

Appendix A

Complete Circuit Matrix

$\theta_i = \sum_{j=i}^{n-1} R_{Wj}$
$\alpha = R_L + R_{TA} + R_{TB} + \sum_{j=1}^{n} R_{Wj}$
$\beta = R_{Wn} + R_{SB} + R_{G(n-1)}$
$\gamma = R_{W(n-1)} + R_{G(n-1)} + R_{G(n-2)}$

$$\begin{bmatrix} 0 \\ V_1 \\ V_2 \\ \cdot \\ \cdot \\ V_i \\ \cdot \\ \cdot \\ V_{n-1} \\ V_n \end{bmatrix} = \begin{bmatrix} \theta_1 & R_{Wn} & -\alpha & \theta_2 & \theta_3 & \cdot & \theta_{(j+1)} & \cdot & \cdot & \theta_{(n-2)} \\ R_{W1} + R_{SA} & 0 & -R_{W1} & -R_{G1} & 0 & \cdot & \cdot & \cdot & \cdot & 0 \\ R_{W2} & 0 & -R_{W2} & -R_{W2} + R_{G1} & -R_{G2} & 0 & \cdot & \cdot & \cdot & 0 \\ \cdot & & & & & & & & & \\ \cdot & & & & & & & & & \\ R_{Wi} & 0 & -R_{Wi} & -R_{Wi} & \cdot & R_{Wi} & R_{Wi} + R_{Gi} & -R_{G(i+1)} & 0 & 0 \\ \cdot & & & & & & & & & \\ \cdot & & & & & & & & & \\ R_{W(n-1)} + R_{G(n-1)} & -R_{G(n-1)} & -R_{W(n-1)} & R_{W(n-1)} + R_{G(n-1)} & \cdot & \cdot & \cdot & \cdot & R_{W(n-1)} + R_{Gn} & \gamma \\ -R_{G(n-1)} & \beta & -R_{Wn} & -R_{G(n-1)} & \cdot & \cdot & \cdot & \cdot & \cdot & -R_{G(n-1)} \end{bmatrix} \begin{bmatrix} I_{SA} \\ I_{SB} \\ I_L \\ I_1 \\ \cdot \\ \cdot \\ I_j \\ \cdot \\ \cdot \\ I_{n-2} \end{bmatrix}$$

Appendix B

Portuguese Grid Maps

B.1 Portuguese High Level Transmission Power Grid

Figure B.1: Map of the Portuguese High Level Transmission Power Grid.

B.2 Portuguese Pipeline Grid

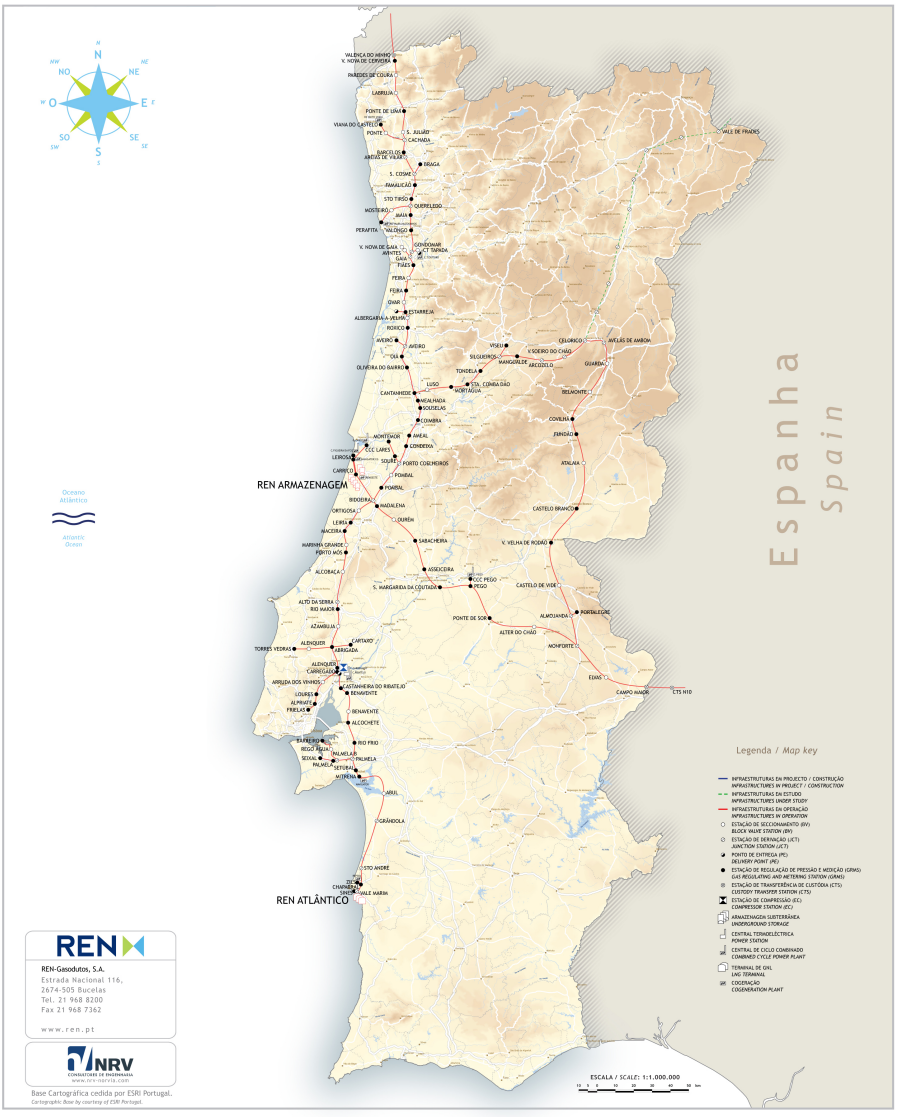

Figure B.2: Map of the Portuguese Pipeline Grid

References

Z. M. K. Abda, N. F. A. Aziz, M. Z. A. A. Kadir, and Z. A. Rhazali. A review of geomagnetically induced current effects on electrical power system: Principles and theory. *IEEE Access*, 8:200237–200258, 2020. doi: 10.1109/ACCESS.2020.3034347.

V. Albertson, J. Kappenman, N. Mohan, and G. Skarbakka. Load-flow studies in the presence of geomagnetically-induced currents. 1979. Copyright: Copyright 2020 Elsevier B.V., All rights reserved.; IEEE Power Eng Soc, Prepr, Summer Meet ; Conference date: 15-07-1979 Through 20-07-1979.

J. Alves Ribeiro, F. J. G. Pinheiro, P. B. Soares, F. A. M. Santos, and M. A. Pais. Towards more accurate GIC estimations in the Portuguese power network. Communication at: IAGA-IASPEI 2021; 21-27 August 2021; Hyderabad, India.

J. Alves Ribeiro, F. J. G. Pinheiro, and M. A. Pais. First estimations of geomagnetically induced currents in the south of portugal. *Space Weather*, 19(1):e2020SW002546, 2021. doi: https://doi.org/10.1029/2020SW002546. URL https://agupubs.onlinelibrary.wiley.com/doi/abs/10.1029/2020SW002546. e2020SW002546 10.1029/2020SW002546.

E. Astafyeva, I. Zakharenkova, and M. Förster. Ionospheric response to the 2015 st. patrick's day storm: A global multi-instrumental overview. *Journal of Geophysical Research: Space Physics*, 120(10):9023–9037, 2015. doi: https://doi.org/10.1002/2015JA021629. URL https://agupubs.onlinelibrary.wiley.com/doi/abs/10.1002/2015JA021629.

R. L. Bailey, T. S. Halbedl, I. Schattauer, G. Achleitner, and R. Leonhardt. Validating gic models with measurements in austria: Evaluation of accuracy and sensitivity to input parameters. *Space Weather*, 16(7):887–902, 2018. doi: https://doi.org/10.1029/2018SW001842. URL https://agupubs.onlinelibrary.wiley.com/doi/abs/10.1029/2018SW001842.

Barbosa, Cleiton, Alves, Livia, Caraballo, Ramon, Hartmann, Gelvam A., Papa, Andres R.R., and Pirjola, Risto J. Analysis of geomagnetically induced currents at a low-latitude region over the solar cycles 23 and 24: comparison between measurements and calculations. *J. Space Weather Space Clim.*, 5:A35, 2015. doi: 10.1051/swsc/2015036. URL https://doi.org/10.1051/swsc/2015036.

E. Bernhardi, P. Cilliers, and C. Gaunt. Improvement in the modelling of geomagnetically induced currents in southern Africa. *South African Journal of Science*, 104: 265 – 272, 08 2008a. ISSN 0038-2353. URL http://www.scielo.org.za/scielo.php?script=sci_arttext&pid=S0038-23532008000400010&nrm=iso.

E. Bernhardi, T. Tjimbandi, P. Cilliers, and C. Gaunt. Improved calculation of geomagnetically induced currents in power networks in low-latitude regions. 01 2008b.

S. Blake. *Modelling and Monitoring Geomagnetically Induced Currents in Ireland*. PhD thesis, 2017.

S. P. Blake, P. T. Gallagher, J. McCauley, A. G. Jones, C. Hogg, J. Campanyà, C. D. Beggan, A. W. P. Thomson, G. S. Kelly, and D. Bell. Geomagnetically induced currents in the irish power network during geomagnetic storms. *Space Weather*, 14 (12):1136–1154, 2016. doi: https://doi.org/10.1002/2016SW001534. URL https://agupubs.onlinelibrary.wiley.com/doi/abs/10.1002/2016SW001534.

L. Bolduc. GIC observations and studies in the Hydro-Québec power system. *Journal of Atmospheric and Solar-Terrestrial Physics*, 64(16):1793–1802, Nov. 2002. doi: 10.1016/S1364-6826(02)00128-1.

L. Bolduc and J. Aubin. Effects of direct currents in power transformers part i. a general theoretical approach. *Electric Power Systems Research*, 1(4):291–298, 1978. ISSN 0378-7796. doi: https://doi.org/10.1016/0378-7796(78)90015-9. URL https://www.sciencedirect.com/science/article/pii/0378779678900159.

D. Boteler. The effects of geomagnetic disturbances on electrical systems at the earth's surface. *Advances in Space Research*, 22(1):17 – 27, 1998. ISSN 0273-1177. doi: https://doi.org/10.1016/S0273-1177(97)01096-X. URL http://www.sciencedirect.com/science/article/pii/S027311779701096X. Solar-Terrestrial Relations: Predicting the Effects on the Near-Earth Environment.

D. H. Boteler. Modeling geomagnetic interference on railway signaling track circuits. *Space Weather*, 19(1):e2020SW002609, 2020. doi: https://doi.org/10.1029/2020SW002609. URL https://agupubs.onlinelibrary.wiley.com/doi/abs/10.1029/2020SW002609. e2020SW002609 2020SW002609.

D. H. Boteler and R. J. Pirjola. Modeling geomagnetically induced currents. *Space Weather*, 15(1):258–276, 2017. doi: https://doi.org/10.1002/2016SW001499. URL https://agupubs.onlinelibrary.wiley.com/doi/abs/10.1002/2016SW001499.

D. Boteler Pirjola and R. Pirjola. Comparison of methods for modelling geomagnetically induced currents. *Annales Geophysicae*, 32:1177–1187, 09 2014. doi: 10.5194/angeo-32-1177-2014.

Boteler, David. Methodology for simulation of geomagnetically induced currents in power systems. *J. Space Weather Space Clim.*, 4:A21, 2014. doi: 10.1051/swsc/2014018. URL https://doi.org/10.1051/swsc/2014018.

J. Cardoso, M. Silva, F. Pinheiro, and M. A. Pais. Standalone gics data logger for substation transformers with open-loop hall-effect sensors. poster presented at: 16th european space weather week; 18-22 november 2019; liège, belgium. 2019.

F. A. Chaves. Record of the great magnetic storm of october 31, 1903, at ponta delgada, azores. *Terrestrial Magnetism and Atmospheric Electricity*, 9(1):29–33,

1904. doi: https://doi.org/10.1029/TE009i001p00029-02. URL https://agupubs.onlinelibrary.wiley.com/doi/abs/10.1029/TE009i001p00029-02.

K.-C. Choi, M.-Y. Park, Y. Ryu, Y. Hong, J.-H. Yi, S.-W. Park, and J.-H. Kim. Installation of induced current measurement systems in substations and analysis of gic data during geomagnetic storms. *Journal of Astronomy and Space Sciences*, 32:427–434, 12 2015. doi: 10.5140/JASS.2015.32.4.427.

I. N. Cholakova, T. B. Takov, R. T. Tsankov, and N. Simonne. Temperature influence on hall effect sensors characteristics. In *2012 20th Telecommunications Forum (TELFOR)*, pages 967–970, 2012. doi: 10.1109/TELFOR.2012.6419370.

S. D. T. Dewi, C. Panatarani, and I. M. Joni. Design and development of dc high current sensor using hall-effect method. *AIP Conference Proceedings*, 1712(1): 030006, 2016. doi: 10.1063/1.4941871. URL https://aip.scitation.org/doi/abs/10.1063/1.4941871.

Ferroxcube. http://ferroxcube.home.pl/prod/assets/i1002525.pdf, 2008.

C. Gaunt and G. Coetzee. Transformer failures in regions incorrectly considered to have low gic-risk. *2007 IEEE Lausanne Power Tech*, pages 807–812, 2007.

C. Gillet and A. Friedrich. Guidelines for Designing a Concentrator for High-Current Sensing Applications with an Allegro Hall-Effect Sensor IC. https://www.allegromicro.com/en/insights-and-innovations/technical-documents/hall-effect-sensor-ic-publications/current-sensor-concentrator, 2019.

R. Girgis, K. Vedante, and K. Gramm. Effects of geomagnetically induced currents on power transformers and power systems. *44th International Conference on Large High Voltage Electric Systems 2012*, 01 2012.

T. Halbedl. *Low frequency neutral point currents on transformer in the Austrian power transmission network*. PhD thesis, 2019.

D. H. Hathaway. The solar cycle. *Living Reviews in Solar Physics*, 12(1), Sep 2015. ISSN 1614-4961. doi: 10.1007/lrsp-2015-4. URL http://dx.doi.org/10.1007/lrsp-2015-4.

H. Hayakawa, P. Ribeiro, J. M. Vaquero, M. C. Gallego, D. J. Knipp, F. Mekhaldi, A. Bhaskar, D. M. Oliveira, Y. Notsu, V. M. S. Carrasco, and et al. The extreme space weather event in 1903 october/november: An outburst from the quiet sun. *The Astrophysical Journal*, 897(1):L10, Jun 2020. ISSN 2041-8213. doi: 10.3847/2041-8213/ab6a18. URL http://dx.doi.org/10.3847/2041-8213/ab6a18.

J. Hübert, C. D. Beggan, G. S. Richardson, T. Martyn, and A. W. P. Thomson. Differential magnetometer measurements of geomagnetically induced currents in a complex high voltage network. *Space Weather*, 18(4):e2019SW002421, 2020. doi: https://doi.org/10.1029/2019SW002421. URL https://agupubs.onlinelibrary.wiley.com/doi/abs/10.1029/2019SW002421. e2019SW002421 10.1029/2019SW002421.

J. Koen and T. Gaunt. Geomagnetically induced currents in the southern african electricity transmission network. In *2003 IEEE Bologna Power Tech Conference Proceedings,*, volume 1, pages 7 pp. Vol.1–, 2003. doi: 10.1109/PTC.2003.1304165.

M. Lehtinen and R. Pirjola. Currents produced in earthed conductor networks by geomagnetically-induced electric fields. *Annales Geophysicae*, 3:479–484, 1985.

LEM Components Brochure. Isolated current and voltage transducers characteristics - applications - calculations. Brochure. URL https://www.lem.com/en/file/3139/download.

C. Liu, D. H. Boteler, and R. J. Pirjola. Influence of shield wires on geomagnetically induced currents in power systems. *International Journal of Electrical Power Energy Systems*, 117:105653, 2020. ISSN 0142-0615. doi: https://doi.org/10.1016/j.ijepes.2019.105653. URL https://www.sciencedirect.com/science/article/pii/S0142061519323312.

C.-M. Liu, L.-G. Liu, and Y. Yang. Monitoring and modeling geomagnetically induced currents in power grids of china. In *2009 Asia-Pacific Power and Energy Engineering Conference*, pages 1–4, 2009. doi: 10.1109/APPEEC.2009.4918502.

D. H. Mac Manus, C. J. Rodger, M. Dalzell, A. W. P. Thomson, M. A. Clilverd, T. Petersen, M. M. Wolf, N. R. Thomson, and T. Divett. Long-term geomagnetically induced current observations in new zealand: Earth return corrections and geomagnetic field driver. *Space Weather*, 15(8):1020–1038, 2017a. doi: https://doi.org/10.1002/2017SW001635. URL https://agupubs.onlinelibrary.wiley.com/doi/abs/10.1002/2017SW001635.

D. H. Mac Manus, C. J. Rodger, M. Dalzell, A. W. P. Thomson, M. A. Clilverd, T. Petersen, M. M. Wolf, N. R. Thomson, and T. Divett. Long-term geomagnetically induced current observations in new zealand: Earth return corrections and geomagnetic field driver. *Space Weather*, 15(8):1020–1038, 2017b. doi: https://doi.org/10.1002/2017SW001635. URL https://agupubs.onlinelibrary.wiley.com/doi/abs/10.1002/2017SW001635.

L. Mari. Magnetizing and exciting currents waveshapes in transformers. https://eepower.com/technical-articles/magnetizing-and-exciting-currents-waveshapes-in-transformers/#, 2020.

J. Marusek. Solar storm threat analysis. 2007.

E. Matandirotya, P. Cilliers, and R. van Zyl. Differential magnetometer method (dmm) for the measurement of geomagnetically induced currents (gic) in a power line: Technical aspects. *Journal of Electrical Engineering Elektrotechnický časopis*, 66:50–53, 09 2015.

A. Meliopoulos, E. Glytsis, G. Cokkinides, and M. Rabinowitz. Comparison of ss-gic and mhd-emp-gic effects on power systems. *IEEE Transactions on Power Delivery*, 9(1):194–207, 1994. doi: 10.1109/61.277691.

S. E. Milan, L. B. N. Clausen, J. C. Coxon, J. A. Carter, M. T. Walach, K. Laundal, N. Østgaard, P. Tenfjord, J. Reistad, K. Snekvik, H. Korth, and B. J. Anderson. Overview of Solar Wind-Magnetosphere-Ionosphere-Atmosphere Coupling and the Generation of Magnetospheric Currents. , 206(1-4):547–573, Mar. 2017. doi: 10.1007/s11214-017-0333-0.

T. S. Molinski. Why utilities respect geomagnetically induced currents. *Journal of Atmospheric and Solar-Terrestrial Physics*, 64(16):1765–1778, 2002. ISSN 1364-6826. doi: https://doi.org/10.1016/S1364-6826(02)00126-8. URL https://www.sciencedirect.com/science/article/pii/S1364682602001268. Space Weather Effects on Technological Systems.

A. Muchinapaya, C. T. Gaunt, and D. T. O. Oyedokun. Design of a low-cost system to monitor geomagnetically induced currents in transformer neutrals. In *2018 IEEE PES/IAS PowerAfrica*, pages 875–879, 2018. doi: 10.1109/PowerAfrica.2018.8520985.

S. Nakamura, Y. Ebihara, S. Fujita, T. Goto, N. Yamada, S. Watari, and Y. Omura. Time domain simulation of geomagnetically induced current (gic) flowing in 500-kv power grid in japan including a three-dimensional ground inhomogeneity. *Space Weather*, 16(12):1946–1959, 2018. doi: https://doi.org/10.1029/2018SW002004. URL https://agupubs.onlinelibrary.wiley.com/doi/abs/10.1029/2018SW002004.

NASA. Aurorae Borealis. https://www.nasa.gov/feature/goddard/2016/nasa-s-themis-sees-auroras-move-to-the-rhythm-of-earth-s-magnetic-field, 2016.

U. S. National Weather Service. Intense space weather storms october 19-november 07, 2003, 2004. URL https://repository.library.noaa.gov/view/noaa/6995. Service Assessment.

N. G. D. C. NOAA. When solar wind collides with Earth's magnetic field. https://www.noaa.gov/, 2019.

E. J. Oughton, M. Hapgood, G. S. Richardson, C. D. Beggan, A. W. P. Thomson, M. Gibbs, C. Burnett, C. T. Gaunt, M. Trichas, R. Dada, and R. B. Horne. A risk assessment framework for the socioeconomic impacts of electricity transmission infrastructure failure due to space weather: An application to the united kingdom. *Risk Analysis*, 39(5):1022–1043, 2019. doi: https://doi.org/10.1111/risa.13229. URL https://onlinelibrary.wiley.com/doi/abs/10.1111/risa.13229.

R. Pirjola. Geomagnetically induced current during magnetic storms. *Plasma Science, IEEE Transactions on*, 28:1867 – 1873, 01 2000. doi: 10.1109/27.902215.

R. Pirjola. Calculation of geomagnetically induced currents (gic) in a high-voltage electric power transmission system and estimation of effects of overhead shield wires on gic modelling. *Journal of Atmospheric and Solar-Terrestrial Physics*, 69(12):1305–1311, 2007. ISSN 1364-6826. doi: https://doi.org/10.1016/j.jastp.2007.04.001. URL https://www.sciencedirect.com/science/article/pii/S1364682607001058.

A. Pulkkinen, A. Viljanen, K. Pajunpää, and R. Pirjola. Recordings and occurrence of geomagnetically induced currents in the finnish natural gas pipeline network. *Journal of Applied Geophysics*, 48(4):219–231, 2001. ISSN 0926-9851. doi: https://doi.org/10.1016/S0926-9851(01)00108-2. URL https://www.sciencedirect.com/science/article/pii/S0926985101001082.

A. Pulkkinen, S. Lindahl, A. Viljanen, and R. Pirjola. Geomagnetic storm of 29–31 october 2003: Geomagnetically induced currents and their relation to problems in the swedish high-voltage power transmission system. *Space Weather*, 3 (8), 2005. doi: https://doi.org/10.1029/2004SW000123. URL https://agupubs.onlinelibrary.wiley.com/doi/abs/10.1029/2004SW000123.

A. Pulkkinen, E. Bernabeu, A. Thomson, A. Viljanen, R. Pirjola, D. Boteler, J. Eichner, P. J. Cilliers, D. Welling, N. P. Savani, R. S. Weigel, J. J. Love, C. Balch, C. M. Ngwira, G. Crowley, A. Schultz, R. Kataoka, B. Anderson, D. Fugate, J. J. Simpson, and M. MacAlester. Geomagnetically induced currents: Science, engineering, and applications readiness. *Space Weather*, 15(7):828–856, 2017. doi: https://doi.org/10.1002/2016SW001501.

P. Ribeiro, J. M. Vaquero, M. C. Gallego, and R. M. Trigo. The first documented space weather event that perturbed the communication networks in iberia. *Space Weather*, 14(7):464–468, 2016. doi: https://doi.org/10.1002/2016SW001424. URL https://agupubs.onlinelibrary.wiley.com/doi/abs/10.1002/2016SW001424.

C. J. Rodger, M. A. Clilverd, D. H. Mac Manus, I. Martin, M. Dalzell, J. B. Brundell, T. Divett, N. R. Thomson, T. Petersen, Y. Obana, and N. R. Watson. Geomagnetically induced currents and harmonic distortion: Storm-time observations from new zealand. *Space Weather*, 18(3):e2019SW002387, 2020. doi: https://doi.org/10.1029/2019SW002387. URL https://agupubs.onlinelibrary.wiley.com/doi/abs/10.1029/2019SW002387. e2019SW002387 2019SW002387.

R. H. Romer. What do "voltmeters" measure?: Faraday's law in a multiply connected region. *American Journal of Physics*, 50(12):1089–1093, 1982. doi: 10.1119/1.12923.

P. Rothwell and C. E. McIlwain. Magnetic storms and the van allen radiation belts—observations from satellite 1958 (explorer iv). *Journal of Geophysical Research (1896-1977)*, 65(3):799–806, 1960. doi: https://doi.org/10.1029/JZ065i003p00799. URL https://agupubs.onlinelibrary.wiley.com/doi/abs/10.1029/JZ065i003p00799.

K. H. Schatten, J. M. Wilcox, and N. F. Ness. A model of interplanetary and coronal magnetic fields. , 6(3):442–455, Mar. 1969. doi: 10.1007/BF00146478.

F. Simpson and K. Bahr. Practical magnetotellurics. 02 2005. doi: 10.1017/CBO9780511614095.

A. W. P. Thomson. Geomagnetic observatories: monitoring the earth's magnetic and space weather environment. *Weather*, 69(9):234–237, 2014. doi: https://doi.org/10.1002/wea.2329. URL https://rmets.onlinelibrary.wiley.com/doi/abs/10.1002/wea.2329.

J. Torta, S. Marsal, and M. Quintana. Assessing the hazard from geomagnetically induced currents to the entire high-voltage power network in spain. *Earth, Planets and Space*, 66, 11 2014. doi: 10.1186/1880-5981-66-87.

J. M. Torta, A. Marcuello, J. Campanyà, S. Marsal, P. Queralt, and J. Ledo. Improving the modeling of geomagnetically induced currents in spain. *Space Weather*, 15(5):691–703, 2017. doi: https://doi.org/10.1002/2017SW001628. URL https://agupubs.onlinelibrary.wiley.com/doi/abs/10.1002/2017SW001628.

A. Viljanen. Geomagnetically induced currents in the finnish natural gas pipeline. *Geophysica*, 25(1/2):135–159, 1989.

A. Viljanen, A. Pulkkinen, R. Pirjola, K. Pajunpää, P. Posio, and A. Koistinen. Recordings of geomagnetically induced currents and a nowcasting service of the finnish natural gas pipeline system. *Space Weather*, 4(10), 2006. doi: https://doi.org/10.1029/2006SW000234. URL https://agupubs.onlinelibrary.wiley.com/doi/abs/10.1029/2006SW000234.

A. Vourlidas, L. A. Balmaceda, G. Stenborg, and A. Dal Lago. Multi-viewpoint Coronal Mass Ejection Catalog Based on STEREO COR2 Observations. , 838(2): 141, Apr. 2017. doi: 10.3847/1538-4357/aa67f0.

A. A. Zawawi, N. F. A. Aziz, M. Z. A. A. Kadir, H. Hashim, and Z. Mohammed. Evaluation of Geomagnetic Induced Current on 275 kV Power Transformer for a Reliable and Sustainable Power System Operation in Malaysia. *Sustainability*, 12(21):1–1, November 2020. URL https://ideas.repec.org/a/gam/jsusta/v12y2020i21p9225-d440792.html.

K. Zheng, D. Boteler, R. J. Pirjola, L.-g. Liu, R. Becker, L. Marti, S. Boutilier, and S. Guillon. Effects of system characteristics on geomagnetically induced currents. *IEEE Transactions on Power Delivery*, 29(2):890–898, 2013. doi: 10.1109/TPWRD.2013.2281191.